AD-775 381

INVESTIGATIONS PERFORMED ON THE ARCTIC
ICE DYNAMICS JOINT EXPERIMENT MARCH 1971

S. F. Ackley, et al

Cold Regions Research and Engineering
Laboratory

Prepared for:

Advanced Research Projects Agency

December 1973

The findings in this report are not to be
construed as an official Department of
the Army position unless so designated
by other authorized documents.

i

AD-775381

DOCUMENT CONTROL DATA - R & D

Security classification of title, body of abstract and indexing annotation must be entered when the overall report is classified)

1. ORIGINATING ACTIVITY (Corporate author)	2a. REPORT SECURITY CLASSIFICATION
U.S. Army Cold Regions Research and Engineering Laboratory Hanover, New Hampshire 03755	Unclassified
	2b. GROUP

3. REPORT TITLE

INVESTIGATIONS PERFORMED ON THE ARCTIC ICE DYNAMICS JOINT EXPERIMENT, MARCH 1971

4. DESCRIPTIVE NOTES (Type of report and inclusive dates)

5. AUTHOR(S) (First name, middle initial, last name)

S.F. Ackley, W.D. Hibler, III, A. Kovacs, W.F. Weeks, A. Hartwell and W.J. Campbell

6. REPORT DATE	7a. TOTAL NO. OF PAGES	7b. NO. OF REFS
December 1973	67	52

8a. CONTRACT OR GRANT NO.	9a. ORIGINATOR'S REPORT NUMBER(S)
ARPA Order 1615	
b. PROJECT NO.	Research Report 315
c.	9b. OTHER REPORT NO(S) (Any other numbers that may be assigned this report)
d.	

10. DISTRIBUTION STATEMENT

Approved for public release; distribution unlimited.

11. SUPPLEMENTARY NOTES	12. SPONSORING MILITARY ACTIVITY
	Advanced Research Projects Agency 1400 Wilson Blvd. Arlington, Va. 22209

13. ABSTRACT

The report is in five parts. Part I, Mesoscale Strain Measurements on the Beaufort Sea Pack Ice: Fracture (lead and crack) orientations in first-year ice indicate correlation with the orientation of the strain rate ellipse. A qualitative relation is suggested between the fracture density and the long-term divergence rate. Correlation was also observed between the divergence of the wind field, as computed from the surface pressure field, and the ice divergence. Part II, Structure of a Multiyear Pressure Ridge: Three transverse profiles were measured across a large pressure ridge in the Beaufort Sea. The ridge sail extended 4 m above sea level and the keel 13 m below. The cross sections of the keel were roughly semicircular, suggesting that form drag coefficients for flow transverse to the long axes of multiyear ridges may be as high as 0.8. Part III, Top and Bottom Roughness of a Multiyear Ice Floe: A spectral study of the snow and ice topography of a multiyear floe showed that the snow cover attenuates the roughness amplitude of the ice surface but does not cover it completely. The snow surface variance is lower than the ice surface variance by a factor of 1/3 to 1/4. The correlation between snow and ice surface roughness is significant for long wavelengths (> 8 m) but not for short wavelengths (< 4 m). The ice sheet as a whole is in free-floating, isostatic equilibrium, but pronounced local deviations from isostatic equilibrium are common. Part IV, Air Photo Analysis of Sea Ice Deformation in the

DD FORM 1473 REPLACES DD FORM 1473, 1 JAN 84, WHICH IS OBSOLETE FOR ARMY USE.

14. KEY WORDS	LINK A		LINK B		LINK C	
	ROLE	WT	ROLE	WT	ROLE	WT
Beaufort Sea Floating ice Ice navigation Ice openings Pack ice Sea ice						

13. Abstract (Cont'd)

Beaufort Sea: The time, direction and magnitude of deformational motion were determined by combining observations of the changes in features related to ice deformation (leads, fractures, pressure ridges) with mesoscale measurements of strains and strain rates on the ice. Part V, Data on Morphological and Physical Characteristics of Sea Ice in the Beaufort Sea: Measurements of the size of ice blocks in newly formed pressure ridges and measurements of salinity and temperature are presented.

i-b

INVESTIGATIONS PERFORMED ON THE ARCTIC ICE DYNAMICS JOINT EXPERIMENT
MARCH 1971

S.F. Ackley, W.D. Hibler III, A. Kovacs,
W.F. Weeks, A. Hartwell, W.J. Campbell

December 1973

PREFACE

This report comprises five separate papers covering research performed as part of the Arctic Ice Dynamics Joint Experiment (AIDJEX). The authors include Stephen F. Ackley, Research Physicist, Dr. William D. Hibler, Research Physicist, and Dr. Wilford F. Weeks, Research Glaciologist, of the Snow and Ice Branch, Research Division, U.S. Army Cold Regions Research and Engineering Laboratory (USA CRREL); Austin Kovacs, Research Civil Engineer, of the Foundations and Materials Research Branch, Experimental Engineering Division, USA CRREL; Allan D. Hartwell, Geologist, formerly of the Snow and Ice Branch; and Dr. William J. Campbell, Geophysicist, of the U.S. Geological Survey.

Manuscript received 6 September 1973

CONTENTS

INVESTIGATIONS PERFORMED ON THE ARCTIC ICE
DYNAMICS JOINT EXPERIMENT, MARCH 1971

by

S.F. Ackley, W.D. Hibler, III, A. Kovacs,
W.F. Weeks, A. Hartwell and W.J. Campbell

INTRODUCTION

The Arctic Ice Dynamics Joint Experiment was formulated in the latter part of the 1960's (Untersteiner and Hunkins 1969)* when, based on previous measurements and models, it became apparent that a coordinated, multidisciplinary, international investigation would be useful for determining the necessary parameters for a predictive model of the motion and deformation of pack ice. This predictive capability could then be applied to such problems as navigation, climate prediction, construction, and over-ice transportation in the Arctic Basin. A revised scientific plan has been formulated to implement such a program (Maykut et al. 1972).† The basis of the plan is to occupy a set of stations (four in the current plan) on the arctic pack for a one-year period and perform a variety of meteorological, oceanographic, and ice dynamics experiments. These experiments would specify the driving forces and ice response to the driving forces, thus allowing formulation of predictive physical and numerical models. This main experiment, currently scheduled for 1975, was preceded in 1971 and 1972 by a set of pilot studies in which camps were occupied for shorter periods of time. Efforts were made to develop techniques, test equipment and provide data for the formulation of the models and to plan for the main experiment. Post-operations reports of these studies appear in AIDJEX Bulletins No. 7** and No. 14.†† The pilot studies have proved to be valuable experiments in their own right, yielding new data and new interpretations in many different areas of arctic sea ice investigations, arctic meteorology and Arctic Ocean oceanography.

This report, divided into five parts, describes the work performed by the USA CRREL group working on AIDJEX using data obtained during the 1971 pilot study. Parts 1, 2 and 3 have been published in the literature; Parts 4 and 5 have not previously been reported. The purpose of this report is to present in final form a single compilation of the ice deformation and morphology data obtained during this program in 1971.

---

*Untersteiner, N. and K.L. Hunkins (1969) Arctic Ice Deformation Joint Experiment, Final Report. University of Washington, ONR Contract N 00014-67-A-0103-0004, 39 p.

†Maykut, G.A., A.S. Thorndike and N. Untersteiner (1972) AIDJEX scientific plan. University of Washington, Division of Marine Resources, AIDJEX Bulletin No. 15, 67 p.

**AIDJEX Bulletin 7 (1971) 1971 Pilot study post operations narratives. University of Washington, Division of Marine Resources.

††AIDJEX Bulletin 14 (1972) 1972 Pilot study post operations narratives. University of Washington, Division of Marine Resources.

PART I: MESOSCALE STRAIN MEASUREMENTS
ON THE BEAUFORT SEA PACK ICE

by

W.D. Hibler, III, W.F. Weeks, S. Ackley,
A. Kovacs and W.J. Campbell

ABSTRACT

The deformation of a strain triangle approximately $6 \times 8 \times 11$ km located on first-year ice in the Beaufort Sea was observed over a two-week period in March 1971. Significant strain events ($\sim 1.5\%$) were observed during short (6-hour) time periods. The long-term (one day or more) divergence rate varied between 0.04 and 0.08×10^{-3} hr^{-1}. Short-term divergence rates showed values as high as 0.29×10^{-3} hr^{-1}. The observed shearing motion indicated that the floes to the east were moving south relative to the floes to the west. This agrees with the shear pattern that might be expected, considering the location of the station in the Pacific Gyre. Studies of fracture (lead and crack) orientations in the vicinity of the strain triangle indicate reasonable correlations with the orientation of the strain rate ellipse. A qualitative relation is suggested between the fracture density and the long-term divergence rate. Correlations were also observed between the divergence of the wind field as computed from the surface pressure field and the ice divergence.

INTRODUCTION

One of the prime goals of the Arctic Ice Dynamics Joint Experiment (AIDJEX) is an improved understanding of the drift of the pack ice in the Arctic Ocean. In the past this problem has interested a number of investigators who have attempted to analyze the drift tracks of manned ice stations and beset ships (Campbell 1968). The first of these investigations (Nansen 1902) considered a wind stress r_a, a water stress r_w and a Coriolis force C as the pertinent terms in the momentum equation. More recent work included the gradient current force G and the existence of appropriate boundary layers. All of these forces can be considered to exist at every point on the ice. For small areas of interest, such as the floe on which a given station is located, these forces can, in principle, be measured and expressed in terms of pertinent averages. Even as this work was progressing, field observations clearly indicated a significant lateral transfer of stress through the pack. For example, severe ridging frequently occurred when the local winds were calm. This lateral transfer of stress has been called the internal ice stress I and is the least understood of the forces currently included in the momentum equation (I is more precisely the divergence of the internal stress field, $I = \nabla \cdot r$). The local value of I is a function of both the regional stress field and the distribution of ice types, as well as roughness elements such as ridges, hummocks and leads; in short, it is determined by the thermodynamic and strain history of the ice. As new strains occur, the resulting deformation features modify the average roughness of both upper and lower ice surfaces. This changes the values of r_a and r_w exerted on the surrounding pack, which in turn affects I.

The internal ice stress was first treated as a simple frictional resistance by Sverdrup (1928) and later as an effective viscosity by Ruzin (1959), Reed and Campbell (1962) and Campbell (1965). The later approach assumes that on a large scale the ice pack can be considered to act as a thin layer of a Newtonian viscous fluid. Using the viscous model for I, Campbell (1965) has been able to predict realistic mean drift velocities as well as the actual position of the Pacific Gyre. His results also show how sensitive the mass transport and ice flow fields are to changes in I. Unfortunately his model gives unrealistically high convergence rates for the gyre.

It is possible to conceive of a number of alternative ways to treat the internal ice stress problem (see, for example, the papers in AIDJEX Bulletin No. 2, 1970). However, without an experimental basis for evaluating the results, it would be difficult to choose among the different approaches. Hence, one of the most urgent needs is for sets of good field observations on the actual deformation of the arctic ice pack, both under a wide range of ice conditions and on several time and space scales. Because, in principle, it is always possible to measure G, C, τ_a and τ_w at the deformation sites, it should at times be possible to determine I as a residual. The variations in I can then be related to both the regional stress and strain fields and to differences in the large-scale morphological characteristics of the pack in the study areas.

This paper describes the results of a pilot study of the local deformation of the pack in the vicinity of Camp 200, the site of the 1971 AIDJEX pilot project in the Beaufort Sea. The purpose of this study was to test experimental procedures and to obtain information on both the total strain and the variation in the strain rate that occurred during the occupancy of the stations.

PREVIOUS WORK

To the best of our knowledge, there have been only a few attempts to measure the deformation of the pack ice even though the desirability of making such measurements has been obvious for some time. The reason for this paucity of data is clear: most field parties operating in the Arctic Ocean have been based on only one drifting station and have not had the air support necessary to lay out and monitor strain arrays in areas of active ice deformation.

Two studies of local strains have been made using a theodolite and a base line laid out on an ice island. In 1952 Crary followed the relative motion of several prominent hummocks located in the pack within 5 km of the edge of Fletcher's Ice Island T-3 (Browne and Crary 1958). The relative locations of these hummocks did not change significantly over a five-month period. In addition, between 1962 and 1965 a series of similar measurements was made from ARLIS II by Senior, Wittmann and Skiles (1968). In the spring of 1962, the relative motion of four towers located within 1130 m of the edge of the ice island was monitored every two to three days for a one-month period. During this time period a lead 9 m wide opened within the array and then closed, forming a 3-m pressure ridge. In the spring of 1963, a larger (nine-tower) array was established and monitored at similar time intervals for 1½ months. The maximum distance of a tower from one end of the base line was just under 5 km. For the first three weeks, little motion occurred. Then a lead 300 m wide rapidly opened between the base line and the towers. Later, a number of leads 15 m wide developed in the area of the towers. Divergences as large as 0.039 were observed, although most values lay between ±0.01. Similar studies were performed in the spring of 1963 and in the fall of 1963, 1964 and 1965, but no significant relative motion was observed.

The T-3 and ARLIS-II studies share a common difficulty. Ice islands are not typical elements of the arctic pack. In general, differences in movement between ice islands and the surrounding pack are to be expected. The reason for this is the difference in the roughness of the upper and

lower surfaces of the ice island as compared to the ridged sea ice, and the larger Coriolis effect on the ice island because of its larger mass. Sometimes, however, the sea ice near an ice island appears to move as a unit with the island. For example, Senior, Wittmann and Skiles estimate, based on observations from an aircraft, that during much of the period of their strain measurements, the ice within 8 km of ARLIS-II was moving as a unit. In short, unless independent verification is available, strains measured in the vicinity of an ice island are not necessarily representative of strains in the surrounding sea ice.

Dunbar and Wittmann (1963) have also measured variations in the areas of the triangle formed by NP-10, NP-11 and ARLIS-II and the quadrilateral formed by these three stations plus T-3. Changes of up to 20% were noted over a 15-day period (the measurement interval), and a maximum change of 63% relative to the initial area was noted over the total period of measurement (four months). The areas involved (roughly 140,000 km^2 and 280,000 km^2, respectively) were large enough that differences in motion between the ice islands T-3 and ARLIS-II and the surrounding pack would not be significant. Other numerical measures of the deformation were not calculated.

The only study of the relative motion of a station array located completely on pack ice was performed near the North Pole (approximately 88°N, 147°E) during the spring of 1961 (Bushuyev et al. 1970). Four stations were placed in a square with sides of 75 to 100 km. In general, the stations moved as a block, even down to two small counterclockwise loops which occurred at roughly the same time (within 6 to 8 hours) in each of the otherwise fairly straight tracks. A study of the station velocities clearly indicated that the ice drift commonly preceded the arrival of the actual wind and that the lead time increased with the wind strength. Bushuyev et al. (1970) felt that the influence of the wind was transmitted through the ice for at least 150 to 200 km. This again emphasizes the importance of the internal ice stress term in the momentum equation. Although a simple linear relation was shown between the angular rotation of the array of stations and the vorticity of the wind field, no parameters relating to the deformation of the ice were computed.

This survey of previous work reveals that in a mesoscale study of ice deformation one might expect strains of anywhere between zero and several per cent. Because studies have not been made of the homogeneity of pack deformation as a function of the array size, there is little basis for deciding the optimum size of the strain array. Also, little is known about how frequently the deformation array should be surveyed. In the past the most frequent observations were made daily.

SITE LOCATION

The site of the 1971 AIDJEX base camp (Camp 200) was on the edge of a large multiyear floe roughly 16 km across, located at 73°45'N, 130°15'W (Fig. 1). The drift of the camp was generally in a south or southeasterly direction with the rate varying from 2 to 15 km per day.

After an initial aerial examination of the pack in the vicinity of the base camp, it was decided to establish the strain array in the approximately 2-m-thick first-year ice to the northeast. The general layout of the strain array relative to Camp 200 and to the major fractures and leads in the vicinity is shown in Figure 2. MRA-3 tellurometers were used as distance-measuring instruments. Distance measurements along the line α-β were obtained beginning on 11 March with complete triangle closures not being made until 12 March. Several closures were made thereafter with the final closure being made on 23 March.

Figure 1. Location of the 1971 AIDJEX camp (position 0). Also shown are the locations of the four other positions where the surface barometric pressure was obtained so that the wind stress could be calculated. Positions 1, 3 and 4 are located near permanent weather stations. Pressures at positions 1-4 were taken from Canadian meteorological maps. The distance a (eq 13) was about 320 km.

RESULTS

Computational technique

The following procedure was used to determine the strain rate tensor from the closure data. Consider a medium with the velocity at each point of the medium given by $v(x)$. Since we are concerned only with the horizontal motion of the ice pack, the velocity vector is two-dimensional. Using tensor notation the strain rate tensor $\dot{\epsilon}_{ij}$ is defined by

$$\dot{\epsilon}_{ij} = \frac{1}{2}\left(\frac{\partial v_i}{\partial x_j} + \frac{\partial v_j}{\partial x_i}\right). \tag{1}$$

To measure the strain rate tensor we need only to measure relative positions between sets of points, say P and P', as a function of time. In particular, if we choose a coordinate system such that the line PP' is oriented at an angle θ to the x-axis, then the one-dimensional strain rate along PP', denoted by $\dot{\epsilon}(PP')$, is related to the strain rate tensor by the equation (Nye 1957)

$$\dot{\epsilon}(PP') = \dot{\epsilon}_{11}\cos^2\theta + \dot{\epsilon}_{22}\sin^2\theta + 2\dot{\epsilon}_{12}\sin\theta\cos\theta. \tag{2}$$
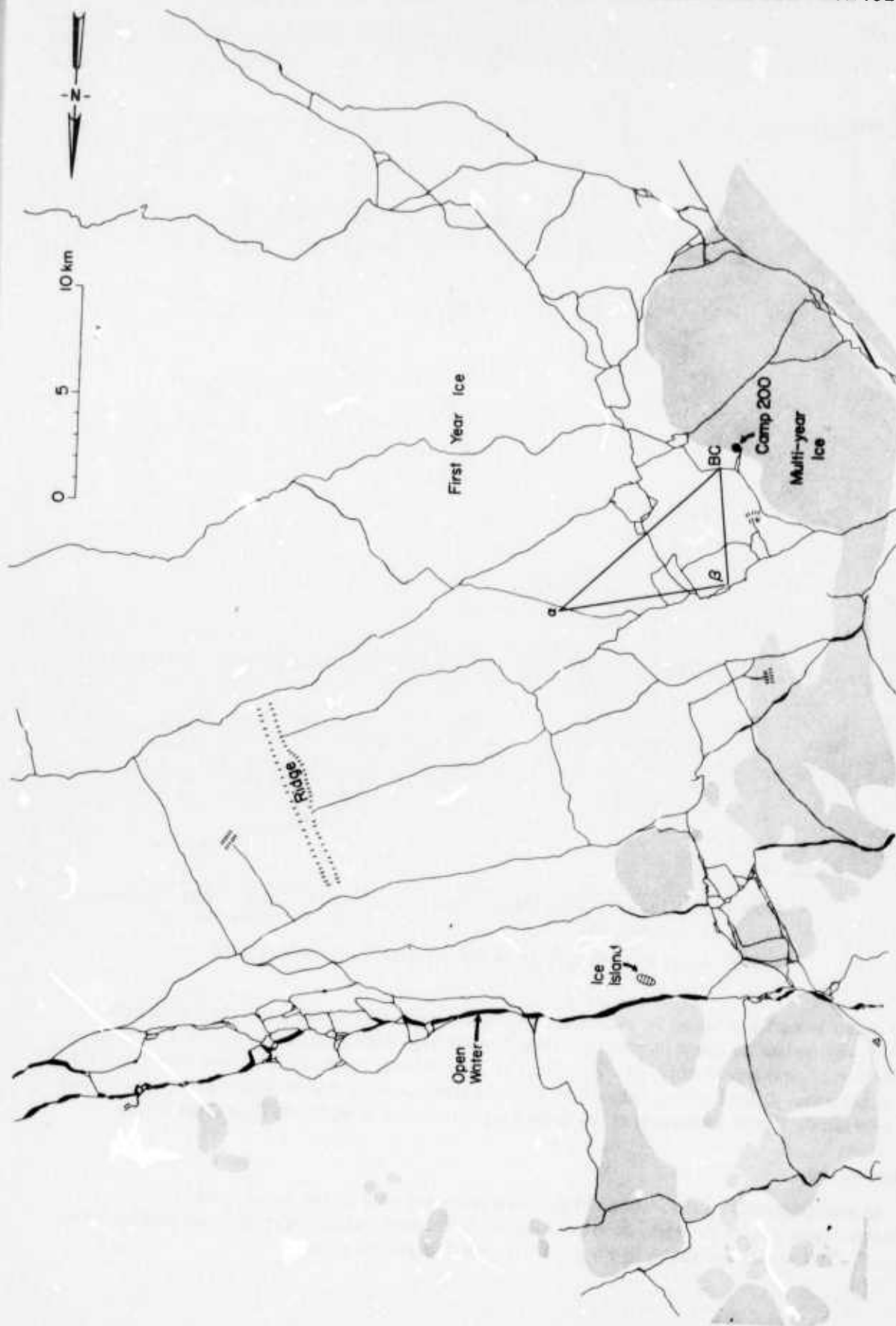
Figure 2. Overlay of a photo mosaic showing the location of the strain array relative to the major fractures in the area near Camp 200 on 15 March 1971. The photography was obtained by NASA at an altitude of 10,600 m. Multiyear ice, annual ice, and ice islands were identified by variations in surface roughness.
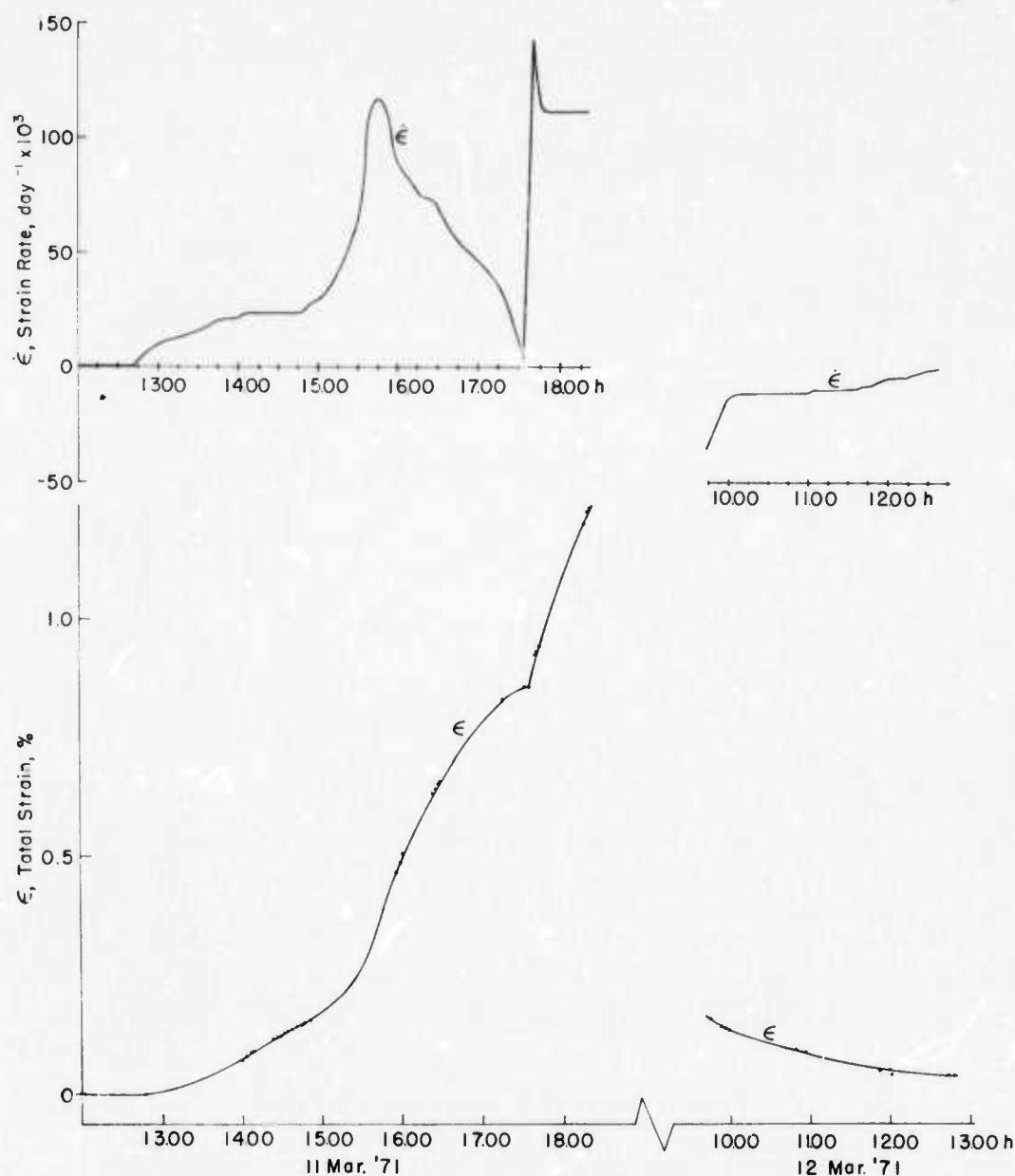
Figure 3.   Strain and strain rates on the α-β line, 11-12 March 1971.

This result is easily obtained by transforming $\dot{\epsilon}_{ij}$ into a coordinate system with the x-axis parallel to PP'. By measuring linear strain rates along three or more non-colinear lines, a set of equations of the form of eq 2 may be solved for $\dot{\epsilon}_{ij}$. Since in our case only three linear strains were used, the set of equations yielded unique values for the strain rate tensor so that least squares averaging was not necessary. (For a discussion of the least squares solution of eq 2, see Thorndike 1970.)

Linear strains

As was discussed earlier, technical problems prevented closing the strain triangle until 12 March. However, on the 11th, an interesting set of detailed readings was obtained between sites α and β. The results are shown in Figure 3. The total strain ε is given by
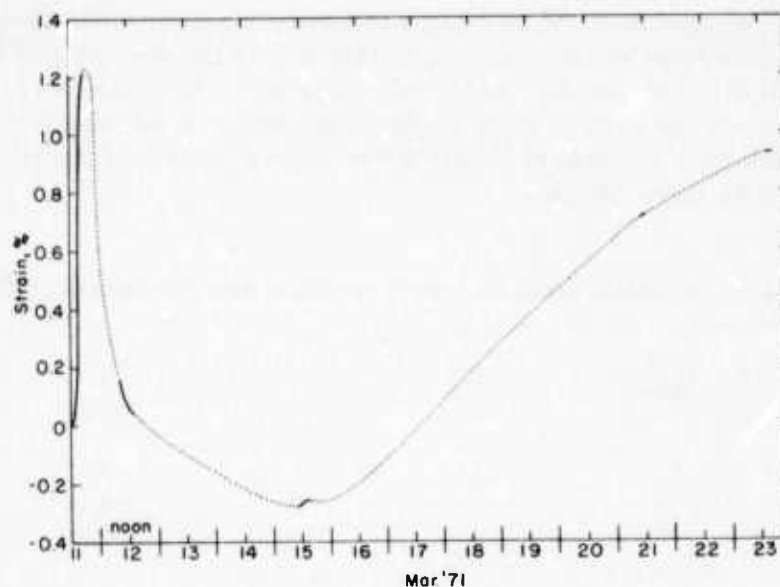
*Figure 4. Strain on the α-β line, 11-23 March 1971. The solid
portions of the curve indicate times when the length of the line
was measured.*

$$\epsilon = \frac{\Delta l}{l_0} \tag{3}$$

where l_0 is the initial length of the strain line (in this case 8317 m). Figure 3 shows that after an
hour of no variation in ϵ, a rapid extension started with expansions of as much as 0.7 m min^{-1}.
· After 4.5 hours, the extension essentially ceased (at 1730 hours) and tnen quickly started again.
If we examine the simultaneous plot of the strain rate $\dot{\epsilon}$, we see that it reached a maximum of 0.116
day^{-1} at 1545 hours, then decreased to roughly zero at 1730 hours, then rapidly increased to 0.142
day^{-1} before finally decreasing to a roughly constant value of 0.111 day^{-1}. These events suggest
that we saw the transfer of momentum through the pack by jostling between floes. At the time we
returned to the base camp, the rapid extension was still continuing. When we reoccupied the α-β
line at 0945 hours the following day, the value of ϵ was gradually approaching zero, indicating a
near return to the state of strain that existed prior to the extension. The maximum period of time
over which this extension occurred was roughly 22 hours.

Figure 4 shows the strain along the α-β line for the complete period of our measurements.
Figures 3 and 4 tell us a great deal about the necessary rate of data acquisition for mesoscale strain
measurements. Daily readings are clearly not adequate: if we had measured the α-β line at noon on
11 and 12 March, we would have concluded that no strains had occurred during this time period. To
clearly define an event such as this extension, readings should be taken at least every 15 minutes.
If one wished to examine the fine structure of the event, such as the cusp in the ϵ curve at 1730
hours on 11 March, readings would be required at least every 5 minutes.

Strain tensor and strain rate tensor

The complete strain triangle was measured over a 10-day period beginning with an initial
closure at 1100 hours on 12 March. Subsequent closures were made on 15, 21 and 23 March. On all
days except 23 March, several sets of closures were made over a period of several hours, allowing

strain rates to be estimated over time intervals of both hours and days. Strain rates computed over time intervals of a few hours will be referred to as *short-term* strain rates, whereas rates computed with time intervals of one or more days will be called *long-term*. The strain closure data are presented as a function of time in terms of the strains along each leg of the triangle in Table I. Where different strain lines were measured at slightly different times, linear extrapolation was used to estimate strains at the times indicated.

Table I. Net strains along the legs of the strain triangle (units of 10^{-3}).
Initial readings (12/1100): $a-\beta$, 8324.5 m; BC$-\beta$, 5579.2 m; BC$-a$, 10,729.0 m.

Date/Time (March 1971)	$a-\beta$	BC$-\beta$	BC$-a$
12/1100	0	0	0
12/1500	-0.463	-0.870	-1.11
15/1000	-3.69	-0.46	-3.30
15/1300	-3.64	-1.02	-3.34
15/1600	-3.50	-1.26	-3.24
21/1200	7.75	-2.21	1.45
21/1500	7.82	-2.24	1.51
23/1500	8.45	-2.22	-8.46

While the strain measurements were being taken, the direction of true north was determined only approximately (within 5 degrees). Consequently, it was not possible to calculate accurate vorticities. Within this error there was no indication of a rotation of the strain array. Therefore, in both long- and short-term strain rates, it was assumed that the angles between the $a-\beta$ line and true north remained fixed. Even if this is not exactly true, the invariants of the strain rate tensor will still be correct as they are independent of the coordinate system.

In the strain calculations the vertex angles of the strain triangle were recalculated using the triangle leg lengths at the beginning of each time interval. The net strain tensor was then obtained by summing the differential values of the strain tensor in the north coordinate system.

In one form, the two invariants of a two-dimensional strain rate tensor are the two components of the tensor along the principal axes (Glen 1970). The results are presented in this form in Figure 5. The data are presented in the convention often used in glacier flow, namely as two perpendicular lines oriented parallel to the directions of the principal axes. The lengths of the lines are proportional to the magnitudes of the principal axis components. In Figure 5, an outward arrow indicates extension and a bar denotes compression. From the information in this figure, the shear components of the strain rate tensor in any coordinate system may be constructed. The general trend of the data, with the exception of the strain rate observed between 12 and 15 March, is an extension in approximately the east-west direction.

Another presentation of the two invariants of the strain rate tensor is the divergence rate $\dot{\epsilon}_{ii}$ and $\dot{\epsilon}_{ij}\dot{\epsilon}_{ij}$ (in the principal axis system these two invariants are $\dot{\epsilon}_x + \dot{\epsilon}_y$ and $\dot{\epsilon}_x^2 + \dot{\epsilon}_y^2$, respectively). Previous authors (Senior, Wittmann and Skiles 1968) have reported only the divergence rate, a useful, if not complete, description of the strain. For a direct comparison with previous work as well as for later analysis, the divergence, divergence rate, and shear (y-axis in the north direction) are presented in Figure 6. As can be seen, the long-term divergence rate varies from 0.042×10^{-3} hr^{-1} to 0.08×10^{-3} hr^{-1}. The short-term divergence rate, on the other hand, has values as large as
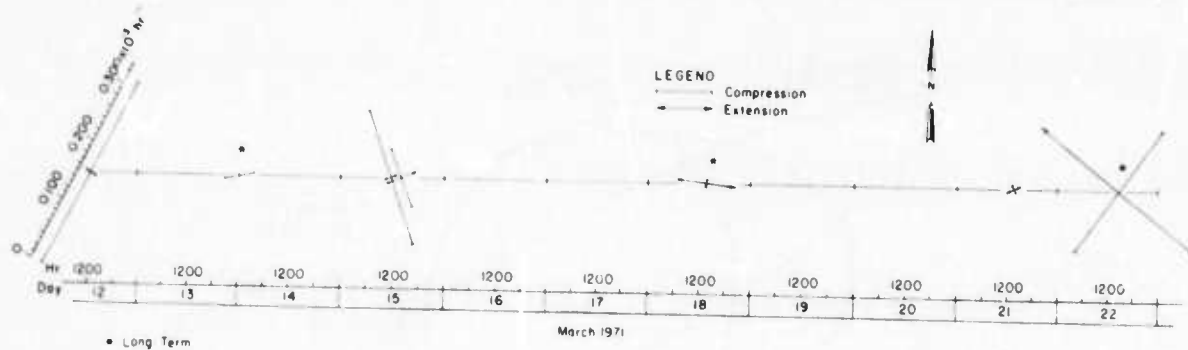
Figure 5. Principal axis components of the strain rate tensor as a function of time. The long-term rates were calculated using time intervals of two or more days, whereas the other rates were calculated using time intervals of from one to two hours. The directions of the bars indicate the principal axis directions with their lengths being proportional to the strain rates.
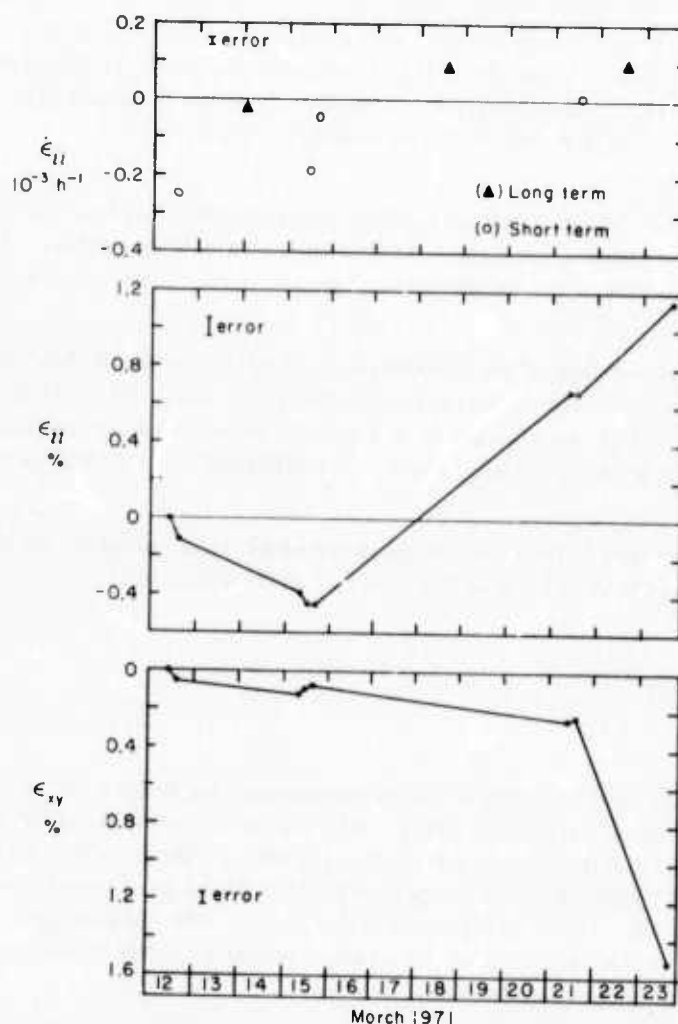

Figure 6. The divergence rate $\dot{\epsilon}_{11}$, net divergence ϵ_{11} and net shear ϵ_{xy} as a function of time. The short-term divergence rates were calculated using time intervals of from one to two hours whereas the long-term rates were calculated using time intervals of two or more days.
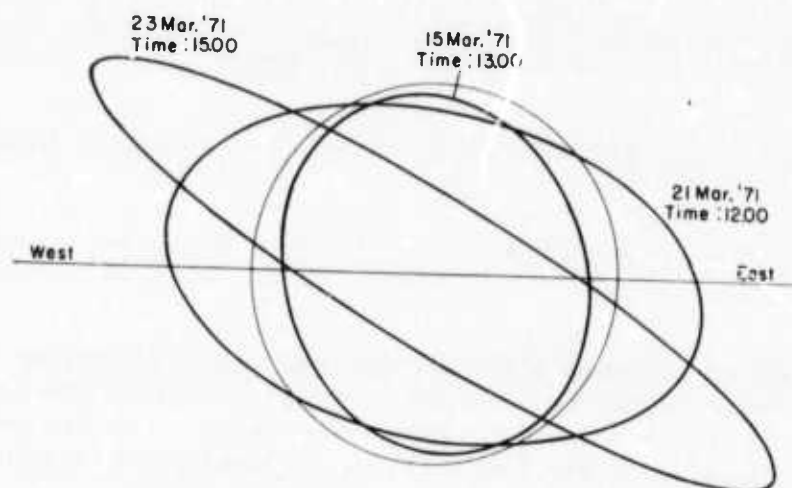
Figure 7. Net strain ellipses as a function of time. The major ellipse axis is in the direction of maximum extension (or minimum compression) and the minor ellipse axis is in the direction of minimum extension (or maximum compression)

0.293×10^{-3} hr^{-1} This indicates that on the time scale of hours large strains occur which are averaged out when measurements are made over time intervals of several days. The presence of this type of fluctuation is borne out by the detailed measurements along the single strain line a-β as shown in Figure 4.

For a physical interpretation of the divergence, it is useful to recall that when the divergence rate is constant over a region, the divergence rate equals the change in area per unit time divided by the area. From the plot of the divergence in Figure 6, we see that the change in area from 12 to 15 March was about 0.4% with the ice converging, while from 15 to 22 March it was about 1% with the ice diverging.

A useful aid in visualizing the deformation in the strain area during the measurement period is the strain ellipse, which is defined in the principal axis system by

$$\frac{x^2}{(1 + \epsilon_x)^2} + \frac{y^2}{(1 + \epsilon_y)^2} = 1. \tag{4}$$

This ellipse has a minor axis in the direction of compression (or least extension) and a major axis in the direction of extension (or least compression). To show the net strain by using this procedure, we have constructed net strain ellipses for 15 March (1300), 21 March (1200) and 23 March (1500). These times are 74, 217 and 268 hours, respectively, relative to an assumed circle at time zero on 12 March, 1100 hours. The results are presented in Figure 7 with the principal axis components enhanced by 100. It is clear that most of the strain is occurring along a line approximately in the east-southeast to west-northwest direction.

Estimation of errors

The accuracy of the MRA-3 tellurometers when operated at only one cavity tune is better than 0.1 m for differential measurements of distance and better than 1 m for absolute measurements. In

view of this type of accuracy an upper error limit would be 1.5 m over long time intervals (one or more days) and 0.1 m over short time intervals (a few hours). Using these values, the average long-term linear strain measurement error, σ, is 0.02%, and the short-term error is 0.0013%.

To estimate the variation in the strain tensor components due to such measurement errors, we will assume that the errors are normally distributed with the same variance along each strain line. With these assumptions, the maximum likelihood (Mathews and Walker 1965) values (in the least squares sense) for the strain rate tensor are obtained by solving the set of equations of the form of eq 2. The errors in the strain rate tensor components within this approximation are given by

$$\Delta x_m = \sigma \sqrt{[(\tilde{L}L)^{-1}]_{mm}} \tag{5}$$

where Δx_m denotes the strain rate tensor errors with

$$\Delta x_1 = \Delta \dot{\epsilon}_{xx}, \quad \Delta x_2 = \Delta \dot{\epsilon}_{yy}, \quad \Delta x_3 = \Delta \dot{\epsilon}_{xy}$$

and

$$L_{i1} = \cos^2 \theta_i, \quad L_{i2} = \sin^2 \theta_i, \quad L_{i3} = 2 \sin \theta_i \cos \theta_i .$$

Here θ_i is the angle between the ith strain line and the east-west axis and $\tilde{L}$ is the transpose of L. For our particular array, using the angles obtained from the first closure, eq 5 yields

$$\Delta \dot{\epsilon}_{xx} = 1.40 \, \sigma, \quad \Delta \dot{\epsilon}_{yy} = 0.95 \, \sigma, \quad \Delta \dot{\epsilon}_{xy} = 1.46 \, \sigma .$$

Using the values of σ mentioned above and eq 5, we arrive at long-term net strain errors for the divergence and shear respectively of 0.047% and 0.029%. For the strain rate errors, the short-term divergence and shear errors over a three-hour interval are 0.01×10^{-3} hr^{-1} and 0.006×10^{-3} hr^{-1} respectively. The long-term divergence and shear errors over a 72-hour interval are respectively 0.0008×10^{-3} hr^{-1} and 0.005×10^{-3} hr^{-1}. These errors are presented as error bars in Figure 6 and, as can be seen, are quite small compared to the magnitude of the strain events. These errors do not, of course, represent the magnitude of the variations in the strain due to lateral inhomogeneity in the strain field (i.e. different strains for different triangles). We expect that such variations would be much larger than the measurement errors. A detailed study of mesoscale strain inhomogeneity is presently underway using data collected in 1972.

CORRELATION OF SYNOPTIC AERIAL PHOTOGRAPHY WITH MEASURED STRAINS

Aerial photography of the strain triangle and surrounding area was obtained from NASA overflights on 11 and 15 March and by NAVOCEANO overflights on 21 and 23 March. These dates coincided with strain measurements. Unfortunately there was considerable variability in the photography because of changes in the weather conditions, the altitudes flown, and the paths flown. Overlays of mosaics of the area from 15 and 23 March are shown in Figures 2 and 8. Scale and area coverage differences arise from the altitudes at which the two flights were made -- 10,600 m on 15 March and 1500 m on 23 March.

From the photography on which Figure 2 is based, net differences in ice type could be distinguished and are indicated on the overlay. These distinctions were based on the surficial appearance of the different ice types. First-year ice is characterized by sharp angular ridges, with relatively flat ice between them. Multiyear ice shows a freckled appearance caused by its undulating
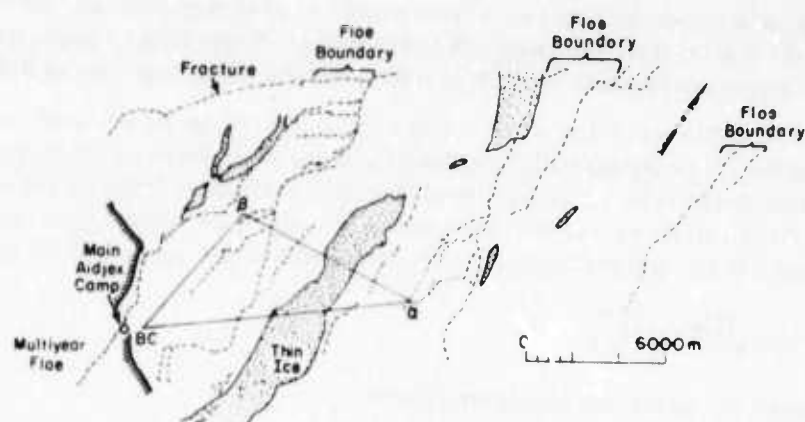
Figure 8. Overlay of an infrared mosaic of the region near Camp 200
on 23 March taken at an altitude of 1500 m by NAVOCEANO. The
fractures, multiyear ice and thin annual ice were identified by light
and dark tones on the infrared mosaic.

"melt" topography. Ice islands are distinguished by their rolling, washboard-like topography and
high freeboard. Fractures show as dark lines because of the open water or very thin ice present
within them.

Because Figure 8 was made from imagery obtained at a lower level, more detail is present,
although the area covered is not so extensive. This specific overlay was prepared from an infrared
mosaic in which different thicknesses of ice are shown quite clearly because of differences in their
surface temperatures. The thickest ice in the mosaic was the multiyear ice (2.5 to 5.0 m). This
ice appears dark on the mosaic and is shown in the lower left of the overlay. Lighter tones indi-
cate the thinner first-year ice (up to 2 m thick) that made up most of the ice in the area of the strain
triangle Within this matrix of first-year ice, two types of thinner ice existed. The thicker of these
two made up the 2000-m-wide refrozen lead that crosses the BC-α and α-β lines and is shown by
stippled shading in Figure 8. Its exact thickness was not measured, but it is estimated to be ≥ 1 m.
The thinnest ice (0 to 40 cm) occurred in the fracture systems that were active during the strain
measurements on 21 and 23 March. This ice appears as bright, sharp lines on the infrared mosaic
(highest surface temperature) and is shown by the dashed lines in Figure 8.

From Figures 2 and 8 it is apparent that the active leads are not strongly affected by ice
thickness variations, since on both overlays leads cut through first- and multiyear ice without
deflection. One can also see in Figure 8 that the active lead system does not coincide with pre-
existing thin ice areas, possibly because the orientations are slightly different. The thin ice area
showed considerable activity on 11 March and was presumably still a relatively weak zone on 21
and 23 March.

Details of the fracture structure were analyzed by determining the total fracture length in any
given direction. Each fracture was broken into straight line segments from 100 to 300 m in length,
and their orientation and length were measured. The total length in each orientation (10° intervals)
for each day of imagery was then tabulated and converted to a percentage of the total length of
fracture. The results are shown in Figure 9. In addition, the total length was divided by the area
covered by the imagery to give a fracture density analogous to the ridge density used by Mock,
Hartwell and Hibler (1972) and the drainage density often used in hydrology.

Because strain data and imagery are variable in time, detail and coverage, the comparisons be-
tween them must be made with some care. We can hypothesize, however, that the net orientation of
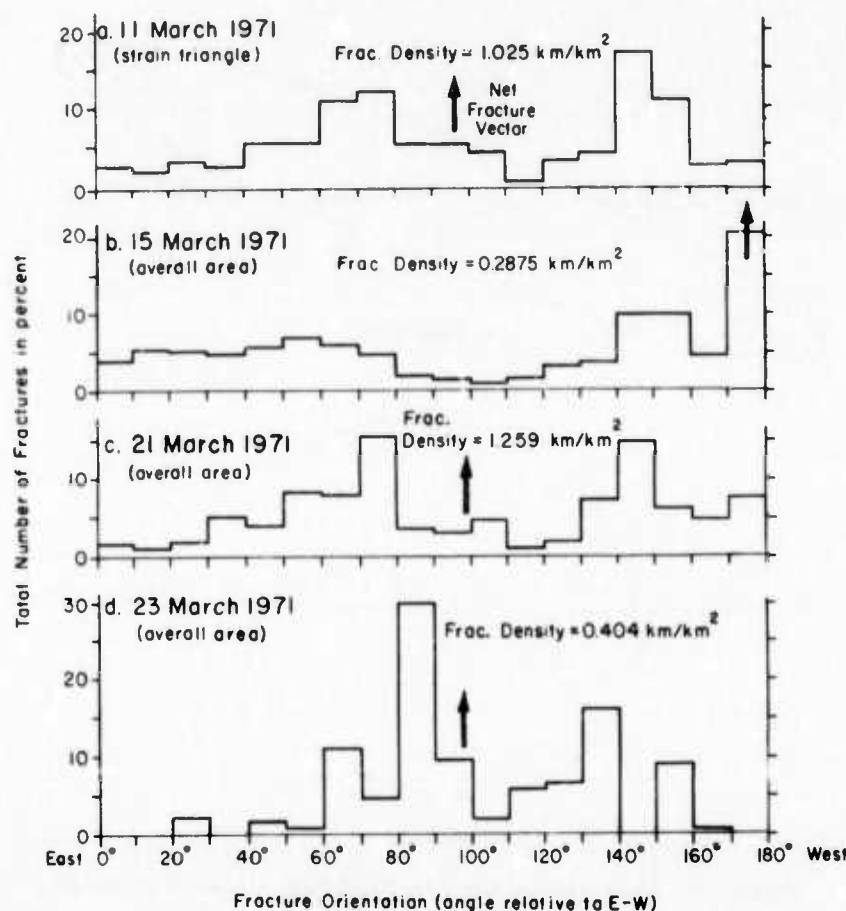
Figure 9. Histogram identifying the fracture orientations obtained from aerial imagery measured in a clockwise direction from the east-west line. Changes in fracture density agree with convergence or divergence of the pack, indicated by the long-term strain rates. Net fracture vectors on the 15th and 21st agree with the direction expected from the short-term strain rates (Fig. 10).

the fractures (if any) should be correlated with the state of stress of the ice pack as manifested by the short-term strain rate. To make this comparison, a net fracture vector was calculated from the results in Figure 9 by using Krumbein's method as described in Mock, Hartwell and Hibler (1972). This method uses twice the angle of each fracture orientation to convert the 180° distribution to a nonsymmetric 360° distribution.

We calculated

$$\bar{\theta} = \frac{1}{2} \arctan \left[\frac{\Sigma f \sin 2\theta}{\Sigma f \cos 2\theta} \right] \tag{6}$$

and

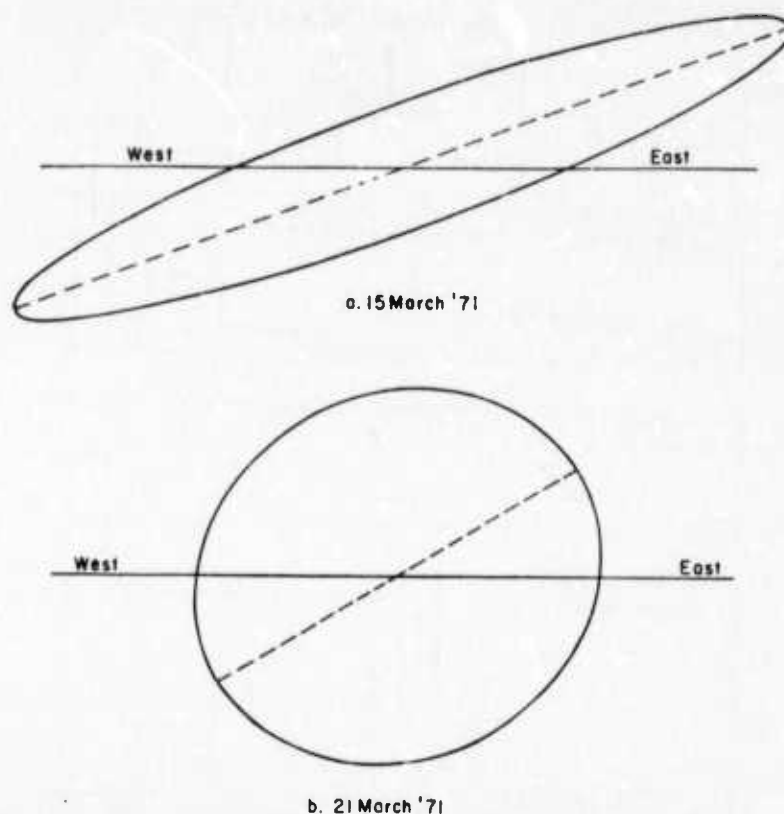$$r = [(\Sigma f \sin 2\theta)^2 + (\Sigma f \cos 2\theta)^2]^{1/2} . \tag{7}$$

Figure 10. Strain rate ellipses for short-term strain rates on 15
and 21 March 1971.

Here $\bar{\theta}$ is the estimate of the resultant vector direction, r is the resultant magnitude of this vector in percent, and f is the percentage of the total lead length in each orientation category. For a directionally random population, r is zero. Referring to Curray (1956), who provides a chart for evaluating significant deviations from zero for r, given the total number of samples, we find that in all cases illustrated in Figure 9 we may reject the hypothesis that our sample is directionally random at the 0.01% level. The directions of the resultant vectors are shown by solid arrows in Figure 9.

On two days, 15 and 21 March, both short-term strain data and aerial imagery were available. For purposes of correlation it is useful to represent the strain on these days by the strain rate ellipse, which is completely analogous to the strain ellipse presented in eq 4 except that strain rates instead of strains are used. As in the strain ellipse, the strain rate ellipse has a minor axis in the direction of compression (or least extension) and a major axis in the direction of extension (or least compression). The strain rate ellipses for 15 and 21 March are illustrated in Figure 10. An angular relationship between the major axis of the strain rate ellipse and the net lead direction may be hypothesized as follows. Once leads are formed, we assume that the deformation of the pack consists of two motions: shear along the leads and extension (or compression) perpendicular to the leads. Consequently, for a diverging strain the major axis of the ellipse would vary from $90°$ to $45°$ relative to the lead orientation, with $90°$ for pure extension and $45°$ for pure shear. Conversely, for a converging strain the major axis would vary from $0°$ to $45°$ relative to the lead direction, with $0°$ for a pure compression and $45°$ for pure shear. Using this model, we note that on 21 March (diverging rate) the fracture orientation was at $9°$ (from true north) and the major ellipse
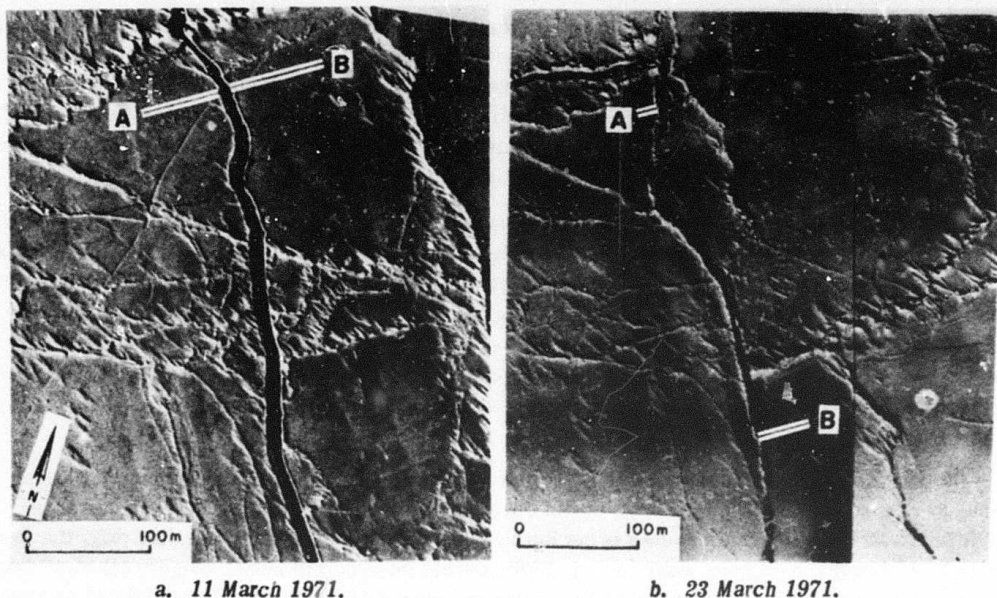
a. 11 March 1971.   b. 23 March 1971.

Figure 11. *Sequential aerial photography showing shear deformation along the lead that crosses the α–β line approximately 1.5 km from β and runs NNW-SSE (see Fig. 8).*

axis was at 68°, with the difference being between 45° and 90° as expected. Conversely, on 15 March, when we observed a converging strain, the lead orientation was at 70° and the major ellipse axis was at 95°, with the difference lying between 0° and 45° as expected.

Although these agreements are qualitative, they do point to a possible way to estimate the direction (within 45°) of the major strain axis from observations of the fracture structure obtained by aerial imagery. This, of course, assumes that it is possible to determine from the imagery whether the ice pack is converging or diverging.

Another correlation might be expected between the long-term divergence rate and the lead density. In particular, if between two days the lead density increased, we would expect that a diverging strain had occurred. A decrease in lead density would indicate the converse. To test this hypothesis, we have calculated the changes in lead density and compared them with the long-term divergence rate. The results are summarized in Table II. As can be seen, there is general agreement, except for the period 21-23 March. We note, however, that the deformation during this period was dominated by a large shear along a single north-south fracture. This fracture can be seen in Figure 11 (see also Hartwell 1972, for a detailed catalogue of motions along leads,

Table II. Observed changes in lead density and the long-term divergence rate of the ice pack during the same time period.

Time period	Change in lead density (km^{-1})	Divergence rate (long-term)
11 to 15 March	1.025 to 0.287 (neg)	Negative
15 to 21 March	0.287 to 1.259 (pos)	Positive
21 to 23 March	1.259 to 0.404 (neg)	Positive

including this particular shear). This may be a case in which the strain triangle was not averaging deformation over a large enough area to yield correct results. It is quite easy to construct an example of a triangle with only shear occurring along a single fracture which cuts through the triangle. Such an example would yield a positive divergence where no divergence had occurred. The wind stress data discussed in the next section also indicate that a convergence would have been expected between 21 and 23 March, so that a measurement anomaly may well have occurred.

Aerial imagery is useful for documenting the particular type of shearing motion. The measured net shear is indicated in Figure 6. From the measurements it is not possible to determine the exact type of slippage (it could be east-west or north-south). The en-echelon fractures to the north of Site β (Fig. 8) suggest that eastern floes are moving south relative to the western floes. This conclusion is verified by a detailed examination of the sequential photography (Hartwell 1972). Such a net shear agrees with the general motion of the Pacific Gyre   ̀at the measurements were taken on the edge of the gyre with the outer part moving more rapidly than the inner part, causing a north-south slippage of the type observed.

In summary, the experience of the 1971 pilot study has made it clear that sequential aerial imagery is a great help in interpreting strain observations in the pack ice. However, because significant large-scale strain events occur during time periods of the order of hours (e.g. the events of 11 to 12 March), it is quite easy to miss these events on synoptic aerial imagery taken at daily or greater intervals. It is also clear that, at present, imagery cannot provide the details needed for short-term correlations with meteorological factors, nor with the actual measurements of divergence, net strains and, most important, strain rates that are required for modeling purposes. At the present time, ground stations must still be relied upon for such critical ice dynamics information.

CORRELATION OF ESTIMATED WIND STRESS AND STRAIN

To estimate the wind stress field, the wind velocity field was calculated from barometric pressure readings by using the expression

$$u = -K_1 \frac{1}{\rho f} \frac{\partial P}{\partial y} - K_2 \frac{\partial P}{\partial x} \tag{8}$$

$$v = +K_1 \frac{1}{\rho f} \frac{\partial P}{\partial x} - K_2 \frac{\partial P}{\partial y} \tag{9}$$

where u and v are the x and y components of the wind velocity, P is the surface barometric pressure, ρ the air density, f the Coriolis parameter, and K_1 and K_2 are positive constants. The first terms in eq 8 and 9 represent the geostrophic wind with a modification expressed by the constant K_1 due to the effect of the frictional drag along the earth's surface. The frictional drag also causes the surface wind to have a component moving across the pressure isobars from high to low pressure (Petterssen 1969, p. 158). This component is represented by the second term in eq 8 and 9. The exact values of K_1 and K_2 may vary depending on the surface roughness. Here we are only concerned with qualitative correlations so the exact magnitudes are not critical. The divergence of the wind velocity field by the above equations is given by

$$\nabla \cdot \mathbf{v} = -K_2 \nabla^2 P . \tag{10}$$

Because of the approximate form of the barometric pressure data available to us, it was impossible to calculate meaningful shear components of the wind stress field; we therefore examined only correlations between the divergence of the ice and the divergence of the wind velocity field.

Assuming the wind stress on the ice is proportional to the wind velocity, a compressional stress will be introduced into the ice which is proportional to $\nabla \cdot \mathbf{v}$. This may easily be seen by considering adjacent infinitesimal sections of the ice and determining the force one section exerts on another due to the wind velocity gradient. With a constant velocity, for example, there would be no compressive stress because the external shearing force would be the same everywhere (neglecting variations in surface roughness).

To the extent that other external stresses, such as water stress, may be neglected, we would expect the convergence rate to scale with the compressional wind stress:

$$\dot{\epsilon}_{ii} = -K(\nabla^2 P) \tag{11}$$

where K is some parameter depending on the compactness. Intuitively this result might be expected to apply to very compact ice (high internal ice stress) which cannot move rapidly, so that Coriolis and water drag forces can be neglected.

The other extreme approximation that could be made would be to neglect the internal ice stress completely and consider, for example, unconstrained wind-driven ice on the open ocean. In this case certain theories yield an ice divergence rate proportional to $\nabla^2 P$ (with a sign opposite to that in eq 11).* Consequently, for purposes of empirical correlation $\nabla^2 P$ is clearly a useful parameter to compare with the divergence rate, with the sign of the correlation (if any) giving some indication of the internal ice stress magnitude.

To calculate $\nabla^2 P$, we utilized the surface barometeric pressure at the five locations indicated in Figure 1. With reference to this figure, pressure P_0 (at Camp 200) was provided by Hans Prelkkinen of the Canadian Polar Continental Shelf Project. These pressures were taken two to three times daily and were therefore extrapolated to six-hour intervals for comparison with other data. The position of pressure P_4 was taken to coincide with the location of Sachs Harbor on Banks Island, where surface pressures were available at six-hour intervals through the Canadian Meteorological Service. Other pressures were taken from surface isobaric charts supplied by the Canadian Meteorological Service, with stations 1 and 3 nearly coinciding, respectively, with the Mould Bay weather station on Prince Patrick Island and the Barter Island station on the Alaskan coast. Data were available at six-hour intervals and a time series of pressure data was constructed beginning at 1800, 7 March. All data were converted to GMT minus six hours, which was approximately the local time at Camp 200. The distance from P to the other pressure locations was about 320 km. From these five pressure values, the Laplacian of the pressure field was calculated by using a finite difference grid, with a the distance between the grid points:

$$\nabla^2 P = \frac{P_1 + P_2 + P_3 + P_4 - 4P_0}{a^2} . \tag{13}$$

Since here we are only concerned with examining the proportionality, we took $a/2 = 1$.

The results are presented in Figure 12 where we have plotted $-\nabla^2 P$ versus time, together with the divergence and divergence rate as functions of time. To smooth the pressure data, we removed the high frequencies with wavelengths shorter than 24 hours by passing a digital, low pass, unity gain filter over the $-\nabla^2 P$ curve. The filter has a pass band extending from 0 to $(1/96)$ hr^{-1} and a
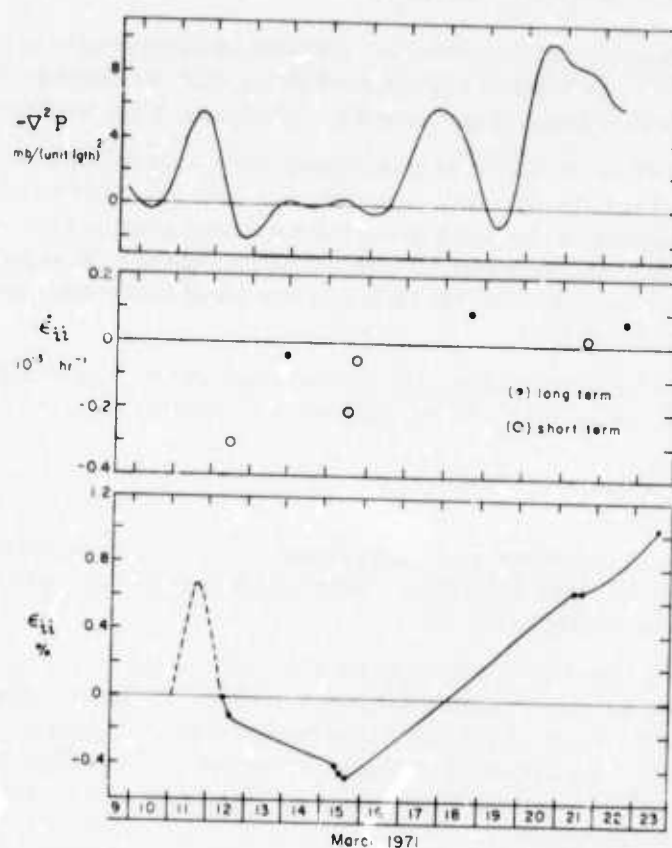
---

*Drew Rothrock, personal communication.

Figure 12. The Laplacian of the surface pressure field, the divergence rate and net divergence as functions of time. The unit length referred to is about 160 km. The dots on the divergence curve represent actual measurements, with the smooth curve simply connecting the measurements. The estimated divergence between 11 and 12 March was based upon visual ground observations, aerial photography and the linear strain along the $\alpha-\beta$ line.

stop band beginning at $(1/24)$ hr^{-1}. The filter was designed according to the procedure discussed by Hibler (1971) and had less than 0.6% side lobe error. Also note that in Figure 12 an extrapolated divergence curve is given for the time period between 11 and 12 March. This extrapolation is based on observations of the lead structure by using aerial photographs as well as ground observations, and is supported by the strain data taken along the $\alpha-\beta$ line during the same time period.

As can be seen, a reasonable correlation exists between the wind velocity field divergence and the ice divergence rate. The ice between 10 and 12 March indicated a divergence followed by a convergence which agrees with the estimated wind stress which is positive on the 11th and negative on the 12th. The trends of the later data after 15 March are also in agreement, i.e. the wind stress divergence generally increases and the ice divergence rate is positive.

In general, the results presented in Figure 12 suggest a correlation between the negative Laplacian of the pressure field and the ice divergence rate, although the data collected are not sufficient to permit us to make any definitive statements about such a correlation. This is especially true due to the complexity of the ice motion and the neglecting of other stresses besides wind stress. Clearly more complete data are needed to find out whether such correlations are generally noted.

CONCLUSIONS

A number of conclusions can be drawn from our study that have considerable bearing on the AIDJEX Project. These are as follows.

1. The analysis of mesoscale strains in the ice pack has proved to be of considerable interest. However, for such a study to be of maximum usefulness in the analysis of ice deformation, the strains should be determined at some fixed time interval. The measurements along strain line α-β on 11-12 March suggest that this time interval should be no greater than one hour. When significant ice deformation is occurring, an interval of 15 minutes would be even more satisfactory. We do not feel that tellurometers are a suitable instrument for such measurements unless they are automated so that only one end of a strain line has to be occupied.

Therefore, during the 1972 AIDJEX field program we used both continuous-wave and pulsed-laser range finders to determine the distances between the main camp and a series of remote towers.

2. It is important that strain measurements be made on several scales so that small scale floc-floe interactions as well as larger scale "continuous" deformation of the pack can be analyzed and related. Only when such studies are completed can sound statements be made about optimum sizes for strain arrays. An examination of the aerial imagery taken during the overflights (see, for example, Figures 2 and 8) as well as visual surface observations definitely suggest that in most cases the ice divergence as measured within the mesoscale array does indeed correlate with the ice divergence as observed over a larger area. Perhaps such mesoscale strains will serve as an adequate index of the macroscale deformation of the pack.

3. The correlations between fracture orientation and the orientation of the strain-rate ellipse, as well as between the lead density and the divergence rate, are encouraging. They suggest that aerial imagery may eventually produce useful quantitative information on the deformation of the ice pack. However, at the present time more combined ground truth and remote sensing data will be required both to increase our confidence in such correlations and to make them more quantitative.

4. In designing the present experiment it was always hoped that the observed correlation between the divergence of the wind field and the behavior of the ice would prove to be simple. The results are certainly encouraging in this regard. They suggest that detailed mesoscale studies of the relations between the wind flow characteristics and the two-dimensional deformation of the ice pack will prove to be most profitable.

ACKNOWLEDGMENTS

LITERATURE CITED

Bushuyev, A.V., N.A. Volkov, Z.M. Gudkovich and V.S. Loshchilov (1970) Results of expedition investigations of the drift and dynamics of the ice cover of the Arctic Basin during the spring of 1961. *AIDJEX Bulletin*, no. 3, p. 1-21. (Translated from Trudy AANII, Leningrad, vol. 257, p. 26-44, 1967.)

Browne, I.M. and A.P. Crary (1958) The movement of ice in the Arctic Ocean. In *Arctic Sea Ice*, U.S. National Academy of Sciences, National Research Council Publ. 598, p. 191-208.

Campbell, W.J. (1965) The wind driven circulation of ice and water in a polar ocean. *Journal of Geophysical Research*, vol. 70, no. 14, p. 3279-3301.

Campbell, W.J. (1968) Sea ice dynamics. In *Arctic Drifting Stations* (J.E. Sater, ed.), Arctic Institute of North America, Washington, D.C., p. 189-196.

Campbell, W.J. (1971) AIDJEX mesoscale strain measurements. *AIDJEX Bulletin*, no. 7, p. 59-62.

Curray, J.R. (1956) The analysis of two-dimensional orientation data. *Journal of Geology*, vol. 64, p. 117-131.

Dunbar, M. and W. Wittmann (1963) Some features of ice movement in the Arctic Basin. *Proceedings Arctic Basin Symposium, October 1962*, Arctic Institute of North America, p. 90-104.

Fredrickson, A.G. (1964) *Principles and applications of rheology*. Englewood Cliffs, N.J.: Prentice-Hall.

Glen, J.W. (1970) Thoughts on a viscous model for sea ice. *AIDJEX Bulletin*, no. 2, p. 18-27.

Hartwell, A. (1972) Airphoto analysis of ice deformation in the Beaufort Sea, March 1971. Part IV of this report.

Hibler, W.D. (1971) Design of small error low pass filters with arbitrarily sharp frequency cut-offs. *Transactions American Geophysical Union*, vol. 52, no. 11, p. 8478.

Mathews, J. and R.L. Walker (1965) *Mathematical methods of physics*. New York: Benjamin.

Mock, S.J., A. Hartwell and W.D. Hibler (1972) Spatial aspects of pressure ridge statistics. *Journal of Geophysical Research*, in press. (Also, see *AIDJEX Bulletin*, no. 12, p. 93-115.)

Nansen, F. (1902) The oceanography of the north polar basin. The *Norwegian Polar Expedition 1893-1896*, Scientific Results, vol. 3.

Nye, J.F. (1957) *Physical properties of crystals*. Oxford, England: Oxford University Press.

Petterssen, S. (1969) *Introduction of meteorology*. New York: McGraw-Hill, p. 158.

Reed, R.J. and W.J. Campbell (1962) The equilibrium drift of Ice Station Alpha. *Journal of Geophysical Research*, vol. 67, p. 281-297.

Ruzin, M.I. (1959) O vetrovom dreife l'dov v neodnorodnom pole davleniia. (The wind drift of ice in a heterogeneous pressure field.) *Trudy AANII*, Leningrad, vol. 226, p. 123-135.

Senior, C. Ward, W.I. Wittmann and F.L. Skiles (1968) Small-scale studies of deformation in the pack ice surrounding Arlis II. In *Arctic Drifting Stations* (J.E. Sater, ed.), Arctic Institute of North America, Washington, D.C., p. 225-237.

Sverdrup, H.U. (1928) The wind-drift of the ice on the North Siberian Shelf. *Scientific Results Norwegian North Pole Expedition with the "Maud", 1918-1925*, vol. 4, no. 1, 46 p.

Thorndike, A. (1970) Techniques for measuring strain rate. *AIDJEX Bulletin*, no. 2, p. 51-60.

PART II: STRUCTURE OF A MULTIYEAR PRESSURE RIDGE

by

A. Kovacs, W.F. Weeks, S. Ackley and W.D. Hibler, III

ABSTRACT

Three transverse profiles across a large pressure ridge located in the Beaufort Sea are presented. The ridge sail extended 4 m above sea level and the ridge keel 13 m below. The cross sections of the ridge keel can be described as roughly semicircular, suggesting that form drag coefficients for flow transverse to the long axes of multiyear ridges may be as high as 0.8. Examination of several salinity, temperature and brine volume profiles shows that much of the ice in the ridge has a very low salinity and is quite strong. All the inter-block voids that initially existed in the ridge at the time of its formation have been completely filled with ice. These observations, coupled with icebreaking experience, indicate that multiyear ridges are, indeed, significant obstacles to even the largest icebreaking ship and should be avoided if possible. A very large first-year ridge with a sail height of 12.8 m is also described. This is the largest free floating ridge yet recorded.

INTRODUCTION

A major problem in the development of the Arctic is the lack of a cheap, reliable, large volume transportation system capable of year-round operation. In many arctic areas such as the Canadian Archipelago, a sea route seems to be the only possible solution. The principal obstacle to the development of such a route is, of course, the highly variable and at times extremely formidable sea ice cover. This ice cover has restricted the operation of surface ships to a few months each summer. Even then there are areas where icebreaker assistance is required. However, the recent test cruises of the *S.S. Manhattan* clearly showed that "super" cargo vessels can be designed and built within the framework of current marine technology that are capable of winter navigation in arctic waters. To optimize any such design one must fully understand the nature of the more significant obstacles that can be expected in the ice cover. Similar information is also needed for the safe design of offshore structures and harbor facilities. Most such structures are fixed, and cannot maneuver around the more obvious obstacles but must take the ice as it comes.

With the exception of ice islands, which are rare and can usually be easily recognized by radar, the most formidable obstacles in the ice pack are the pressure ridges and hummocks, i.e. those linear to irregular accumulations of ice caused by the compressive and shear interactions between ice floes; such features may become very large indeed. The highest free-floating ridge sail that we are aware of was 12.8 m above sea level whereas the deepest keel recorded in submarine sonar data extended some 47 m below sea level (Lyon, personal communication). Impressive as these figures are, ridges of this size fortunately appear to be quite rare. Indeed, ridge sails in excess of 5 m are rare.

Operational experience has shown that the bulk properties of geometrically similar ridges may vary greatly. For instance the *S.S. Manhattan* was able to progress with relative ease through most

first-year ridges but encountered considerable difficulty with apparently similar multiyear ridges.
Actually it might be expected that the properties of first-year pressure ridges would be highly
variable. This would primarily depend upon the degree of bonding developed between the ice blocks
that make up the ridge. The best bonding should develop when the ice being incorporated into the
ridge is very cold. Many of the first-year ridges that have been studied in detail were poorly bonded
(Weeks et al. 1971). In a multiyear ridge, on the other hand, the meltwater produced during the sum-
mer can drain downward into the core of the ridge. Here the water refreezes, cementing the ice
blocks together into a solid, resistant mass of low salinity ice. At least two melt seasons are
usually required for the voids between the ice blocks to become completely filled.* That the core
of an old multiyear ridge was usually a particularly resistant obstacle was recognized quite early
by Russian investigators (Burke 1940, Zubov 1945).

Considering that multiyear ridges are commonly considered the most formidable obstacles in
the pack, it is amazing that there are no detailed observations of either their overall structure or
the state of the ice forming them. The only published investigation of a multiyear ridge of which
we are aware is by Spichkin (Gakkel' 1959) who determined the cross-sectional profile of such a
ridge where it was intersected by a lead. This revealed that the underwater portion of the ridge
was massive compared with the above-water portion. No other data were apparently obtained.

This report presents the results of a study designed to add additional information on the struc-
ture and properties of multiyear ridges. The observations were made in the Beaufort Sea roughly
550 km north of Tuktoyaktuk, Northwest Territories, at Camp 200 of the Canadian Polar Continental
Shelf Project, the base of the 1971 Arctic Ice Dynamics Joint Experiment (AIDJEX) pilot study.
The observations include the determination of the surface relief of the ridge and the snow thickness
using standard surveying techniques, the profiling of the ridge keel using a sonar technique utilized
by Kovacs (1971), and the sampling of the ice in the inner portions of the ridge by drilling and coring.

PROFILES

An aerial view of the ridge is shown in Figure 1. The location of each of the three profiles is
marked. The detailed cross sections are shown in Figure 2. This figure also shows the longitudi-
nal ridge crest elevation profile on which the location of each transverse cross section is indicated.
In the area profiled, the ridge crest elevation ranged between 1.5 and 4.0 m. Also the three ice
thicknesses at the intersections of the longitudinal and the transverse profiles are plotted. A fence
diagram showing the cross sections in perspective is given in Figure 3. Although the actual dis-
tance between the cross sections is 8 m, in this drawing the cross sections have been laterally dis-
placed from one another in order to provide an unobstructed view of their geometry. The highest
elevation on cross section A was 3.9 m, whereas its keel extended to a depth of some 12 m. Simi-
larly, on cross section B the ridge sail was 3.9 m high and the keel some 13 m deep. In cross
section C only half of the subsurface contour of the keel was determined. By using the slope of
the contoured portion of the keel and the keel contours from cross sections A and B as guides, we
estimate the keel depth of profile C to be 11.5 m. The height of the sail on cross section C is
3.4 m. Using the values of sail heights and keel depths reported above, the average freeboard to
depth ratio for this multiyear ridge was calculated to be 1 to 3.3. This ratio is lower than the 1 to
4.5 ratio recently determined by Kovacs (1971) for first-year pressure ridges but is in excellent
agreement with the ratio proposed by Wittmann and Schule (1966) for the Makarov pressure ridge
model. The cross sections also clearly show that the subsurface portion of the ridge is significantly
wider than the above-water portion. Note that in cross section B-B there is a major discrepancy

---

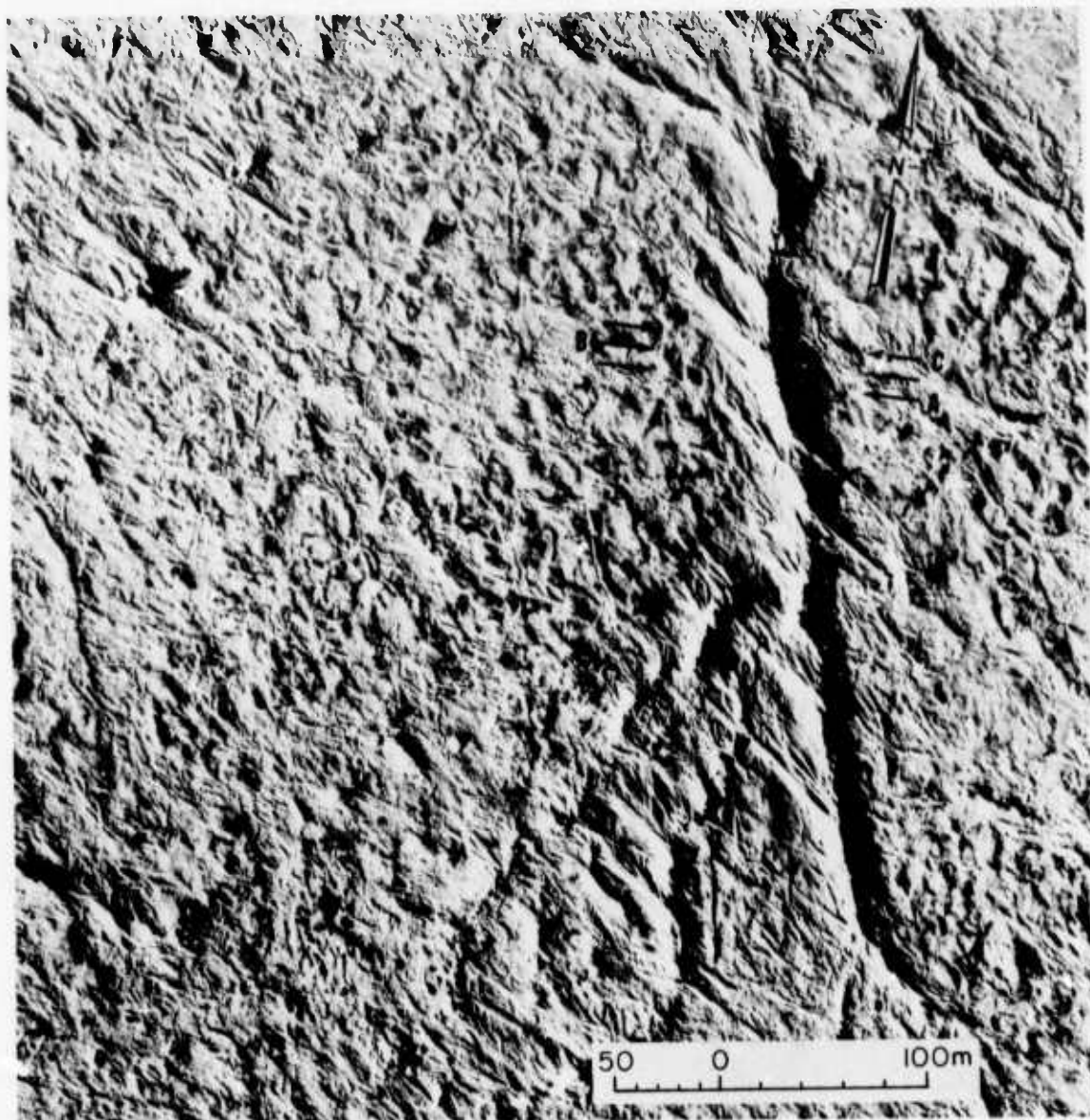*Allan Gitt, personal communication.

Figure 1. Aerial view of the multiyear ridge studied (center of photograph) and the surrounding terrain. The photograph was taken after the study was completed and a storm had swept the ice surface clean of a major portion of its snow cover. First-year ice can be seen in the upper left-hand corner. The position of each profile line is marked.

between the ice thickness obtained by drilling and by sonar. We have no explanation for this except to observe that the drilled thickness is a point measurement whereas sonar "samples" an appreciable area. In a general way the transverse profiles of the ridge keel can be described as roughly semicircular to semielliptical. Drag coefficients for such form roughness elements are discussed in Hoerner (1965) and range from 0.8 for a semicircular shape to 0.5 for a semielliptical shape. Because of the "streamlining" effects of the summer melt season and the snowdrifts, the drag coefficient for the ridge sail would be significantly lower.
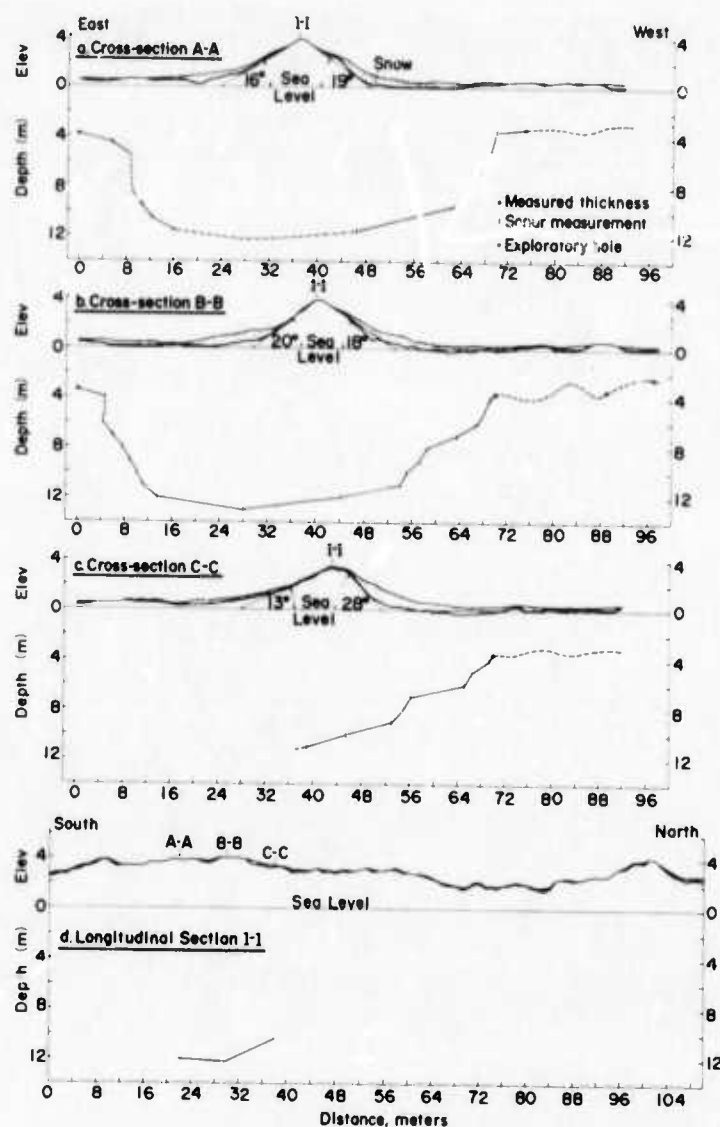
Figure 2. Transverse and longitudinal cross sections of the multiyear ridge.

In most of the profiles, the upper ice surface at the edges of the ridge sails shows a downward deflection. This phenomenon has been observed in most first-year ridges studied (Weeks and Kovacs 1970, Kovacs 1971). In the case of first-year ridges this deflection is clearly caused by load transfer from the sail to the surrounding plate ice as a result of an isostatic imbalance produced during the initial ice pile-up. In the current ridge the deflection is believed to be partly related to snow loading and partly to keel ablation. The latter would cause the ridge to subside in the process of seeking isostatic equilibrium. It is expected that during the next melt season these depressions will fill with meltwater from the ablating ridge sail. When these ponds refreeze the following fall, these deflected areas will probably no longer be discernible.

The slope of the ridge sail was determined by measuring the angle of the profile lines shown in the cross-sections (Fig. 2). The slope varied between $12°$ and $28°$ and averaged $19°$. This is $5°$ less than the average surface slope determined by Kovacs (1971) for first-year pressure ridges.
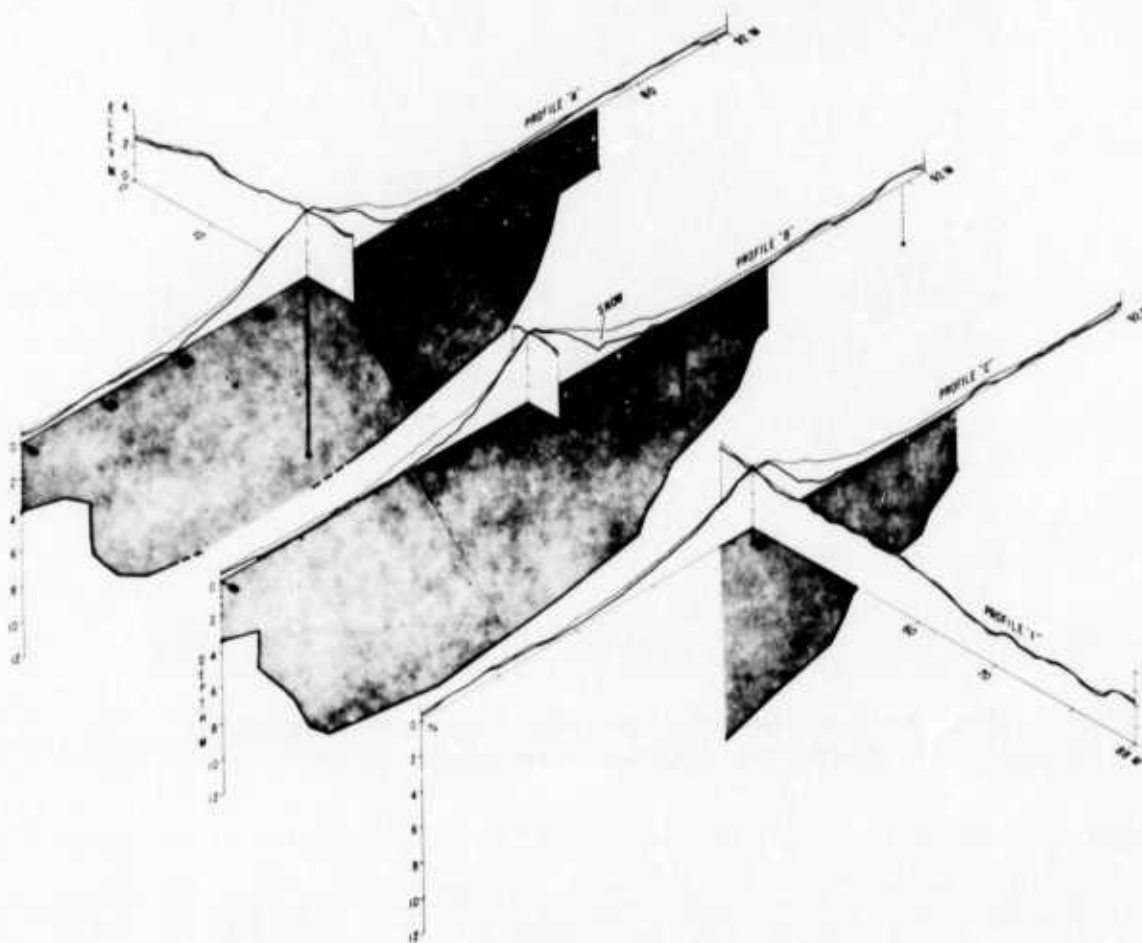
Figure 3. Fence diagram showing the relative positions of cross sections A, B and C.

This difference, which may well be general, is undoubtedly due to the modification of the shape of the ridge sail by ablation. No attempt was made to determine the slope of the keel which has a bowl-like shape.

The fact that pressure ridges act as snow fences is again clearly illustrated in the cross sections. The greatest snow accumulation was in excess of 1 m and occurred along the toe of the sail.

INTERNAL PROPERTIES

Exploratory coring at meter 37 on cross section A, at meters 50 and 60 on cross section B, and at meter 43 on cross section C (see Fig. 2) revealed no cavities of any type and showed the ice to be sound, as indicated by augering resistance. There were no wide cracks or leads that transected the ridge so an actual profile could not be examined. However Kovacs (unpublished data) has examined cross sections of several similar multiyear ridges in the Beaufort Sea. Figure 4 shows a general view of such a ridge which has split. Note that the ice is extremely massive. Figure 5 shows a detail of the internal structure of another multiyear ridge. The distribution and size of the
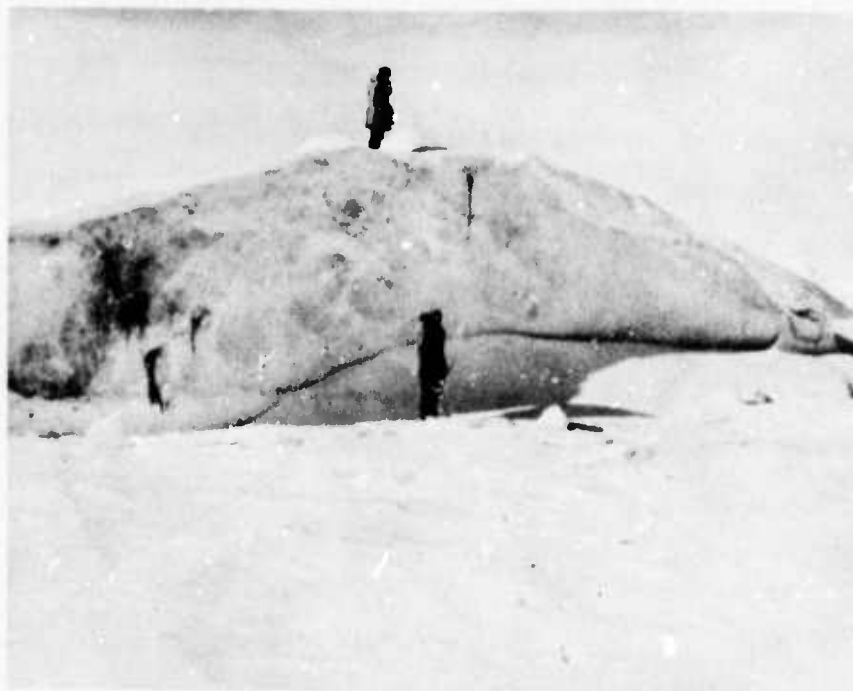
Figure 4. View of the sail of a multiyear pressure ridge located in the
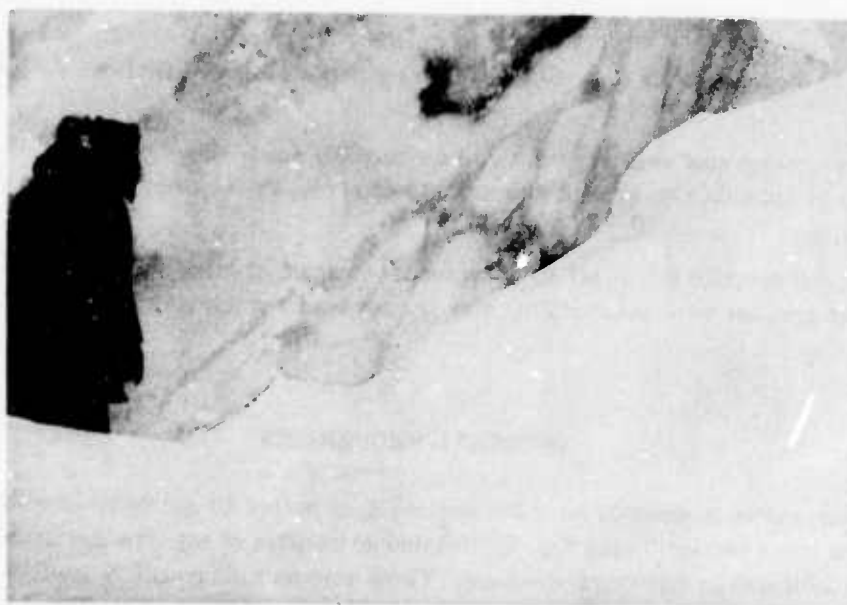Beaufort Sea. Note the massive nature of the ice.

Figure 5. Internal structure of a multiyear pressure ridge from the Beaufort
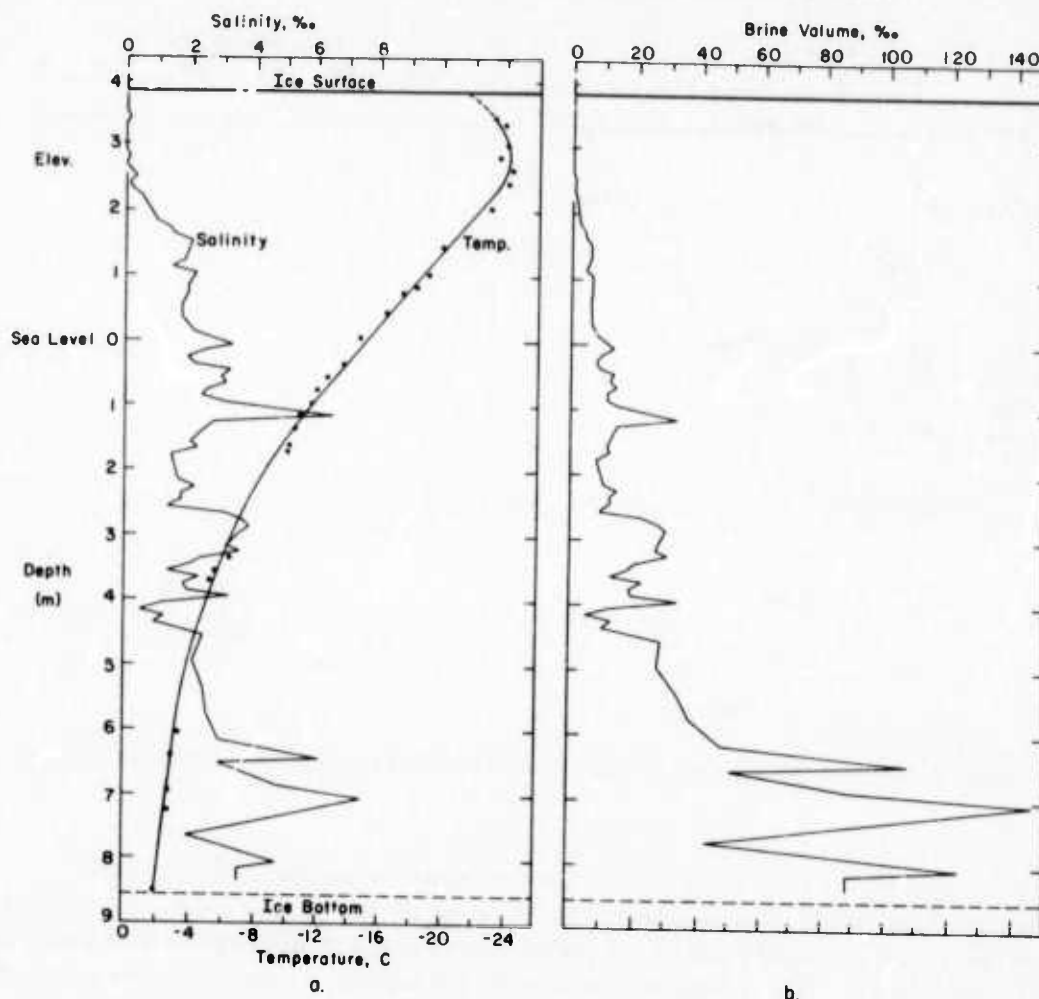Sea. Note the lack of voids between the angular blocks composing the ridge.

Figure 6. Salinity, temperature and brine volume profiles of the ice at Meter 37 on cross section A.

subangular ice blocks incorporated into this ridge as well as the refrozen water between the blocks is clearly shown. The lack of interblock voids is striking. Note also the dark plankton band within the largest ice block. Based on this information, our coring observations and, as mentioned earlier, the difficulties experienced when ships attempt to break through multiyear ridges, we suggest that the ice blocks composing most multiyear ridges are completely bonded together by the freezing of interstitial water.

Figures 6, 7 and 8 show the salinity, temperature and brine volume profiles obtained by coring into the ridge. Figure 8 also gives the density profile of the ice to a depth of some 3.5 m. All the ridge profiles show the salinity to be virtually zero at the surface.

As shown in Figures 6 and 7 the ice remains fresh for a depth of 1 m. The near-surface ice was also found to contain a large number of air bubbles, suggestive of extensive brine drainage. This increase in air content is reflected in the sharp decrease in ice density near the top of the ridge sail (Fig. 8). Figures 9 and 10 show similar profile data obtained from the multiyear ice adjoining the ridge. In all of the profiles there is a gradual increase in the salinity with depth. At the bottom of the ridge the salinity averages roughly 4.5 ‰ whereas at the bottom of the presumably undeformed multiyear ice, the value is very slightly higher. All the salinity profiles show
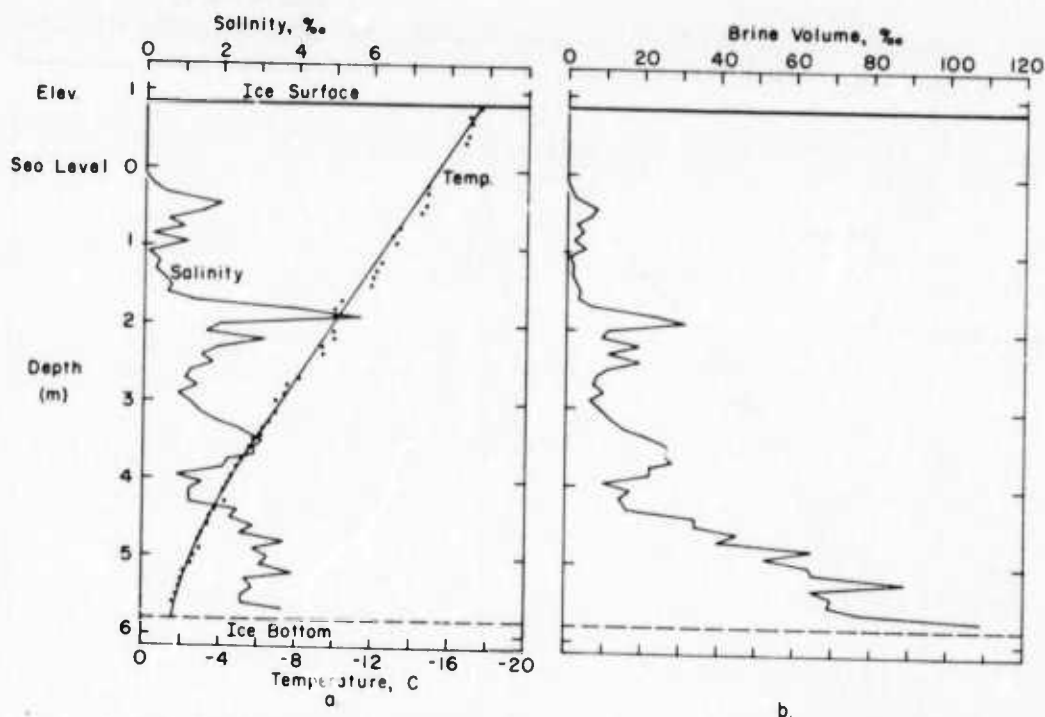
Figure 7. Salinity, temperature and brine volume profiles of the ice at Meter 50 on cross
section B.

the wide scatter that is particularly characteristic of multiyear ice (Schwarzacher 1959,
Untersteiner 1968) and to a lesser extent of first-year ice (Weeks and Lee 1962). A point of interest
is that much of the ice represented by the profiles shown in Figure 10 formed in a melt pond and is,
in fact, first-year ice. This is suggested by both the ice topography surrounding the coring site and
the salinity profile itself. The pond clearly exhibited a pronounced salinity stratification prior to
freeze-up.

The temperature profiles shown in Figures 6, 8, 9 and 10 all show by the curvature in their
upper portions that a gradual warming of the ice cover is under way. This trend is, however, not
yet apparent in Figure 7 where the thick snow cover formed in the lee of the ridge has caused a
delay in the arrival of the warming trend at the ice surface.

The brine volume profiles shown in Figures 6, 7 and 8 are as expected: effectively nil at the
surface with a gradual increase toward the bottom in response to the increase in the temperature
and salinity values. Because of the time of year (March), the ice temperatures would be expected
to be near their annual minimum corresponding to a maximum in ice strength (Weeks and Assur 1968).

If we assume that the overall ridge is in isostatic equilibrium we can calculate a mean density
for the ridge ice by determining the ratio of the ice above sea level to the ice below sea level. The
snow cover was converted to an equivalent ice volume by assuming an average snow density of
0.45 g cm^{-3}. The observed ratio was 1 to 7.7, corresponding to a mean ice density of 0.91 g cm^{-3},
in good agreement with an average measured density of 0.90 g cm^{-3}. This suggests that multiyear
ridges may be close to being in overall isostatic balance. Although a sample of one can hardly be
considered as proof of this conjecture, it is reasonable to assume that this well may be the case.
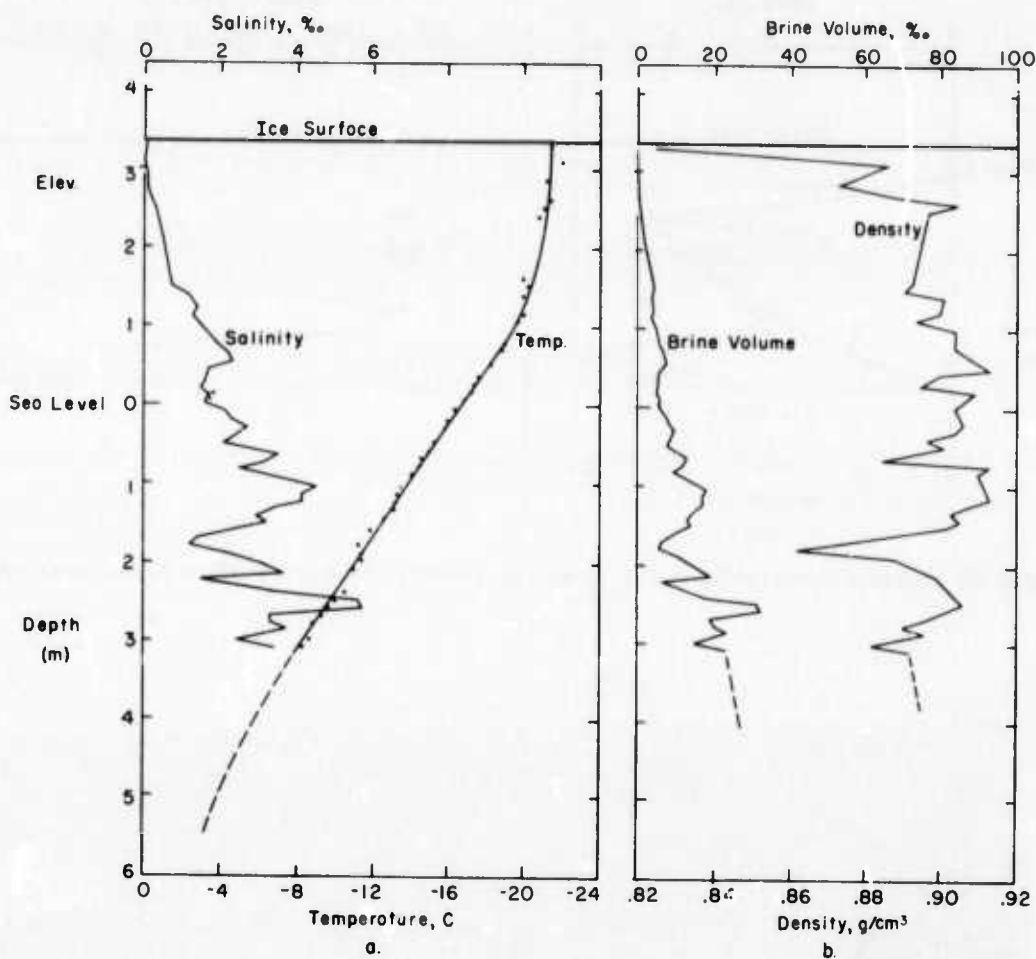
Figure 8. Salinity, temperature, brine volume and density profiles of the ice at Meter 43
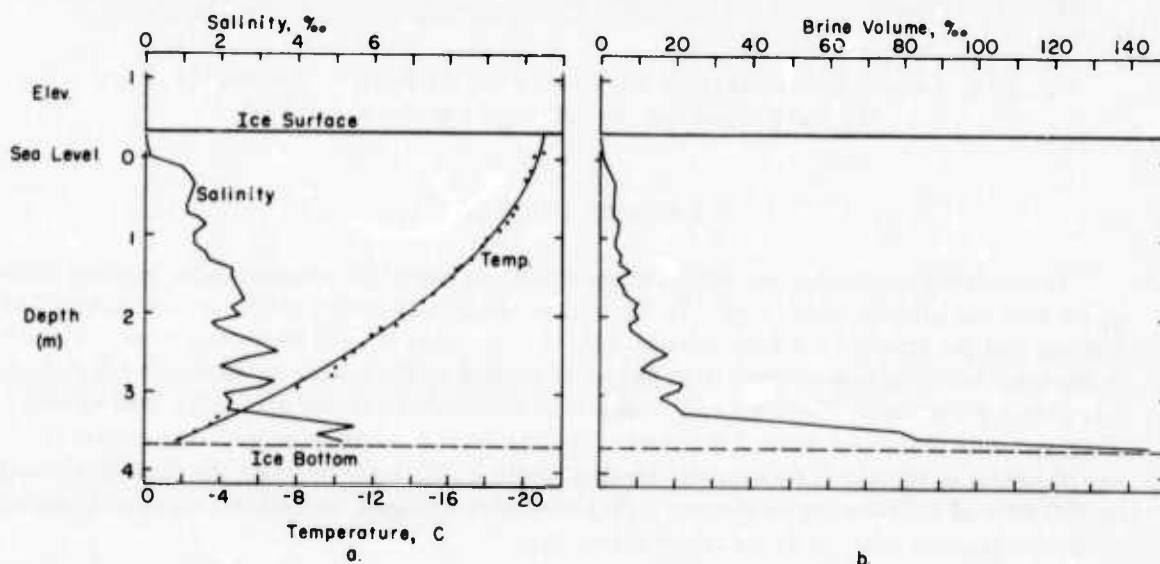on cross section C.

Figure 9. Salinity, temperature and brine-volume profiles of the ice at Meter 89 on cross section B.
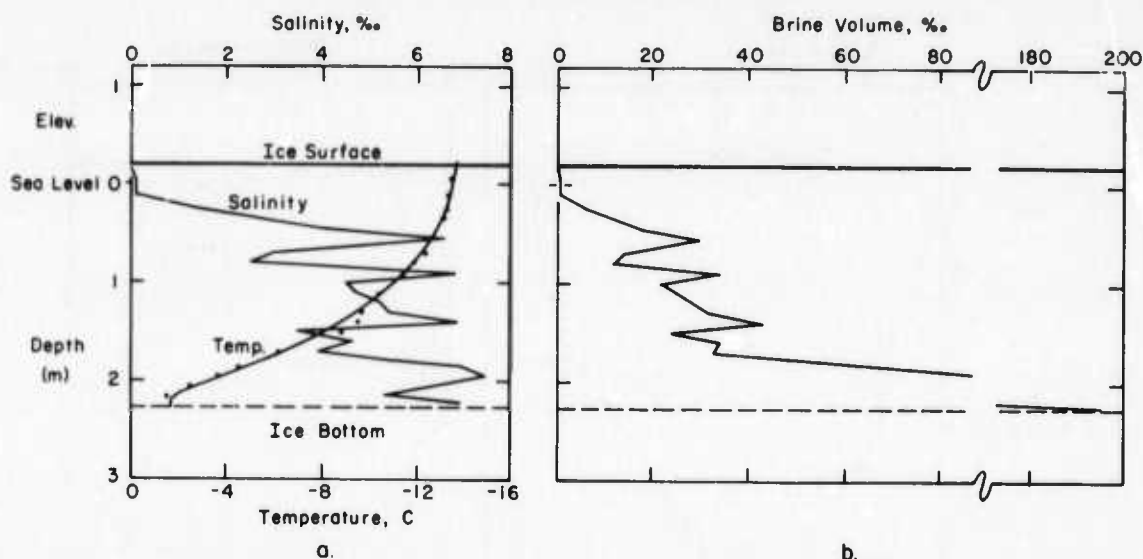
Figure 10. Salinity, temperature and brine volume profiles of the ice at Meter 97 on cross section B.

*Figure 11. Large free-floating ridge sail observed in the Beaufort Sea near Camp 200.
The highest point on the sail is 12.8 m above sea level.*

LARGEST RIDGE SAIL

An extremely large pressure ridge was observed near one of the oceanographic stations (about 10 km from the AIDJEX base camp). To the best of our knowledge this ridge has the highest free-floating sail yet sighted (and documented) in the Arctic Ocean (12.8 m above sea level). The ice in the ridge was first year and the large ice block located on the top of the ridge was 2.2 m thick, 3 m wide and 7 m long. The ridge had clearly been active in the recent past and a lead existed along one side of it at the time of our visit. The high portion of the ridge was very limited in lateral extent ($\approx$ 100 m). If we estimate the keel depth of this ridge by using the (keel depth/sail height) ratio of 4.5 observed by Kovacs (1971) on first-year ridges, we obtain a value of 57 m, some 10 m more than the deepest previously observed keel.

CONCLUSIONS

The multiyear ridge studied in this report was large and structurally massive. All the initial voids between the blocks composing the ridge have been subsequently filled with solid ice. In addition much of the ice in the ridge has a very low salinity. It is, therefore, reasonable to assume that ridges of this type represent a significant impediment to shipping and should be avoided if at all possible. They also represent a major problem in the design of potential offshore structures such as shipping terminals and drilling platforms.

ACKNOWLEDGMENTS

LITERATURE CITED

Burke, A.K. (1940) Sea ice. Izdatel'stvo Glavsevmorputi, Leningrad (in Russian), 95 p.

Gakkel', Ia. Ia. (1959) Tectonic deformations modeled naturally in sea ice. Izvestiya Vsesoyuznogo Geograficheskogo Obshchestava, vol. 91, no. 1, p. 27-41. (DRB Translation T328R).

Hoerner, S.F. (1965) Fluid-dynamic drag. New Jersey: Hoerner, 148 Busteed Drive, Midland Park 07432, 415 p.

Kovacs, A. (1971) On pressured sea ice. International Sea Ice Conference, Reykjavik, Iceland, 25 p.

Schwarzacher, W. (1959) Pack ice studies in the Arctic Ocean. Journal of Geophysical Research, vol. 64, p. 2357-2367.

Untersteiner, N. (1968) Natural desalination and equilibrium salinity profile of perennial sea ice. Journal of Geophysical Research, vol. 73, p. 1251-1257.

Weeks, W.F. and A. Assur (1968) The mechanical properties of sea ice. Proceedings Conference on Ice Pressures Against Structures, Laval University, 1968. National Research Council of Canada, Associate Committee on Geotechnical Research, Technical Memorandum No. 92, p. 25-78.

Weeks, W.F. and A. Kovacs (1970) The morphology and physical properties of pressure ridges: Barrow, Alaska, April 1969. International Association of Hydraulic Research Symposium on Ice and its Action on Hydraulic Structures, Reykjavik, Iceland, 7-10 September 1970, Paper 3.9, 8 p.

Weeks, W.F., A. Kovacs and W.D. Hibler (1971) Pressure ridge characteristics in the arctic coastal environment. Proceedings First International Conference on Port and Ocean Engineering under Arctic Conditions, Technical University of Norway, Trondheim, vol. 1, p. 152-183.

Weeks, W.F. and O.S. Lee (1962) The salinity distribution in young sea ice. Arctic, vol. 15, p. 92-108.

Wittmann, W. and J.J. Schule (1966) Comments on the mass budget of arctic pack ice. Symposium on Arctic Heat Budget and Atmospheric Circulation. RAND Corporation (RM-5233-NSF), p. 215-246.

Zubov, N.N. (1945) Arctic ice. Izdatel'stvo Glavsevmorputi, Moscow (in Russian), 160 p.

PART III. TOP AND BOTTOM ROUGHNESS OF A MULTIYEAR ICE FLOE

by

W.D. Hibler, III, S.F. Ackley, W.F. Weeks and A. Kovacs

ABSTRACT

A spectral study of the snow and ice topography on a multiyear ice floe has shown that the snow cover, although attenuating the roughness amplitude of the ice surface, does not cover it completely. In general the snow surface variance is lower by a factor of $\frac{1}{3}$ to $\frac{1}{4}$ than the ice surface variance. The correlation between snow and ice surface roughness is highly significant for long wavelengths (> 8 m), but fails to be significant for short wavelengths (< 4 m). These results agree with what might be expected intuitively in that long wavelength variations are not masked appreciably while short wavelength variations are well hidden. Although the ice sheet as a whole is in free-floating, isostatic equilibrium, pronounced local deviations from isostatic equilibrium are common. The trend is for ice drafts to deviate more than expected from isostasy for thin ice and less than expected for thick ice. Estimates are also made of the number of ice thickness measurements required to obtain the mean thickness of the multiyear floe to any specified accuracy.

INTRODUCTION

Little work has been done on the correlation between the roughness of the upper and lower surfaces of sea ice. At first thought this might appear surprising inasmuch as the surface roughness is important in controlling the wind and water drag exerted on the ice. However, there is still no indirect method of determining the thickness of sea ice, much less a method of doing this remotely as a continuous profile. Drilling is, of course, time consuming and tiring, but is virtually the only means of determining freeboard and draft at a point. Present observations on ridging in first-year ice suggest that although lack of local isostatic equilibrium is common, a good overall correlation between top and bottom roughness is to be expected. Whether this is generally true for multiyear ice has not been previously studied.

The following is a preliminary look at the freeboard to draft correlation problem in multiyear ice. In addition a study of the relation between the snow surface and the true ice surface of the multiyear floe was completed. This is of interest because remote sensing techniques using laser profilometry record the elevation of the snow surface and not the true ice surface.

The study site was part of a multiyear floe approximately 5 km^2 in area, located in the Beaufort Sea at the site of the 1971 AIDJEX pilot study about 550 km north of Tuktoyaktuk, N.W.T. An aerial photograph of the study area is shown in Figure 1 of Part II. Figure 1 of Part III shows the plan drawing of the profile lines where 1-1 refers to the ridge shown in the aerial photograph. At the time when the photo was taken the ice surface was effectively scoured free of the snow that is shown in Figure 2. The structure of the large multiyear pressure ridge in the right portion of the figure was also studied and is the subject of another paper (Kovacs et al. 1972). The differences
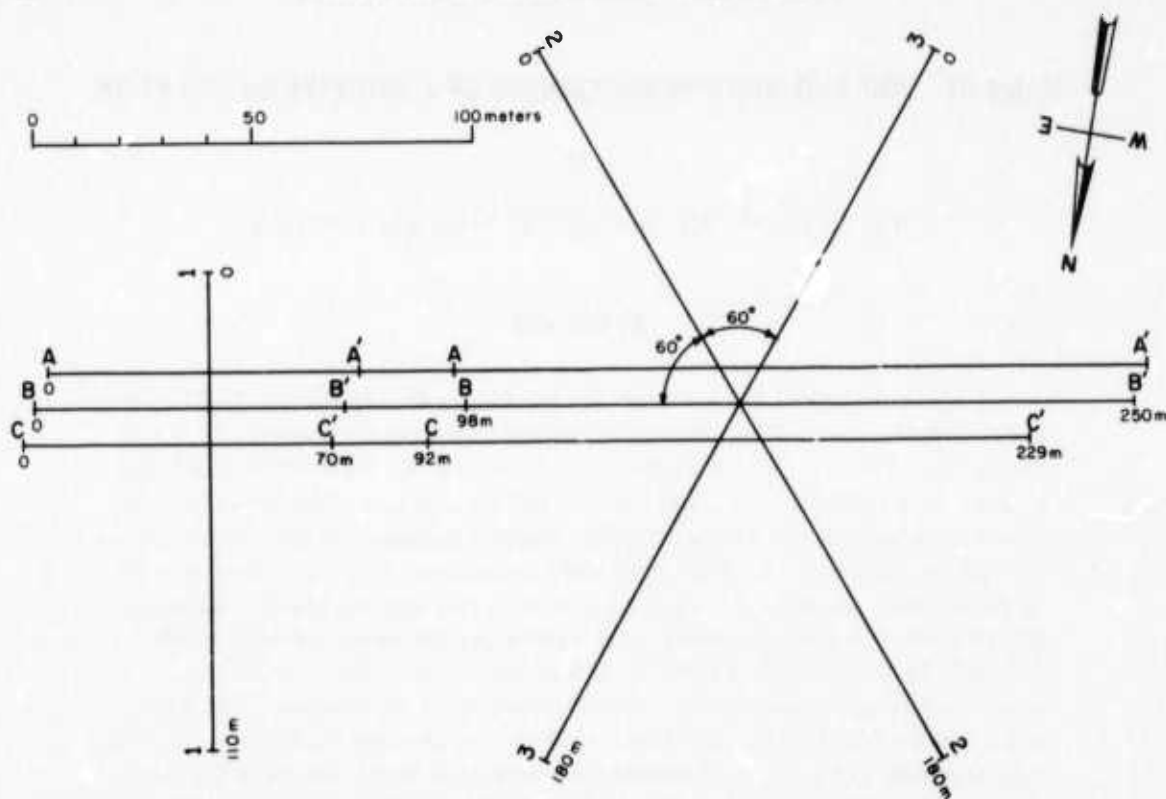
Figure 1. The locations of the profile lines along which snow and ice elevations and random thickness measurements were taken (see Fig.　　Part II for airphoto of multiyear floe).

in roughness between first- and multiyear ice are quite evident from the "freckled" appearance of the multiyear ice as shown in the figure compared to the smooth first-year ice whose surface is marked only by snowdrift features.

Figure 2 shows cross-sectional views of the five elevation profiles that were studied. The snow depth and the ice elevation above sea level were determined at 1-m intervals along each profile by leveling. In addition ice thicknesses were determined by drilling at 31 locations. The figure clearly shows the undulating topography characteristic of multiyear floes.

RESULTS

Snow surface/ice surface corelations

In much remote sensing data, in particular in laser profiles and digitized roughness plots made from aerial photographs, the surface of the snow is "seen" rather than the true ice surface. It was apparent by observation at the study site that after a storm, snow drifting could change the effective surface sampled by remote sensing. From a visual examination of the profiles shown in Figure 2 it initially appears that the snow covers up much of the interesting roughness. A more detailed examination of the surface roughness indicates that this may not be the case. Figure 3 shows both snow and ice spectra along all profiles. The spectra were calculated using a Hamming spectral window and a maximum wave number of 50. The confidence limits are indicated. Computational detail and a discussion of the particular interpretation of the power spectra of sea ice can be found
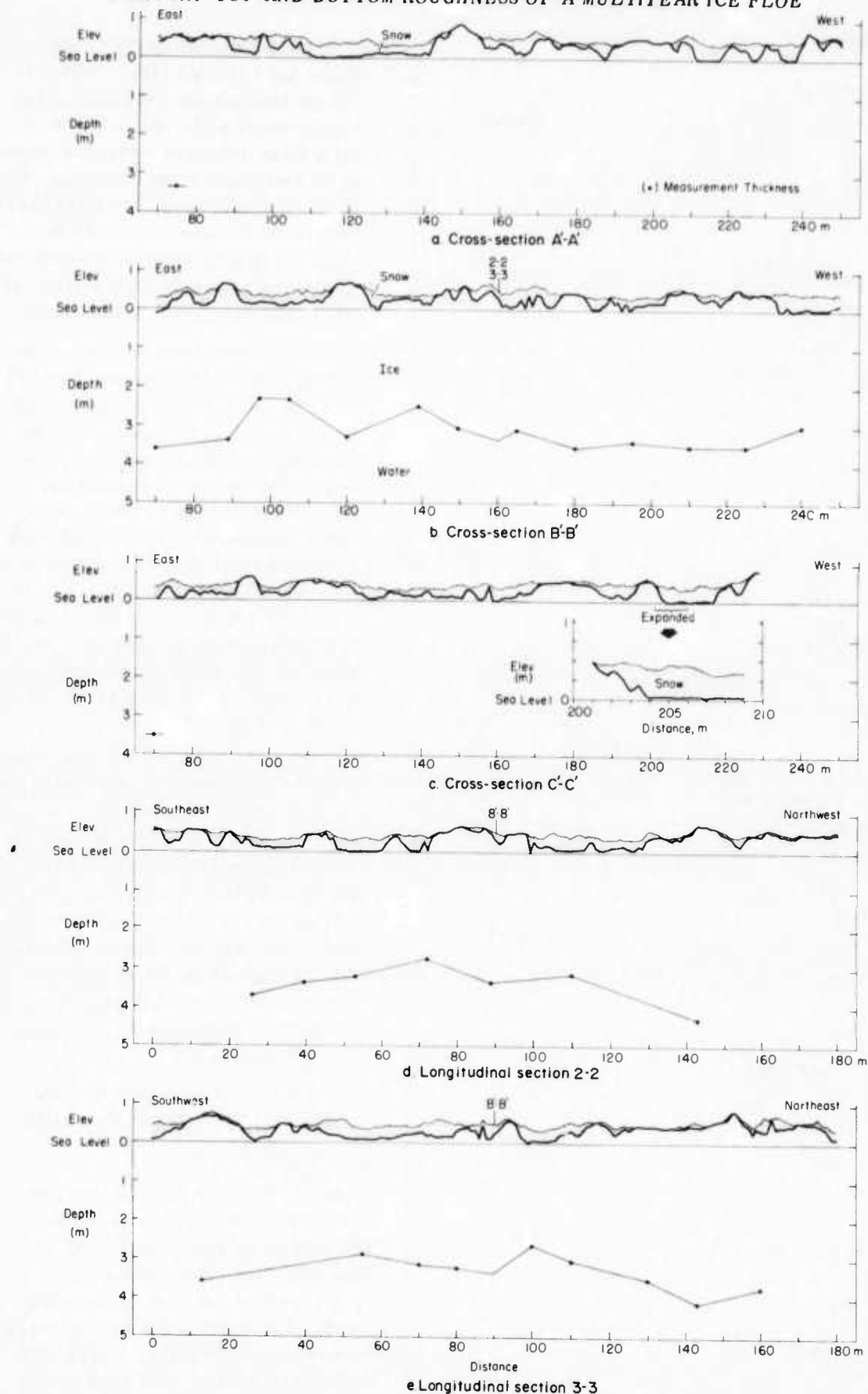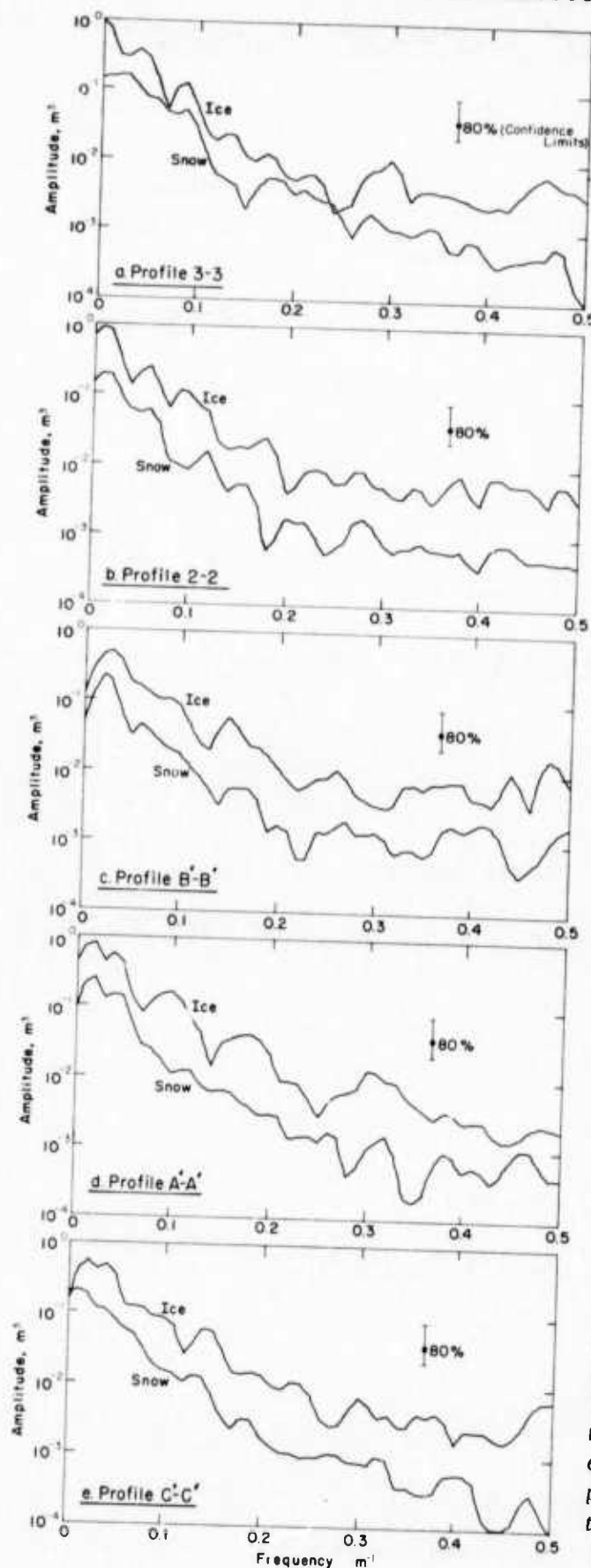
Figure 2. Cross sections of the 5 profiles studied, illustrating snow and ice elevations and random thicknesses. The vertical scale is exaggerated by a factor of 10 compared to the horizontal scale.

in Blackman and Tukey (1958) and Hibler and LeSchack (1972) respectively. For our analysis here, the spectra may be considered a plot of the amount of variance or roughness versus the frequency or wavelength of the roughness. The plots shown in Figure 3 are normalized to the total variance so that the area under the spectral curve in any given frequency band gives the total variance or mean square roughness in that region.

From Figure 3 we see that as expected the spectral components for the snow surface are generally all smaller by a factor of $\frac{1}{3}$ to $\frac{1}{4}$ than the spectral components of the ice surface. This means that the roughness has been smoothed out and consequently wind stress measurements (Banke and Smith 1971) might be expected to change as the snow cover shifts. Taking the square root of the variance to be some measure of the mean roughness height we see that a factor of 2 variation in the mean roughness height can easily be caused by shifts in the snow cover.

The other point obvious from Figure 3 is that the general shapes of the snow surface and ice surface spectra are much the same for the same profile, with many of the same spectral peaks occurring in the snow surface spectrum as in the ice surface spectrum. These peaks indicate that the snow cover, although attenuating the amplitude of the ice surface, does so in such a way that the dominant spectral components, especially at low frequencies, are still observable.

To obtain a more quantitative analysis of how well the snow surface correlates

Figure 3. *Snow elevation and ice elevation power spectra along five profiles. The spectra are normalized so that the total area under the spectral curves equals the total variance for any given profile. The y-axis amplitude represents the variance per frequency interval. The 80% confidence limits are as indicated.*
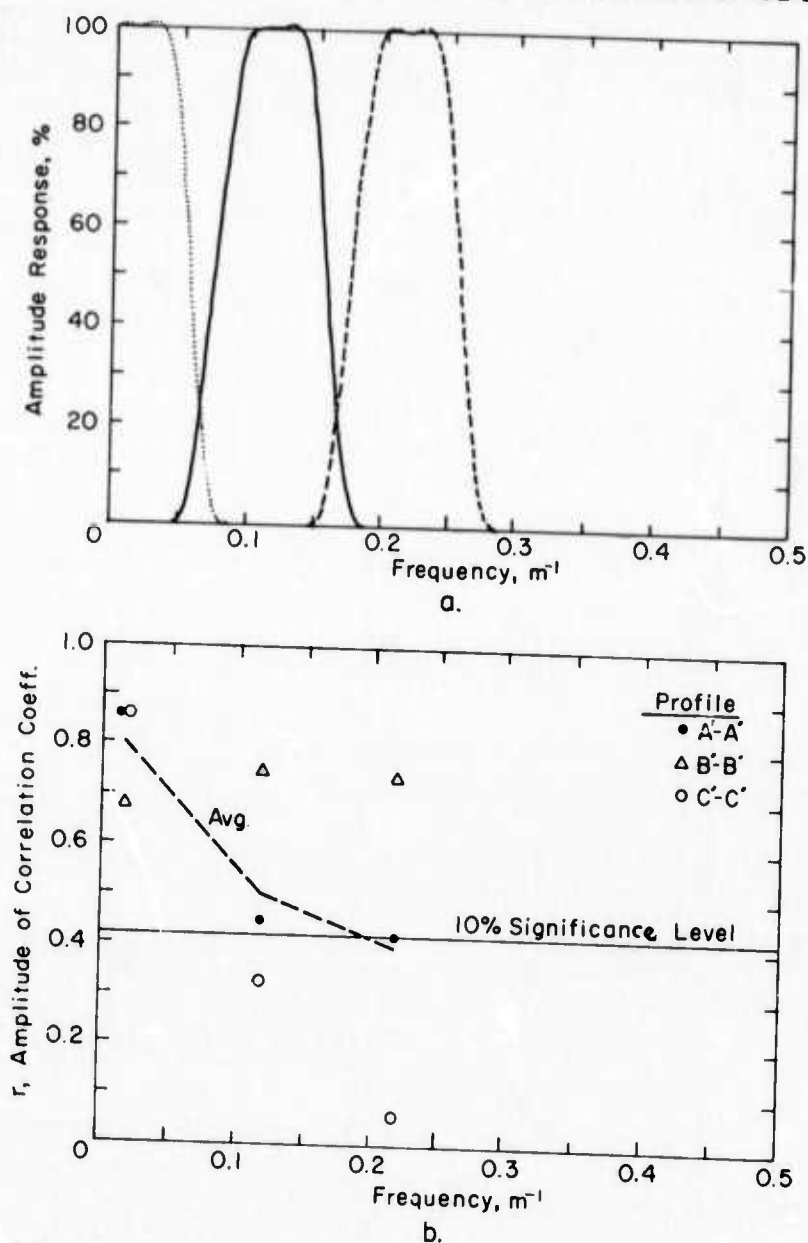
Figure 4. Frequency response of convolution filter weights (a) and correlation coefficient amplitudes (b) for each filtered profile. The line connects the average correlation results in each pass band. The 10% confidence level represents the value that would be exceeded 10% of the time by the correlation coefficient obtained from 18 random samples of uncorrelated normal variates.

with the ice surface at different frequencies, we passed three band pass filters over the parallel snow and ice profiles A'-A', B'-B' and C'-C', and plotted the results. This procedure has the advantage of indicating at what position correlation takes place. We also calculated the correlation coefficient between snow and ice profiles for each band passed result. When determining the degrees of freedom for calculating the significance of the correlation coefficient for a band pass filtered profile, the total number of data points is multiplied by the fraction of the spectrum filtered. The frequency response of the filters (less than 1% side lobe errors in all cases) together with the average correlation coefficient for each frequency band is given in Figure 4. The 10% significance level for
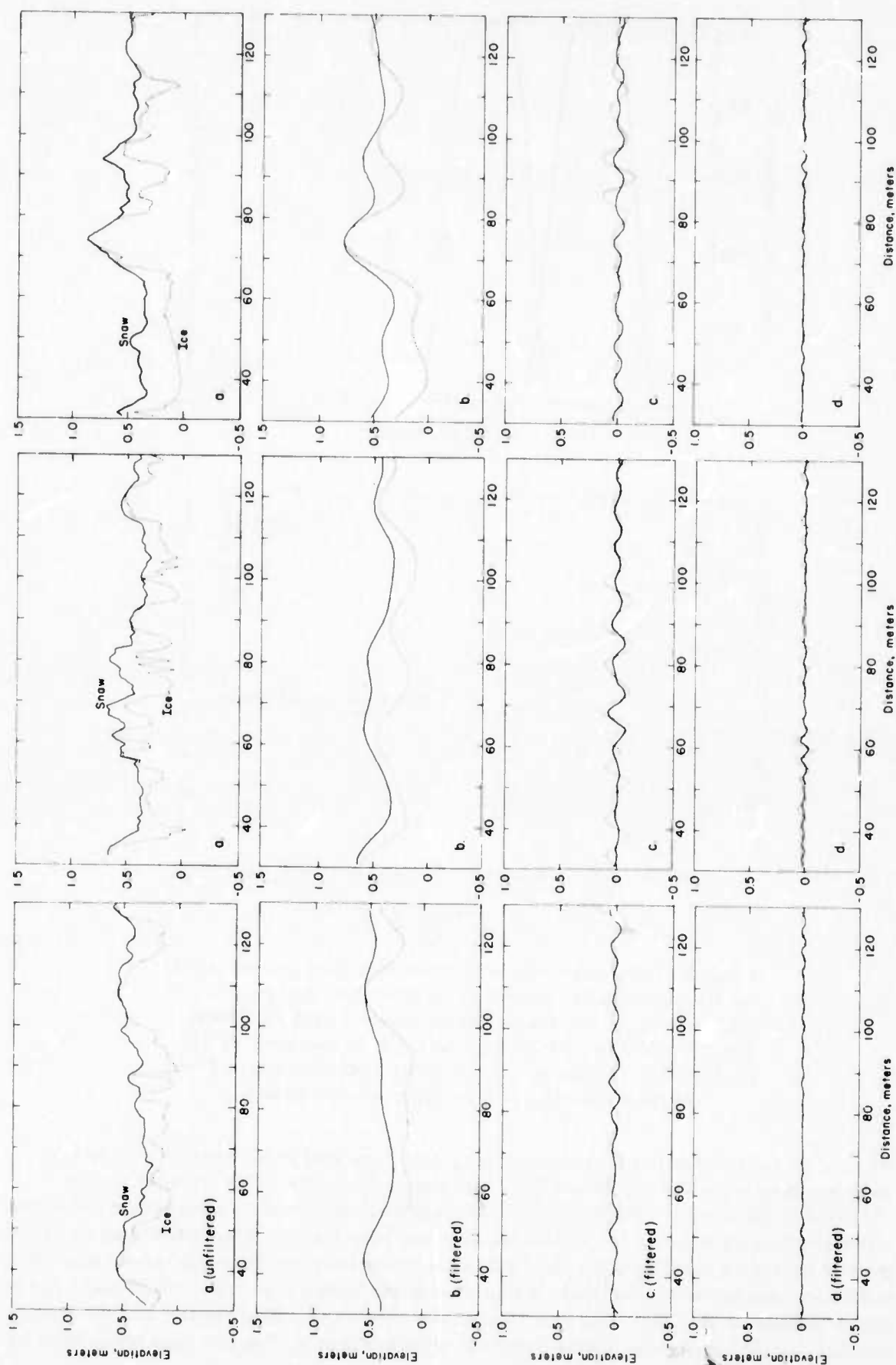
Figure 5. Unfiltered and filtered snow and ice profile data. The frequency response of the band pass filters used is given in Figure 4. For each profile, part a represents the unfiltered profiles and parts b, c and d represent the low, medium and high pass filtered results respectively.

the correlation coefficient (using 16 degrees of freedom) is given by the dotted line. The plot clearly indicates the stronger correlation for wavelengths longer than 8 m. In fact the average correlation coefficient for the lowest frequency band is 0.80, which is greater than the average total correlation coefficient (for all frequencies) of 0.72.

The filtered profiles for each of the three pass bands together with the unfiltered results are given in Figure 5. These plots qualitatively give the same results indicated by the correlation coefficients, namely that wavelengths longer than about 8 m are well correlated whereas shorter wavelengths have a poorer correlation. In summary the quantitative results suggest that as a rule of thumb 8 m is the demarcation wavelength, with shorter wavelength variation in the ice surface being masked by the snow cover while the longer wavelength components are not strongly affected.

Both before and after these measurements were made, high winds blew away much of the snow cover. Consequently, the resulting surface roughness spectrum changed to one more nearly approaching the true ice surface. The spectra plotted in this paper give some indication of the limits of the surface roughness spectrum expected due to such changing conditions.

The spectra of the true ice surface also indicated a dominant low frequency spectral peak at a wavelength of about 30 m which persisted on parallel profiles. We feel this peak is representative of melt hummock spacings for the region analyzed. The low frequency peak did shift as the profile direction was changed, indicating lineation (Hibler and LeSchack 1972) in the surface approximately parallel to the nearby pressure ridge shown in Figure 1. It should be noted here that the profiles analyzed do not include the pressure ridge, so that we are discussing here only the "flat" part of a multiyear floe.

Freeboard/ice thickness correlations

To study the correlation between surface roughness and thickness and the bottom topography we calculated a correlation coefficient of 0.60 for the correlation of freeboard to draft and a co-efficient of 0.79 for the correlation of freeboard to thickness. Both these numbers indicate a linear correlation significant at better than the 1% level by an analysis of variance test.

To determine the ice draft and/or the ice thickness from the freeboard, we can calculate the regression line between these variables. The resulting equations are $d = 1.337f + 2.80$ and $t = 2.32f + 2.80$ where d and t are the ice draft and the thickness respectively and f is the freeboard (all in meters). Using these relations, the root mean square errors between the predicted and observed values of draft and thickness were in both cases 0.36 m. These numbers indicate the improvement that can be made in draft or thickness estimates by having information of the local freeboard available. (The standard error of the estimate of 0.36 m obtained by using the regression line is significantly less than the standard errors of the estimate on draft (0.46 m) and thickness (0.60 m), see Table 1).

Table I. Summary of statistical results (31 holes).

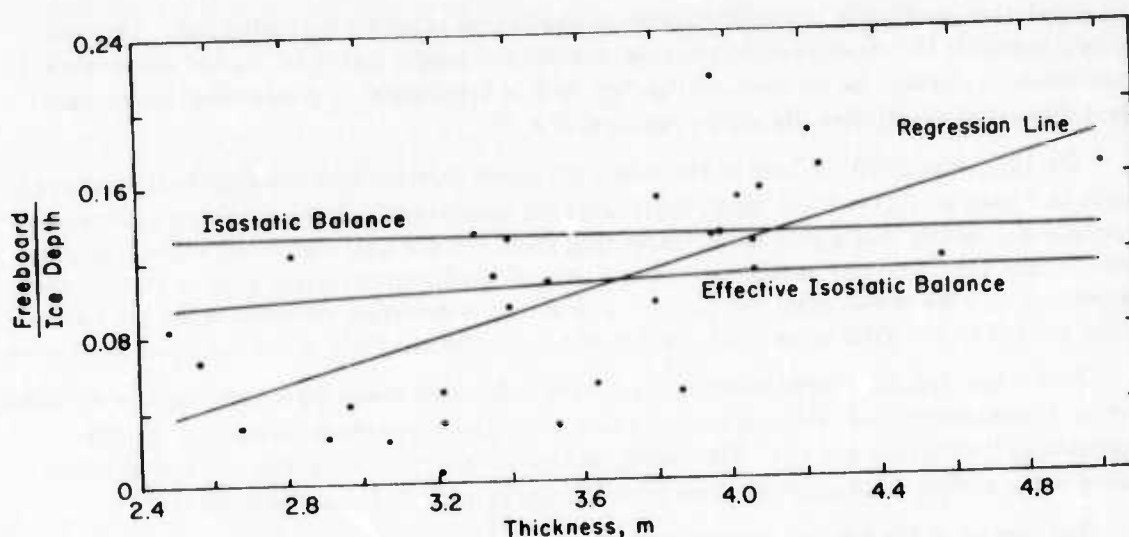|	
Mean ice draft	3.24 m
Ice draft standard deviation	0.46 m
Mean ice thickness	3.57 m
Thickness standard deviation	0.60 m
Mean freeboard	0.33 m
Freeboard standard deviation	0.20 m
Mean snow depth	0.16 m
Snow depth standard deviation	0.13 m
Correlation coefficients	
Depth to freeboard	0.60 m
Thickness to freeboard	0.79 m

Figure 6. *Ice freeboard/ice depth ratio (f/d) versus ice thickness (t). The isostatic balance line was calculated assuming ice and sea water densities of 0.91 and 1.03 g cm^{-3}. In the effective isostatic balance the weight of the snow was also included.*

Both linear regression lines deviate significantly from the result expected if the ice is in isostatic balance. In particular the isostatic balance result would be of the form $t = ad$ where $a =$ (density of sea water)/(density of ice). Assuming a sea ice density of 0.91 g cm^{-3} (estimated from the ice cores) and a sea water density of 1.03 g cm^{-3}, we would obtain ratios for d/f and t/f of 7.58 and 8.58 respectively.

The trend of the deviations from isostatic balance is indicated very clearly in Figure 6 where we have plotted the freeboard/draft ratio vs thickness. The isostatic balance line with the snow cover neglected and an effective isostatic balance line considering both the density of the ice and the depression of the ice sheet by the snow cover are indicated. In calculating the effective line a mean snow thickness of 0.16 m and a snow density of 0.45 g cm^{-3} were used, based on snow measurements at the site. Also shown is the regression line of f/d on t. The trend is clearly for the ice draft to be greater than expected from isostatic balance for thin ice and the inverse for thick ice. Therefore, on a point to point basis, the assumption of isostatic balance breaks down.

However, as might be expected since the ice sheet is clearly free-floating, if cross-sectional areas rather than individual points are used for comparison with the assumption of isostatic balance, the results are quite good. To illustrate this we note that the mean thickness and mean draft are proportional to the total cross-sectional area and cross-sectional area below the water level respectively of the ice floe. If a depression of 0.07 m due to 0.16 m of snow cover is included we find that the average draft of 3.24 m and the average ice thickness of 3.57 m imply a mean ice density of 0.915 g cm^{-3} for isostatic balance. This is in agreement with the findings of Kovacs et al. (1972) and is a very reasonable value since cores taken in this region of the floe indicated densities between 0.90 and 0.92 g cm^{-3}. The mean thickness we obtained also compares well with the mean value for Beaufort Sea "unhummocked" multiyear ice (3.47 m) obtained by Koerner (1971).

The fact that individual points deviate significantly from isostatic balance while on the average the overall ice sheet is in isostatic balance is similar to the situation observed in pressure ridges (Fukutomi and Kusunoki 1951, Weeks et al. 1972). The form of the deviations suggests that a model similar to the Wittmann-Makaroff pressure ridge model (Wittmann and Schule 1966) may well also apply to the small melt hummocks that develop on a multiyear floe. In this model the underside of
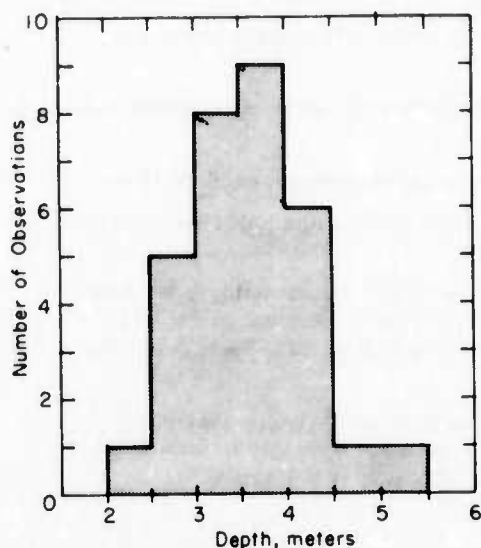
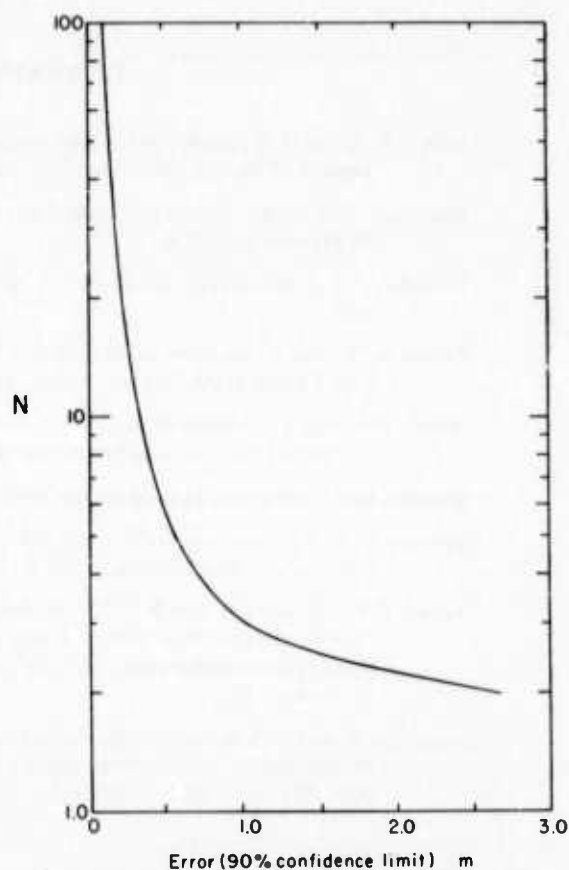Figure 7. *Distribution of ice thickness measurements.*

Figure 8. *Estimated error (90% confidence limits) of the mean ice thickness as a function of the number of holes used in making the estimate.*

the hummock has a greater horizontal extent than the sail. This would yield deviations of the type observed, i.e. deep hummocks are less deep than would be expected on the basis of isostasy. The actual balance would be between the volume of the hummock below water and the volume above water.

Estimating the average ice thickness

One interesting application of the thickness data is to estimate, using sampling theory, the number of holes needed to obtain the mean ice thickness of the multiyear floe with a specified accuracy. Based on the 31 measurements, the mean and standard deviation of the ice thickness is 3.57 ± 0.60 m. The frequency distribution of the ice thicknesses is shown in Figure 7 and is to a good approximation normal. The 90% confidence limits on the true mean are 3.39 and 3.75 m. If we now assume (Griffiths 1967) that the value of the standard deviation is independent of the sample size N, a t distribution may be used to estimate the number of holes required to estimate the ice thickness to a given accuracy. Figure 8 shows the 90% confidence limits on the mean calculated using this procedure plotted against N. To obtain the mean thickness of the unridged portion of the multiyear floe accurate to better than 0.5 m, with a 90% certainty, only six holes are necessary. On the other hand, for an accuracy of 0.1 m with the same certainty, 100 holes would be required.

LITERATURE CITED

Banke, E.G. and S.D. Smith (1971) Wind stress over ice and over water in the Beaufort Sea. *Journal of Geophysical Research*, vol. 76, no. 30, p. 7368-7374.

Blackman, R.B. and J.W. Tukey (1958) *The measurement of power spectra*. New York: Dover Publications, 190 p.

Griffiths, J.C. (1967) *Scientific method in analysis of sediments*. New York: McGraw, p. 303-310.

Fukutomi, T. and K. Kusunoki (1951) On the form and formation of hummocky ice ranges. *Low Temperature Science*, vol. 8, p. 59-88.

Hibler, W.D. and L. LeSchack (1972) Power spectrum analysis of under-sea and surface sea ice ridge profiles. *Journal of Glaciology*.

Koerner, R.M. (1971) Ice balance in the Arctic Ocean. *AIDJEX Bulletin*, no. 6, p. 11-26.

Kovacs, A., W.F. Weeks, S. Ackley and W.D. Hibler (1972) A study of a multiyear pressure ridge in the Beaufort Sea. Part II (this report).

Weeks, W.F., A. Kovacs and W.D. Hibler (1972) Pressure ridge characteristics in the Arctic coastal environment. *Proceedings, First International Conference on Port and Ocean Engineering under Arctic Conditions*, 23-30 August 1971, Tech. University of Norway, 32 p.

Wittmann, W. and J.J. Schule (1966) Comments on the mass budget of Arctic pack ice. *Proceedings, Symposium on the Arctic Heat Budget and Atmospheric Circulation*, (J.O. Fletcher, ed.), p. 217-246. The Rand Corporation (RM-5233-NSF).

PART IV: AIRPHOTO ANALYSIS OF ICE DEFORMATION IN THE BEAUFORT SEA

by

Allan D. Hartwell

ABSTRACT

Ice deformation in a 175-km^2 area of the Beaufort Sea (at about 74°N, 131°W) between 11 and 23 March 1971 was analyzed by means of sequential aerial photographs. The approximate time, direction and magnitude of deformational motion were determined by combining observations of the changes in features related to ice deformation, such as leads, fractures and pressure ridges, and mesoscale measurements of strains and strain rates on the ice. During this period a series of compressions, extensions and shearing motions occurred, producing numerous changes in ice morphology. The entire area was apparently under considerable lateral constraint with no observable rotation or rounding of floes. No leads wider than about 150 m were present. Shearing motion along one individual lead of up to 280 m was documented by the photographs. Relative motion along shear zones was nearly always dextral or right lateral in accord with the clockwise rotation of the Pacific Gyre.

INTRODUCTION

The Arctic Basin is dominated by a formidable cover of sea ice that is in constant drifting motion. The morphology of the ice is constantly changing: convergence and ridging occur in one area while divergence with associated fracturing and floe separation occur in another (Kovacs 1971). In order to better understand the large-scale response of sea ice to its environment, a study of the mesoscale deformation of the pack ice in the Beaufort Sea was conducted during March 1971 as part of the 1971 Arctic Ice Dynamics Joint Experiment (AIDJEX) pilot program. This study consisted of measurement of strains and strain rates between surface stations in a triangular network during a two-week period from 11 to 23 March (Hibler et al. 1972). In addition sequential aerial photographs of the ice cover were taken during this period by NASA and U.S. Navy planes at altitudes ranging from 533 to 10,363 m. This photography permitted observations of the nature of local ice deformation.

This report presents the results of an analysis of some of the air photos obtained. This study is specifically related to sea ice deformation in a 175-km^2 area centered on the strain triangle. From each set of photographs, overlays were prepared of features related to deformation such as leads, fractures and pressure ridges. The overlays were then photographically reduced to a common scale so that the changes in specific features could be traced through the two-week period. When used in conjunction with visual ground observations and strain measurements on the ice, the approximate time, direction and magnitude of events associated with the deformation of the sea ice could be determined.
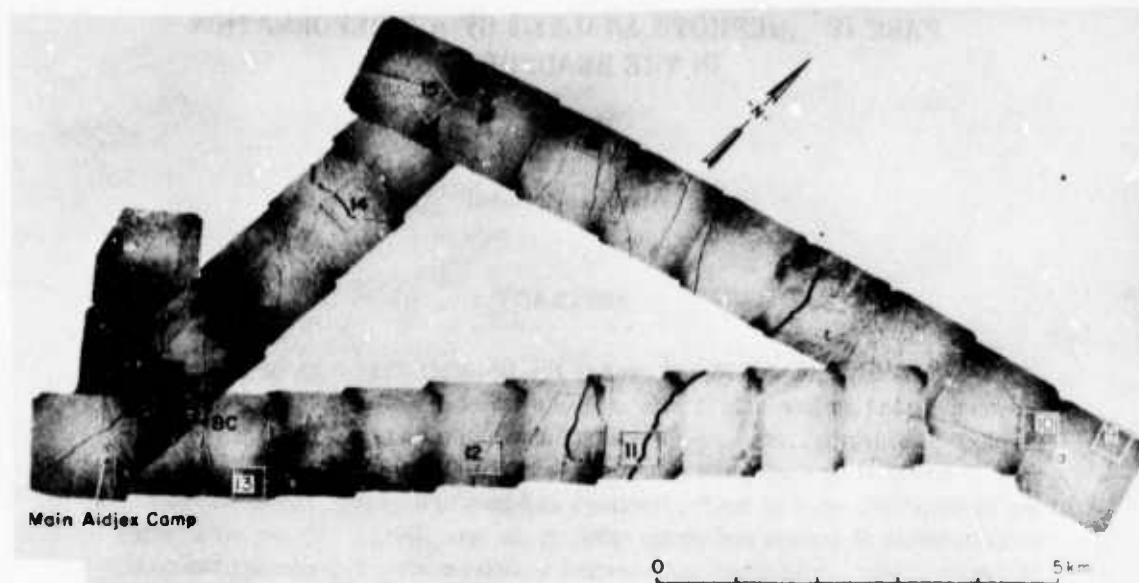
Figure 1. Location map showing strain triangle and ice conditions on 11 March; boxed areas are locations of Figures 9-16.

STUDY AREA

The field site for this study was near the Canadian Polar Continental Shelf Project's Camp 200 in the Beaufort Sea about 560 km north of Tuktoyaktuk, N.W.T., Canada (Fig. 1; see also Figure 1 of Part I). The camp was on the edge of a large multiyear floe roughly 16 km across, located at $72°45'N$, $130°15'W$. The floe was surrounded by first-year pack ice about 2 m thick. This ice contained a considerable number of pressure ridges and fractures as well as some thinner zones of old refrozen leads. During the two weeks of the study the ice cover underwent considerable deformation.

METHOD OF ANALYSIS

This study is based on aerial photographs obtained during overflights by a NASA Convair 990 and a U.S. Navy (NAVOCEANO) NC-121K on 11, 15, 21 and 23 March 1971 (Table I). From mosaics of these photographs overlays of 1) leads and fractures and 2) pressure ridges were prepared at a common scale for each of the four days.

From these overlays changes in specific features were traced through the two-week period in order to estimate the direction and magnitude of specific deformational events. For example, extension or compression along leads and fractures was determined by graphically restoring the ice cover to its unfractured condition and measuring the approximate magnitude and direction of net movement from the aerial photographs. Like wise, shear-type motions could be easily recognized and measured from observed offsets of pack ice features such as old ridges. Numerous new pressure ridges formed during the period of observation and in some instances the amount of deformed ice they contained could be estimated.

Reference is made here to measurements of pack ice strain between the triangular network of Stations a, β and BC (base camp) established by Hibler et al. (1972) using distance-measuring

Table I. Photo coverage, 1971 AIDJEX pilot program.

Date	Local time*	Approximate altitude, m	No. of runs	Area covered	Weather conditions/ image quality
11 March (NASA)	1606-1625	1,067	5	Legs of strain triangle and strip extending SE from main camp	Excellent
15 March (NASA)	1312-1514	10,360	10	Regional coverage N and E of main camp cut to about 35 km	Fair
	1525-1535	3,048	2	Regional coverage NE of main camp including two strain stations	Fair
	1538-1553	1,067	3	Legs near but not coincident with strain triangle	Good
21 March (NAVOCEANO)	1428-1550	533	12	Strain triangle area	Poor
23 March (NAVOCEANO)	1355-1417	529	3	Legs of strain triangle	Excellent
	1448-1650	1,524	10	Regional coverage	Good

*Local time is 7 hours behind Greenwich Mean Time.

instruments (Fig. 1). Their data (Fig. 3) provided a measurement of the net deformation (i.e. strain rate tensor) for the region while the overlays were used to catalog and identify specific local deformational events and history. The initial lengths of the triangle legs as measured on 12 March were: $\alpha - \beta = 8.3$ km, $\alpha - BC = 10.7$ km, and $\beta - BC = 5.6$ km.

ICE DEFORMATIONS

11 March

The initial ice conditions in the study area are shown in the 11 March photographs (Fig. 1) and in the corresponding overlay showing the lead and fracture system at that time (Fig. 2). There are a large number of existing ridges. There are also two large leads (26-35 m wide) and numerous smaller ones (4-17 m wide). Other discernible features are the large refrozen lead of thinner ice near Station α and the multiyear floe near BC. Two recent deformational events are clearly shown in this photography. The first of these is an older localized NW-SE shear of 23 to 29 m along three fractures midway between α and BC. This shearing produced some minor ridges and at the time of the photography the fractures had refrozen with a thin cover of ice (see Fig. 11a). The second event is a major NE-SW extension of up to 35 m that opened almost all of the fractures in the area and was continuing at the time of the photography (about 1620). Strain measurements made between 1200 and 1820 on this same day showed continuing extension of up to 98 m along the $\alpha-\beta$ line and 31 m along $\alpha-BC$ (Fig. 3). By late in the day ground observers noted that a large number of leads had opened in the study area and a large fracture had split the multiyear floe on which the camp was located, opening a 30-m lead along a pressure ridge roughly 200 m from their living quarters (Hibler et al. 1972).
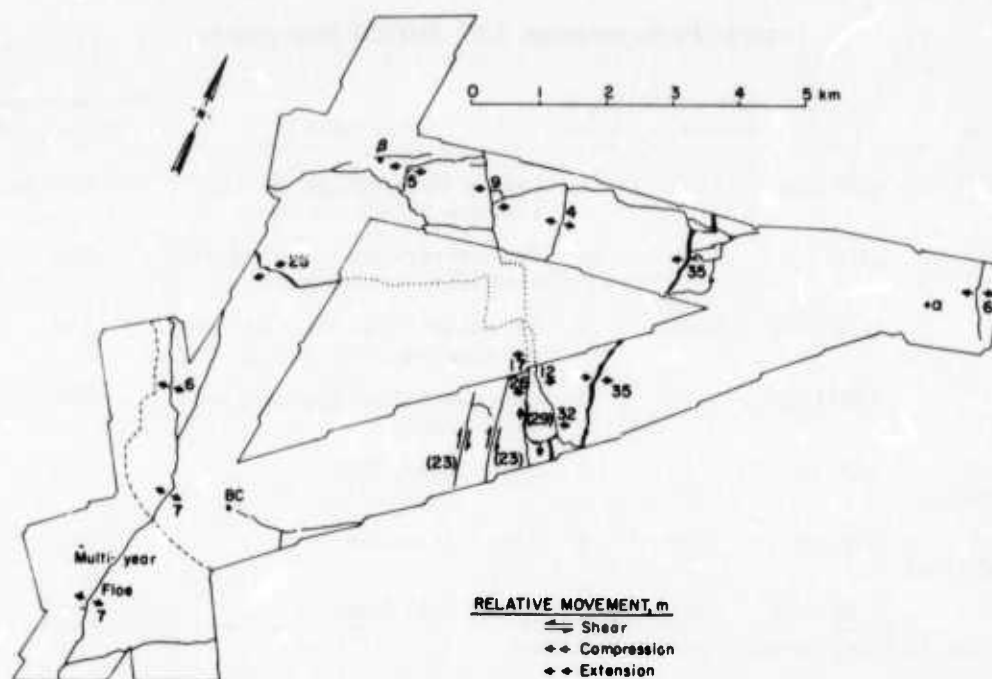
Figure 2. Lead and fracture system on 11 March. Arrows indicate type and direction
of relative movement; approximate magnitude is given in meters. Earlier movement
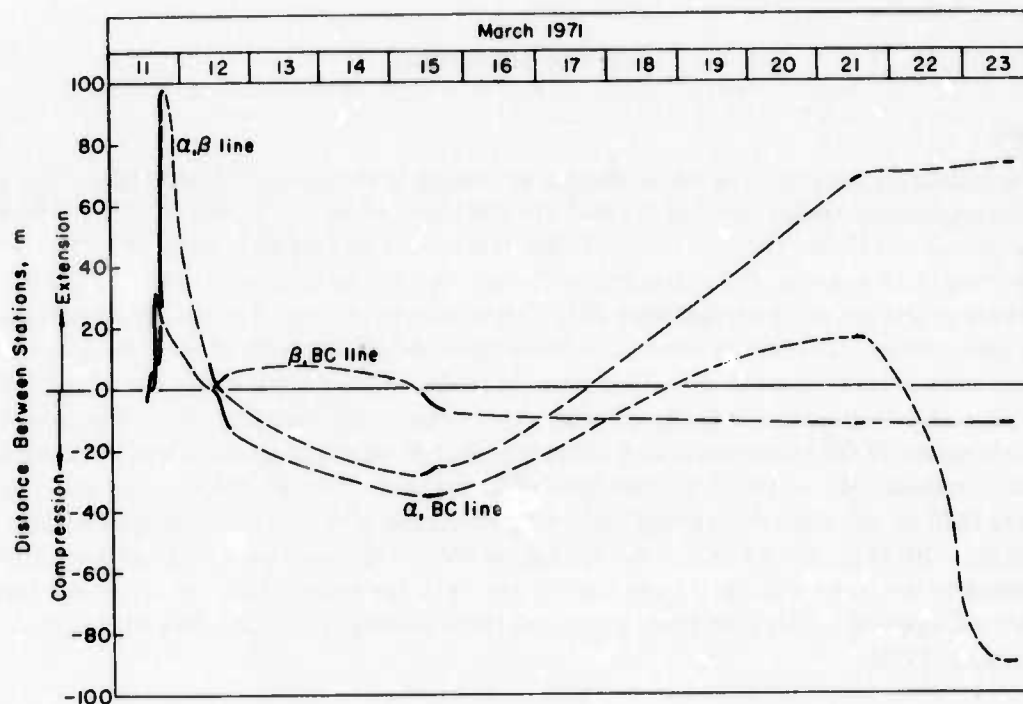indicated by parentheses.

Figure 3. Measured extension and compression along the triangular network, 11 to 23 March.
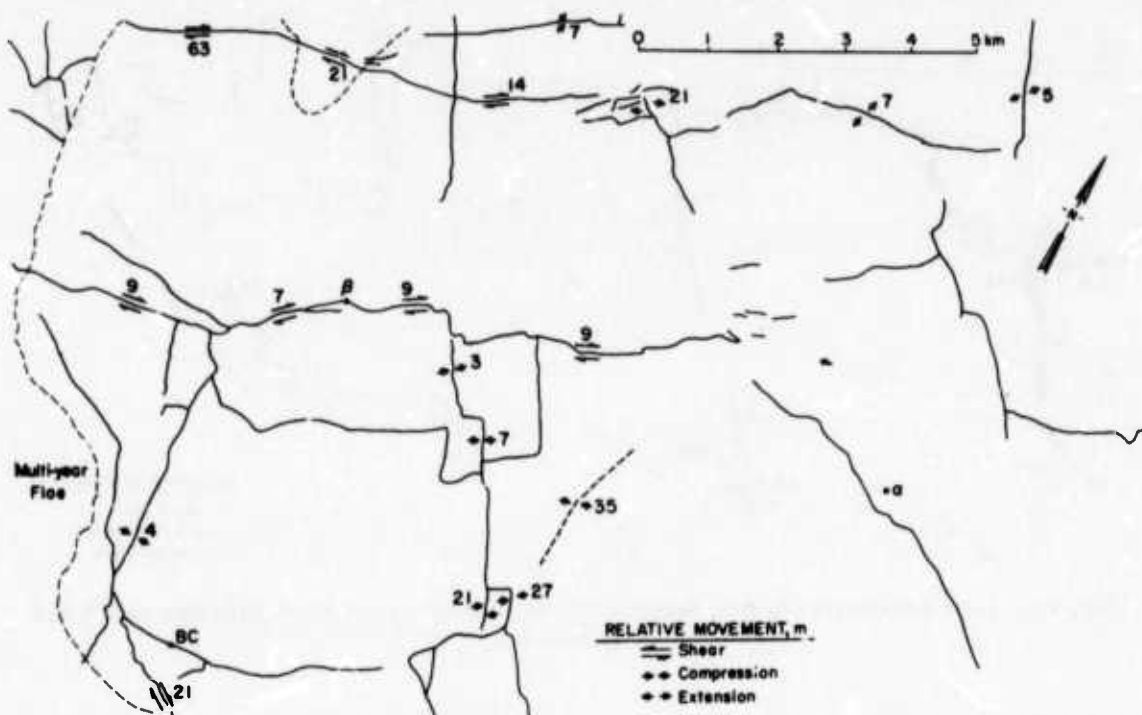
Figure 4. Lead and fracture system between 12 and 15 March; note NE-SW shear zones.

12 March

Sometime during the night the movement "reversed" and compression occurred across the entire strain network (Fig. 3). By morning most of the leads had closed and some new pressure ridges formed. A large number of cracks and leads were present in the vicinity of β but the station was still intact (Hibler et al. 1972). By 1100 the $a-\beta$ and $a-$BC lines had shortened to their original lengths and readings were finally obtained along $\beta-$BC, thereby "closing" the strain network. During the afternoon $a-\beta$ and $a-$BC showed 13 m and 1 m compression respectively whereas $\beta-$BC had 5 m extension (Fig. 3).

13-14 March

Although. no photography or strain measurements were obtained during this period, it was apparent from the strain measurements, ground observations and photography of 15 March that additional compression of up to about 35 m occurred along the $a-\beta$ and $a-$BC lines (Fig. 3). This NE-SW compression closed all of the major fractures in the study area, producing some ridging and localized shearing. In addition two new E-W dextral or right lateral* shear zones developed, one across Station β (7-9 m shear) and the other parallel but 3.5 km north of Station β (up to 63 m shear; Fig. 4). This shearing motion was a small-scale replicate of a much larger regional scale deformation that was occurring across a series of nearly parallel shear zones, suggesting that the ice cover was deforming as several very large floes (Hibler et al. 1972).

15 March

No significant deformation was observed on this day. Along $\beta-$BC several meters of compression occurred, whereas the other two began to show a few meters of extension (see Fig. 3).

---

*Movement of right side down or to the right relative to the left side.
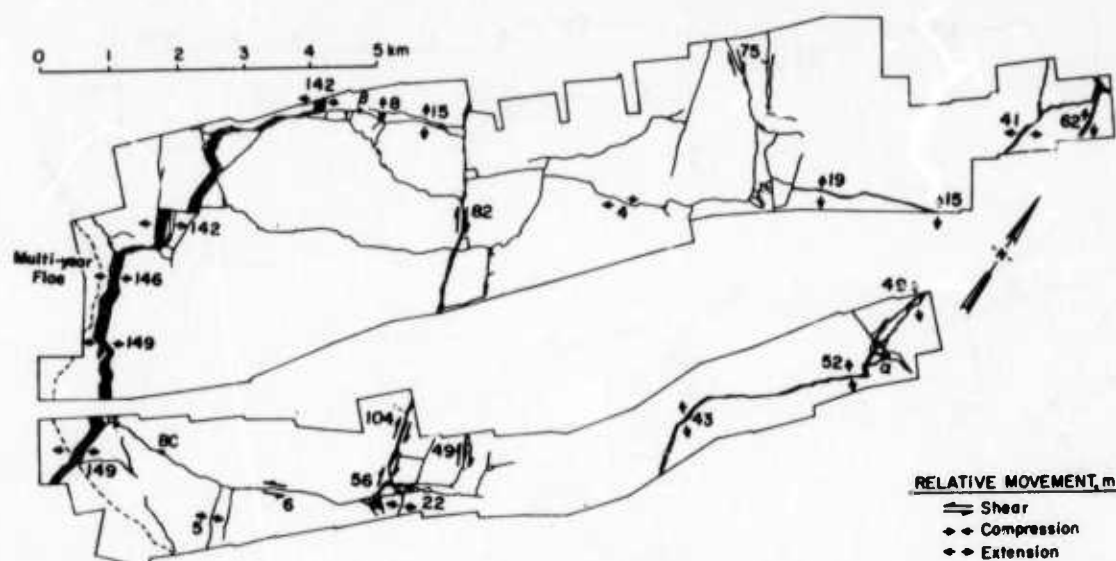
Figure 5. Lead and fracture system between 16 and 20 March; note large extension to left and shear in center.

16-20 March

Although no photography or strain measurements were obtained during this period, examination of the 15 and 21 March photographs and the strain data of 21 March indicate that extensive deformation occurred across the entire study area (Fig. 5). Active E-W dilatation apparently continued, opening two long leads, one west of β-BC about 142-149 m and the other near α about 41-62 m, and numerous smaller ones (4-22 m). A major dextral NW-SE shear zone with 56-104 m movement developed across the center of the strain network. This movement apparently also caused an 8-19 m dilatation along the old shear zone running through β. In addition a lead formed along the pressure ridge at α, destroying the tent which marked the station.

21 March

By the time of the photography up to 22 m of NE-SW dilatation had occurred along three newly refrozen leads (Fig. 6). Along α-BC and α-β several meters of continuing dilatation was measured, whereas β-BC showed no change (Fig. 3).

22 March

No photography or strain measurements were obtained on this day, but from the photographs and strain measurements of 21 and 23 March it is apparent that extensive deformation occurred (Fig. 7). Major NW-SE dilatation of up to 216 m with some shearing and new ridging occurred in the center of the study area and east of α (50-168 m). The long lead west of β-BC had 74-89 m of E-W compression but did not close completely.

23 March

During the night a general N-S compression occurred, causing offset of 47-108 m in the refrozen lead west of the strain triangle, 69 m in the center of the study area, and 36 m east of α (Fig. 8). The strain measurements show that very little deformation occurred during the day (Fig. 3).
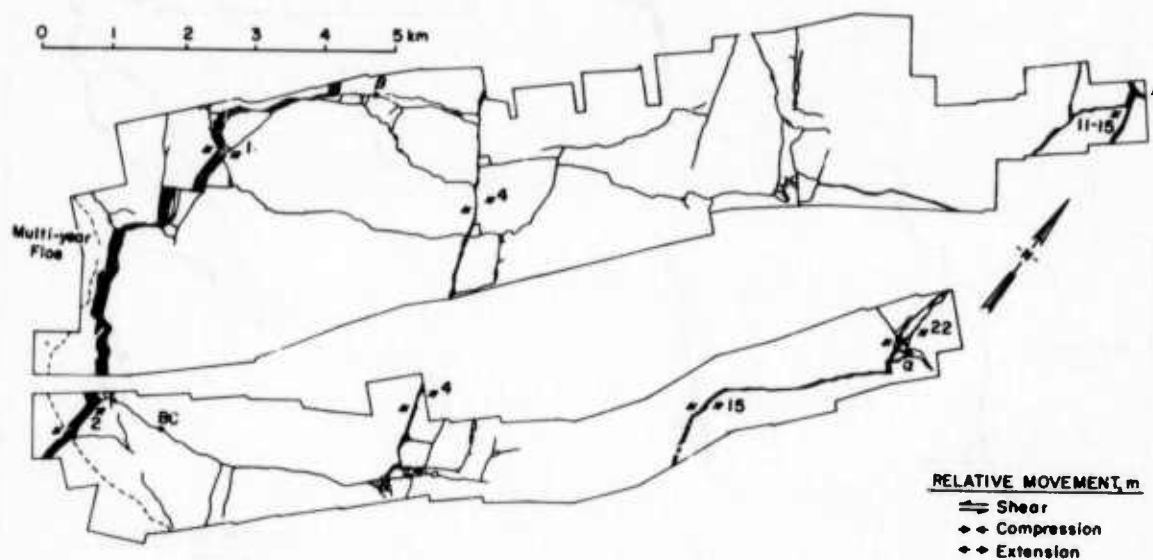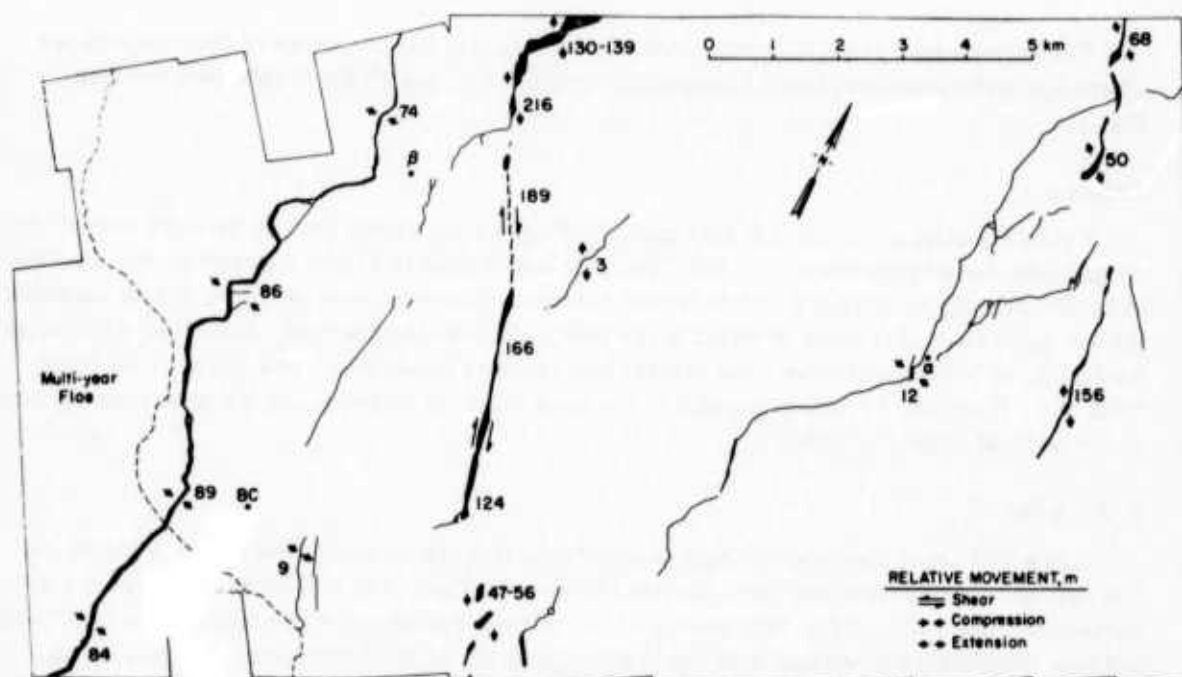
Figure 6. Lead and fracture system on 21 March.

Figure 7. Lead and fracture system on 22 March; note continued shearing in center of strain triangle.
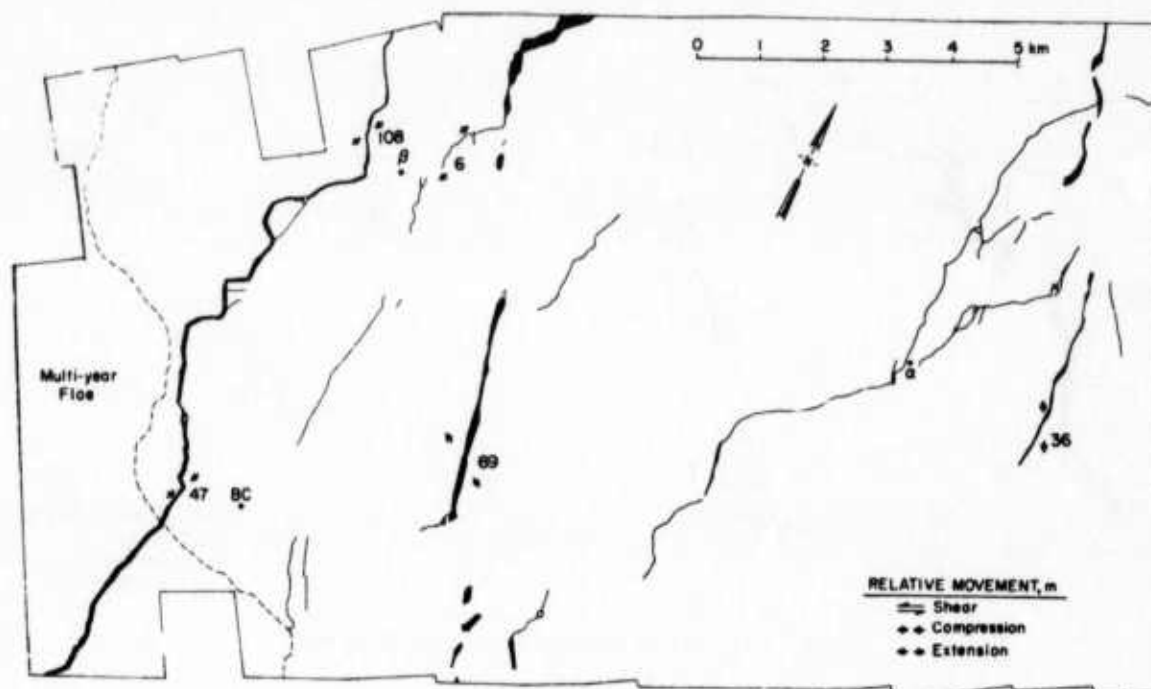
*Figure 8. Lead and fracture system on 23 March.*

NET DEFORMATIONAL CHANGES

The deformations which occurred in this study area over the two weeks of observations are photographically documented using comparative photos of 11 and 23 March (see location map, Fig. 1).

Station *a*

Extensive changes occurred in this area. In Figure 9 the narrow lead on the right was slightly compressed, before refreezing (Fig. 9b). The new lead visible in Figure 9 formed on the 22nd due to NE-SW dilatation. Note how it cuts across numerous pressure ridges where the ice is somewhat thicker and causes only minor cracking in the relatively thin refrozen lead. At Station *a* extensive fracturing, 30 m of lateral offset, and several new pressure ridges developed during 16-20 March (Fig. 10). Fracturing developed parallel to the main ridge and helped produce a new ridge adjacent to the original ridge (Fig. 10b).

a – BC Line

Along this leg of the strain triangle leads closed from the east and west on 13-14 March, re-freezing and causing numerous small pressure ridges. In Figure 11b a 20-m-wide strip of ice was compressed into a new ridge. Note how solid the original fracture zone has become due to refreezing and how completely the original lead has healed due to the parallel directions of extension and compression. Figure 12 clearly shows the large lead which developed on 16-20 March and further sheared on 22 March, resulting in about 250 m of net dextral offset in a NW-SE direction. Note the continuing NW-SE offset that was occurring in the refrozen ice across the lead at the time the photo was taken (about 69 m; Fig. 12b).
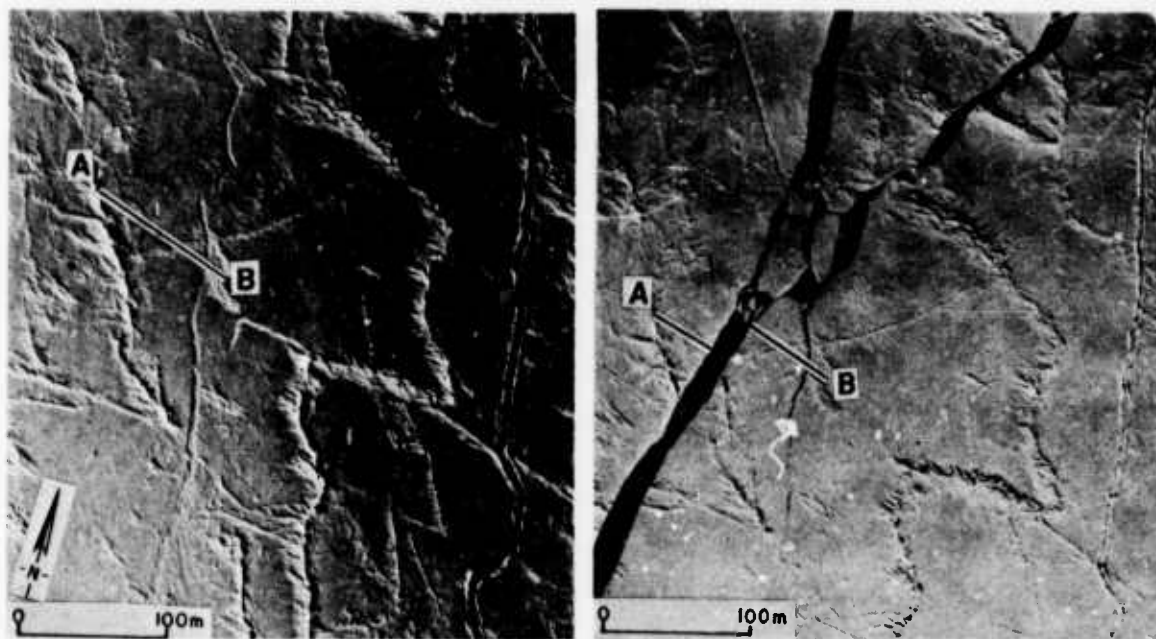
a. 11 March.   b. 23 March.
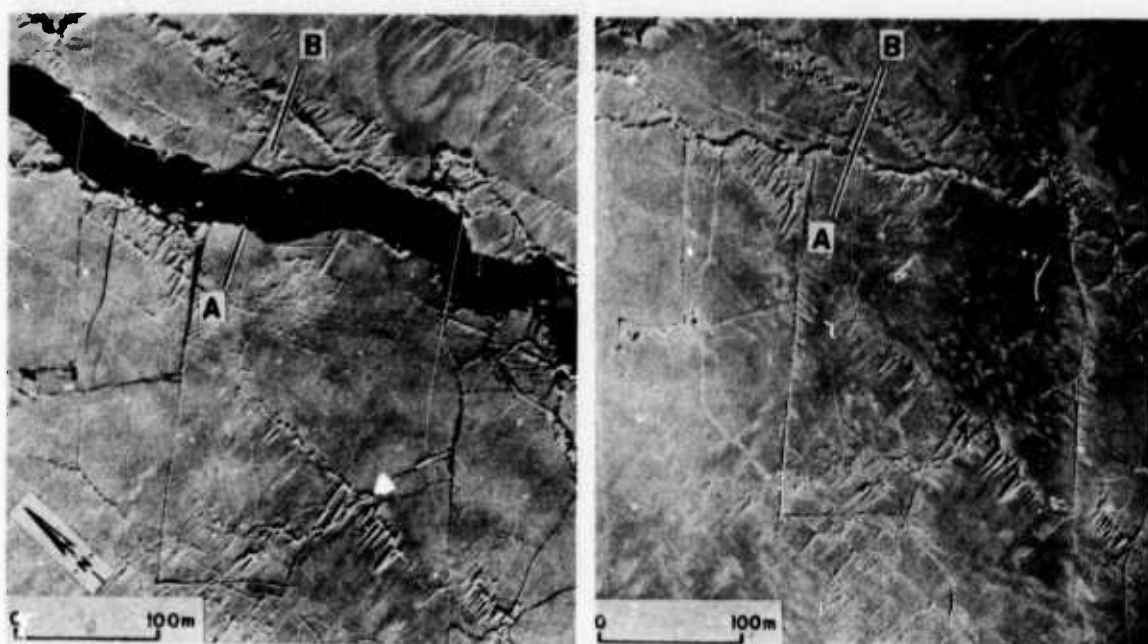
Figure 9. Fracturing near Station a.
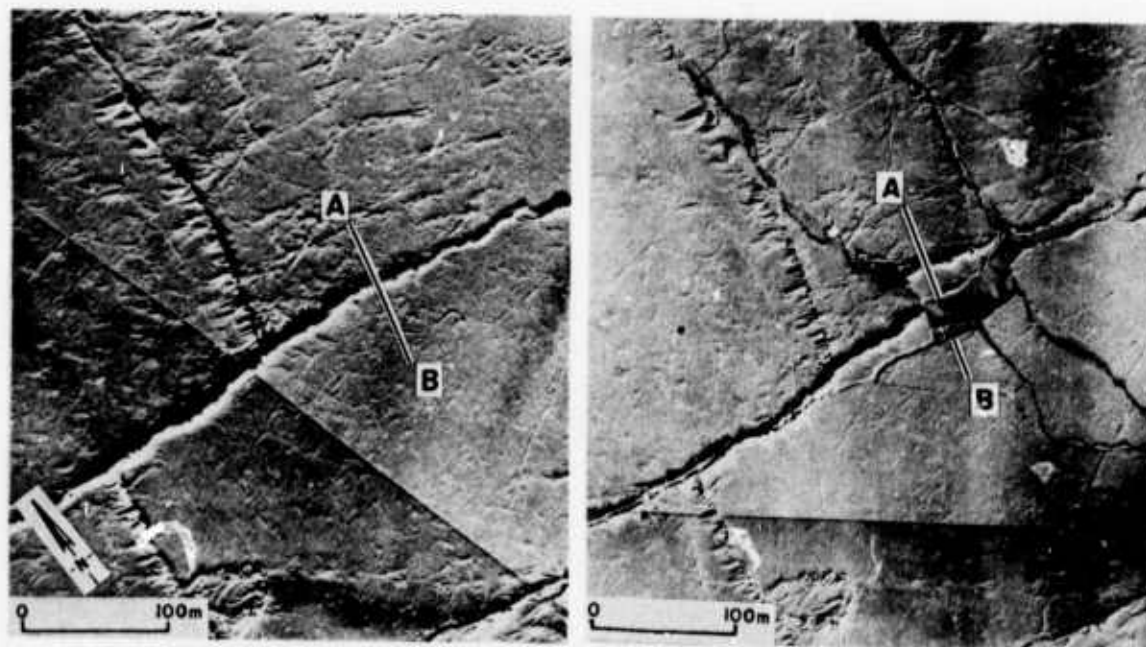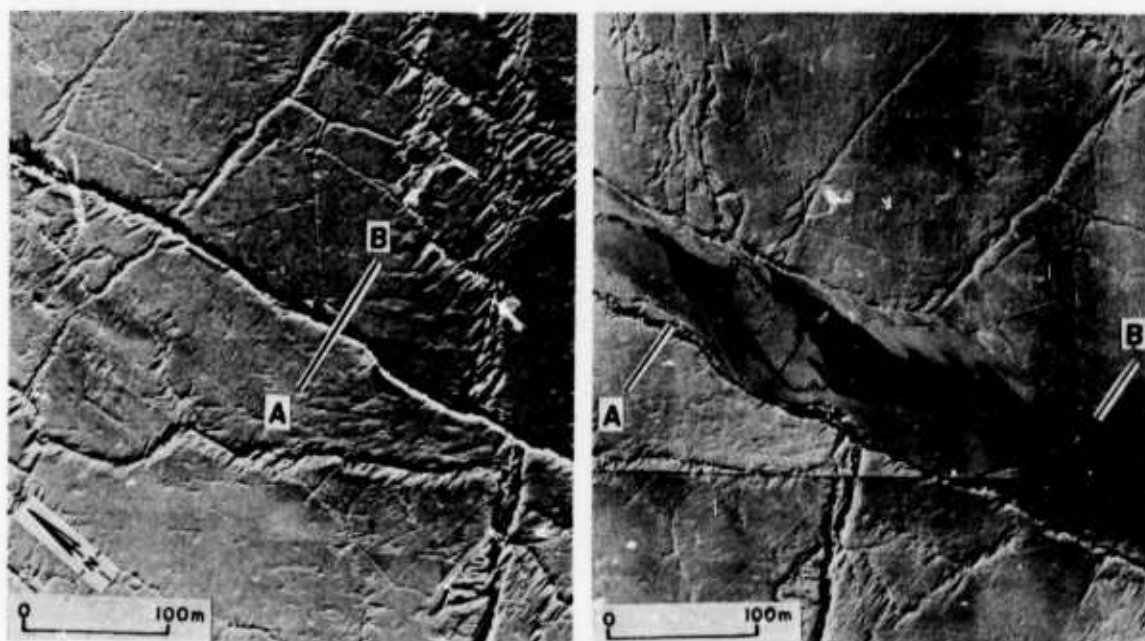

a. 11 March.   b. 23 March.

Figure 10. Fracturing and deformation at Station a.
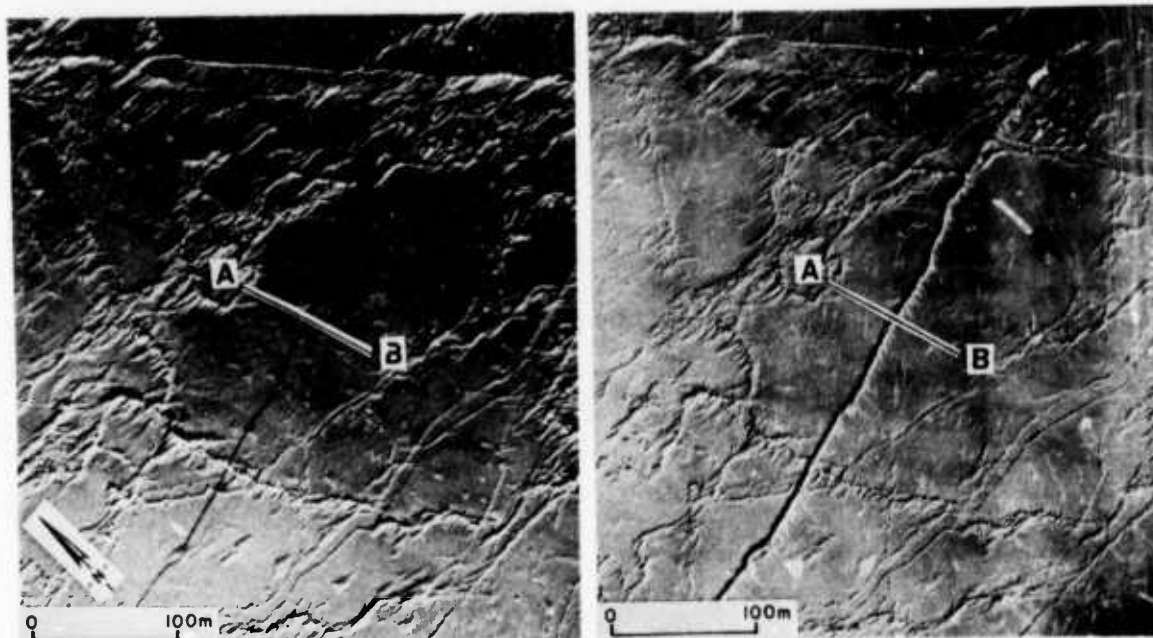
a. 11 March.   b. 23 March.

Figure 11. Lead along the a – BC leg which deformed about 20 m of ice as it closed.

a. 11 March.   b. 23 March.

Figure 12. Large lead along a – BC leg which produced about 250 m of offset.

a. 11 March.   b. 23 March.

Figure 13. Ridge that formed near Station BC.

Station BC

There was relatively little deformation in this area. Figure 13 shows the only major change, a fracture which sheared about 6 m NE-SW during 16-20 March, creating a long, prominent ridge. Note its straightness and remarkably uniform vertical profile as shown by shadows (Fig. 13b). This new ridge looks very similar to the much older ones which surround it. The uplifted blocks such as the one in the upper right also show the thickness of the ice (about 2 m).


β - BC Line

This leg of the strain triangle showed only a small amount of deformation during the study (Fig. 3). The only significant change was the closing of the lead visible on 11 March and the formation of a small ridge (Fig. 14b). This closure was somewhat unusual in that the lead apparently refroze and then fractured again along the southern edge, forming a small, irregular ridge during the subsequent compression.

Station β

A number of changes occurred in this area. The lead present on 11 March (Fig. 15a) closed and refroze, forming a new ridge (Fig. 15b). The fracture visible on 11 March also formed a new ridge during the same compressional event (13-14 March); later, on 16-20 March, it refractured and the 60-m-wide lead formed (Fig. 15b). Note the NE-SW compression with attendant finger rafting in the refrozen lead at the time of photography.
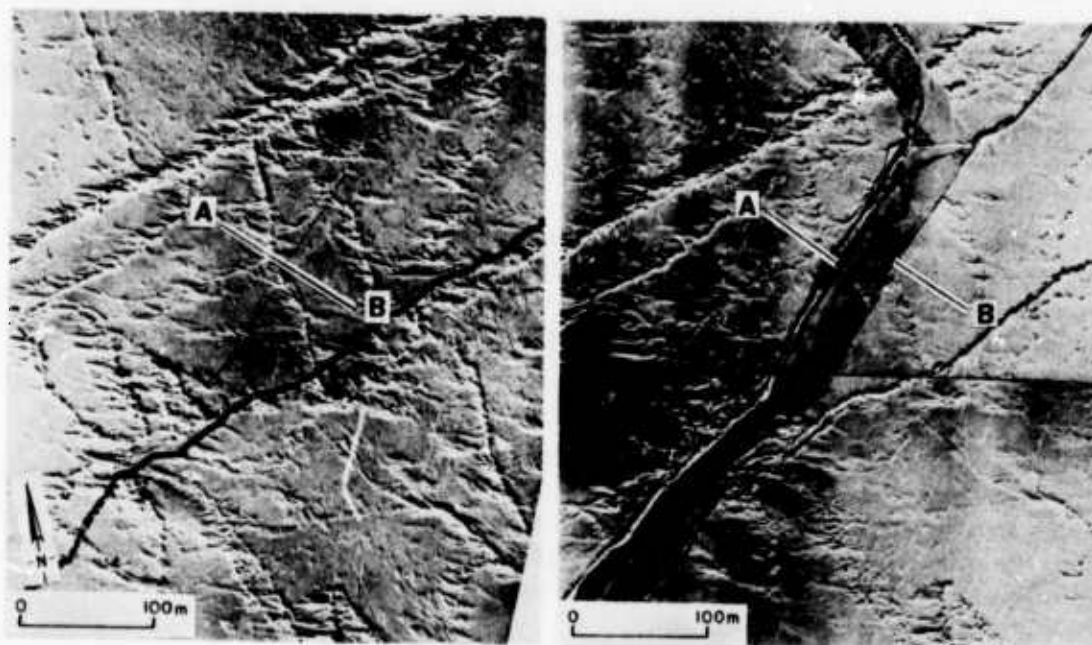

$a - \beta$ Line

Along this leg of the strain network extensive dextral shear occurred, forming the largest new ridge observed anywhere in the study area (Fig. 16b). The shear motion, like that in Figure 12,
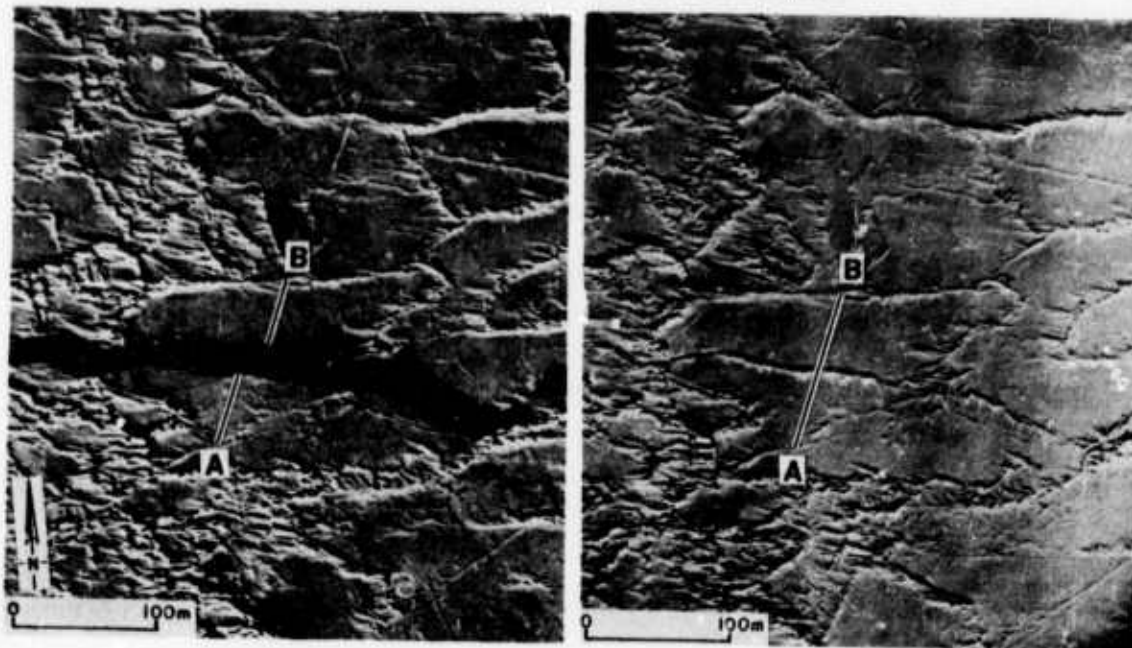
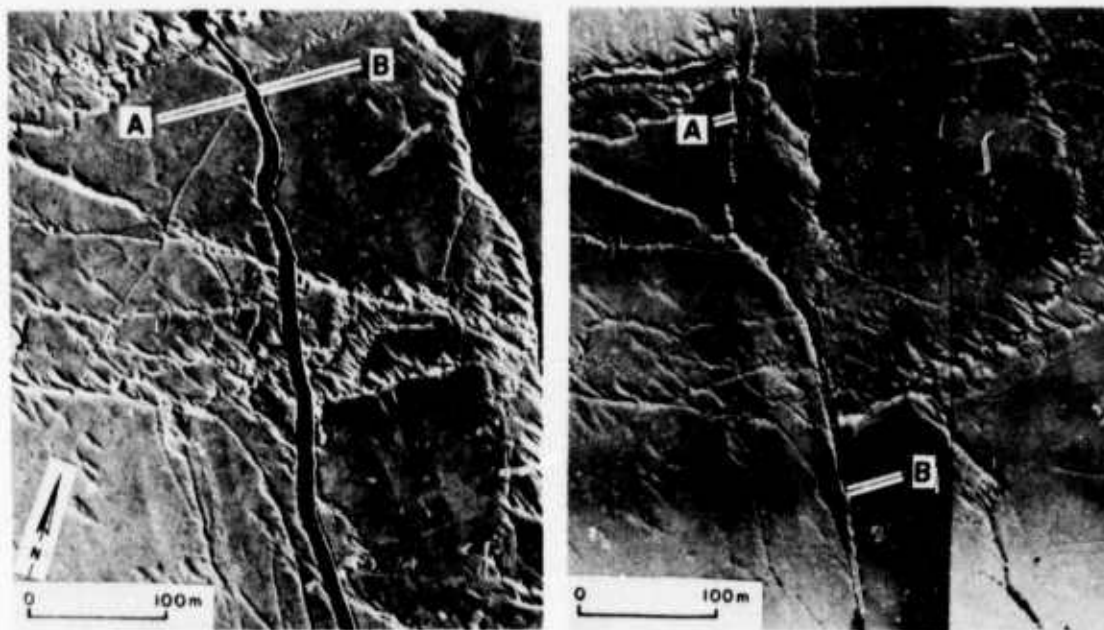a. 11 March.   b. 23 March.

Figure 14. Lead along the β–BC leg that closed and formed a new ridge.

a. 11 March.   b. 23 March.

Figure 15. Deformation at Station β.

a. 11 March.   b. 23 March.

Figure 16. Large dextral shear and new ridge that formed along the α–β leg.

started on 16-20 March and further sheared on 22 March, resulting in a net right-lateral NW-SE movement of about 280 m. This shearing motion deformed a strip of ice up to 65 m wide, building a long, nearly continuous ridge about 5-10 m wide and 3-4 m high (Fig. 16b).

PRESSURE RIDGE DISTRIBUTION

The distribution of all pressure ridges more than about 0.6 m high in the study area as of 23 March is shown in Figure 17. These data clearly demonstrate the ubiquitous nature of the ridges. In order to measure the orientation characteristics of these ridges, a representative study sector was arbitrarily chosen (square outlined in Figure 17). All ridges within it were subdivided into segments which could be approximated by straight lines. Next the orientation and length of each segment were tabulated. The mean segment length was calculated and then used to define a "standard ridge" (122.1 m). The frequency distribution of standard ridges as a function of direction (Fig. 18) shows a preferred orientation in the eastern and southern quadrants but a random orientation in the northern quadrant.

The Rayleigh test techniques of Curray (1956) and Krumbein (1939) were applied to these data to define a "preferred" orientation (127°) and to test if the observed ridges were randomly oriented. The results yielded a probability of < 0.00001 that the observed distribution could have been drawn from a randomly oriented population (Mock et al. 1972). Similar results were obtained with a variance ratio test and a goodness of fit test (Mock et al. 1972). From these results and the apparent absence of large rotational movements of the ice "floes," we conclude that the dominant ridge-forming compressions and shears have come from the east and west.
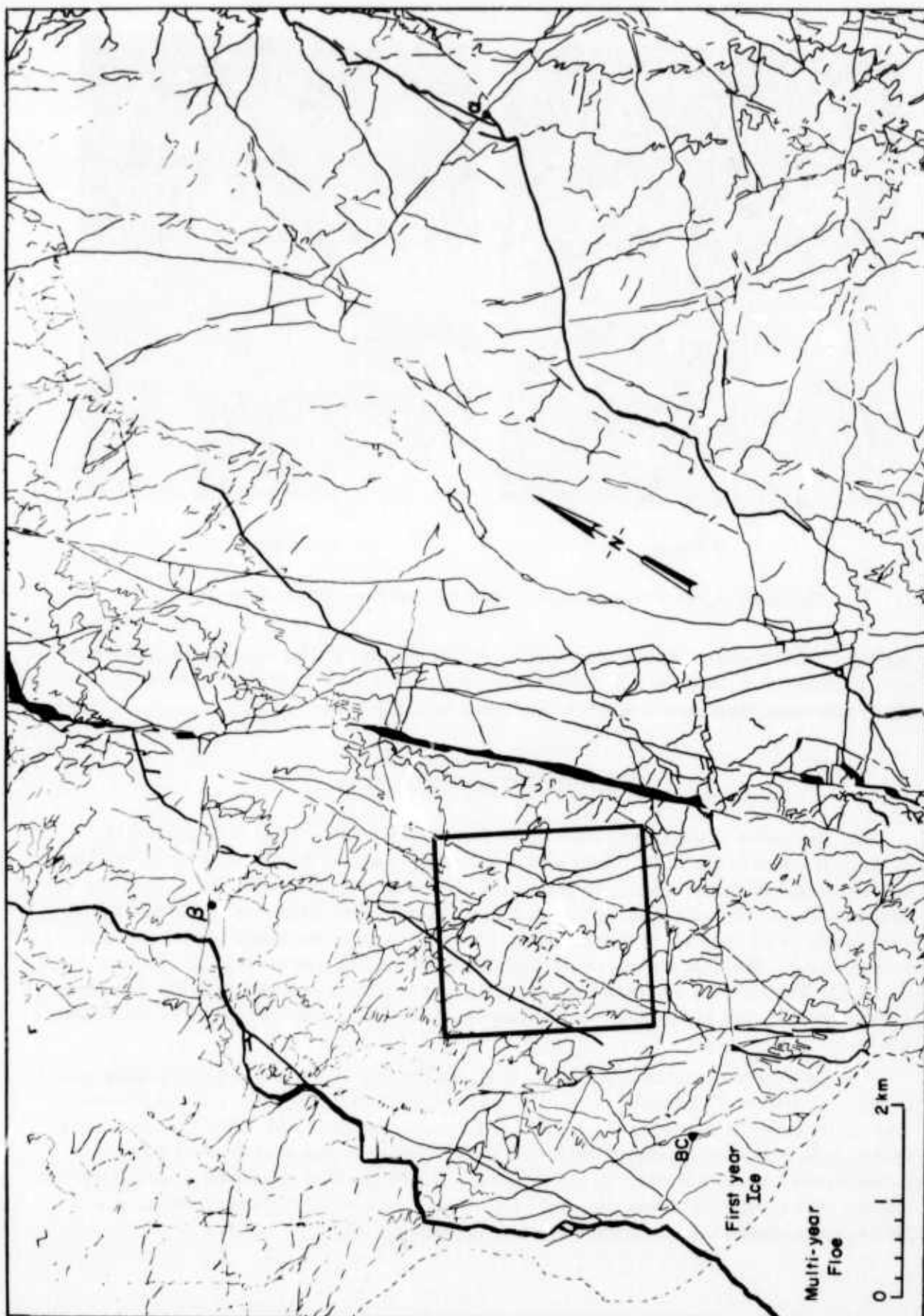
Figure 17.   Pressure ridges greater than about 0.6 m high, 23 March.   Square area is study sector for measurement of ridge orientation.
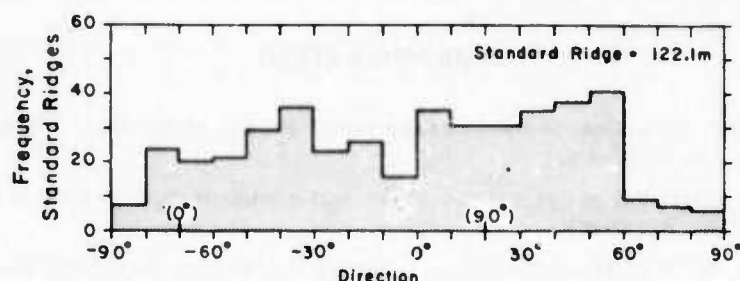
Figure 18. Frequency distribution of "standard" ridges as a function of direction.

SUMMARY AND CONCLUSIONS

During the two weeks of this study, at a time when no major cyclonic passages occurred, a variety of deformation events were observed in this region. Five main types of deformation were observed: 1) fracturing, 2) extension along fractures and formation of leads up to 150 m wide, 3) compression of leads and crumpling of their thin, refrozen ice cover into small ridges, 4) lateral compression of adjacent ice sheets and creation of ridges, and 5) shearing motion of up to 280 m and creation of ridges. During the study period the entire area was apparently under considerable lateral constraint with no significant rotation or rounding of floes such as Anderson (1970) observed in pack ice 72 km northeast of Point Barrow. Shearing motion was nearly always dextral or right lateral in accord with the clockwise rotation of the Pacific Gyre. At many locations fractures and leads developed with apparent "disregard" for ice thickness and thinner zones of refrozen leads (such as in Figures 9 and 10).

This study demonstrates that a rather complete interpretation of the deformation history of a given sector of sea ice may be made using sequential aerial photography in conjunction with surface strain measurements. For optimum results overlapping flight lines should be flown at several different altitudes. With a 15.2-mm (6-in.) lens, the following flight altitudes are recommended:

1. 8000-10,000 m for regional coverage of major lead systems and distribution of large multiyear floes.
2. 1500-2000 m for distribution of fractures, leads, pressure ridges and ice types.
3. 600-800 m for detailed delineation of deformation features for sequential studies.

Even with low-altitude photography such as that of 21 March (533 m) or 23 March (529 m) it was impossible to detect any significant deformation in "passive" features away from fractures, leads or relatively new pressure ridges.

ACKNOWLEDGMENTS

LITERATURE CITED

Anderson, V.H. (1970) Sea ice pressure ridge study: an airphoto analysis. *Photogrammetria*, vol. 26, p. 201-228.

Curray, J.R. (1956) The analysis of two-dimensional orientation data. *Journal of Geology*, vol. 64, p. 117-131.

Hibler, W.D., III, W.F. Weeks, S. Ackley, A. Kovacs and W.J. Campbell (1972) Mesoscale strain measurements on the Beaufort Sea pack ice (AIDJEX 1971), Part 1.

Kovacs, A. (1971) On pressured sea ice. *Proceedings of 1971 Sea Ice Conference*, Reykjavik, Iceland, in press.

Krumbein, W.C. (1939) Preferred orientation of pebbles in sedimentary deposits. *Journal of Geology*, vol. 47, p. 673-706.

Mock, S.J., A.D. Hartwell and W.D. Hibler, III (1972) Spatial aspects of pressure ridge statistics. *Journal of Geophysical Research*, in press.

PART V: DATA ON MORPHOLOGICAL AND PHYSICAL CHARACTERISTICS OF SEA ICE IN THE BEAUFORT SEA

by

S.F. Ackley, A. Kovacs, W.F. Weeks and W.D. Hibler, III

Introduction

The data reported here represent incidental measurements made at the main AIDJEX Camp 200 and at the strain network camps. In general, the data are not sufficiently representative to draw detailed conclusions from so the results are listed only to make them accessible and to document them for possible future reference.

Block size determinations in newly formed ridges

Two measurements were made of block sizes in newly formed pressure ridges. This parameter is of some interest since a recent model of the ridging process in sea ice has indicated that experimentally measured block sizes assist in the calculation of the fracture energy necessary to build pressure ridges (Parmerter and Coon 1973)*.

The two sets of measurements were made at two locations near strain site β (Fig. 1). The ridge at site A (from ground observations) apparently formed by a compression with the principal compressive direction normal to the edge of the thin ice in that area. This ridge thus corresponds roughly to the case modeled by Parmerter and Coon. If we reasonably assume that the same direction of motion caused the ridge at site B, then this ridge formed by a motion roughly parallel to the thin ice in that area or a shearing deformation mode. The data on block sizes for each ridge are listed in Table I. The block thickness was 0.19 m for both ridges.

Table I. Block sizes.

Site A		Site B	
Block width (m)	No. of blocks	Block width (m)	No. of blocks
<0.50	1	0.90 to 0.95	3
0.50 to 0.55	3	0.96 to 0.99	0
0.56 to 0.60	5	1.00 to 1.05	2
0.61 to 0.65	5	1.05 to 1.1	0
0.66 to 0.70	3	1.1 to 1.15	3
0.71 to 0.75	5	1.15 to 1.2	1
0.76 to 0.80	2	1.25 to 1.3	0
0.81 to 0.85	1	1.31 to 1.35	2
0.86 to 0.90	4	1.36 to 1.4	1
0.91 to 0 95	0	1.41 to 1.55	0
0.96 to 0.99	0	1.55 to 1.60	2
1.00 to 1.05	2		
1.20 to 1.25	2		

*Parmerter, R.R. and M.D. Coon (1973) Mechanical models of ridging in the arctic sea ice cover. AIDJEX Bulletin No. 19, Division of Marine Resources, University of Washington.
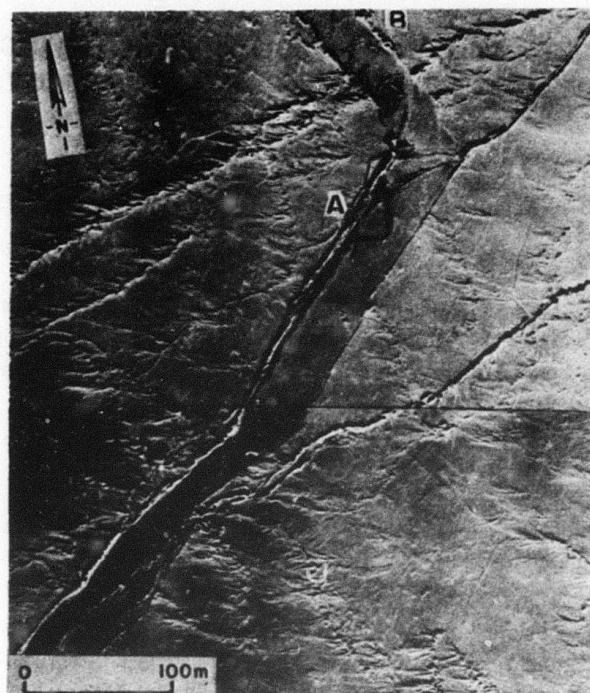
Figure 1. Location of sites for block size determinations approximately 300 m west of Camp β. Data from the two sites are shown in Tables I and II.

Table II. Statistical averages of the measured values.

	Site A	Site B
Mean block width	0.73 m ± .19 m	1.19 m ± .22 m
No. of measurements	33	14
Mean width/thickness	3.8	6.2

Salinity – temperature measurements

In addition to the measurements reported in Part II, *Structure of a Multiyear Pressure Ridge,* two additional vertical profiles were also obtained (Fig. 2, 3) as well as some near-surface salinities in thick first-year ice and in newly formed ice (Table III) measured in concurrence with ground-based microwave ellipsometer studies conducted by A. Edgerton and D. Williams of Aerojet-General Corp.

Two salinity values of freshly formed ice in a "pond" cut from a new lead northwest of camp for ellipsometer studies are listed below. The salinities are average values over the thicknesses indicated (sea water salinity 32‰).

Ice thickness	Salinity
3.8 cm	18‰
8 cm	20‰

These samples were collected soon after the ice formed and the salinity values represent that of newly formed ice, probably with very little brine drainage.
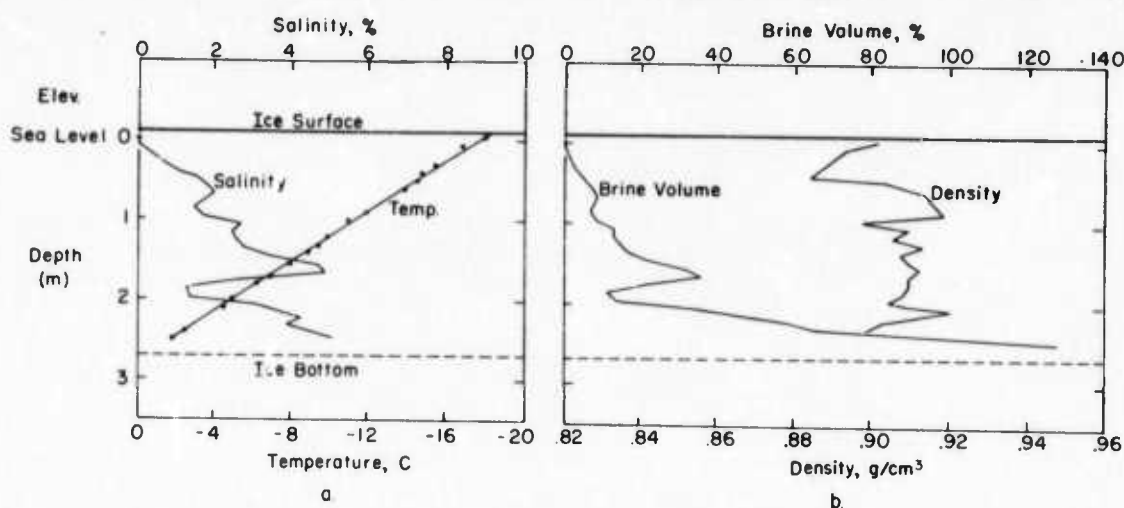
Figure 2. Salinity-temperature profile from station 133, profile line C. (Refer to Parts II and III of this report for details on the profile line locations.)
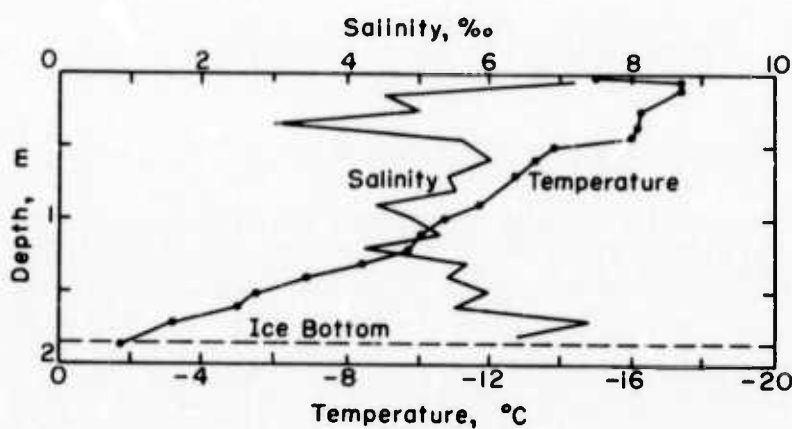

Figure 3. Salinity-temperature profile from first-year ice located just beyond the north end of the runway at the main camp. Ice thickness = 1.85 m. Depth measured down from top ice surface. Six centimeters of snow on top surface.

Table III. Surface salinity and temperature measurements.

Measurements made in same general locale (beyond north end of runway on first-year ice) as profile shown in Figure 3.

	Temp (°C)	Depth (cm)	Salinity (‰)
Site A	−19.6	1 8	10.0
Site B	−19.4	1 7	6.4